UNIVERSITY OF OKLAHOMA

GRADUATE COLLEGE

EXPERIMENTAL AND NUMERICAL STUDY OF A PASSIVE COLD THERMAL ENERGY STORAGE SYSTEM

A DISSERTATION

SUBMITTED TO THE GRADUATE FACULTY

in partial fulfillment of the requirements for the

Degree Of

DOCTOR OF PHILOSOPHY

By

Mohammad Shahabadifarahani

Norman, Oklahoma

2025

Downloaded from SHAREOK. Persistent Handle URL: https://hdl.handle.net/11244/341803

EXPERIMENTAL AND NUMERICAL STUDY OF A PASSIVE COLD THERMAL ENERGY STORAGE SYSTEM

A DISSERTATION APPROVED FOR THE

SCHOOL OF AEROSPACE AND MECHANICAL ENGINEERING

BY THE COMMITTEE CONSISTING OF

Dr. Hamidreza Shabgard, Chair

Dr. Pejman Kazempoor

Dr. Wilson Merchan Merchan

Dr. Jivtesh Garg

Dr. Reza Foudazi

©Copyright by Mohammad Shahabadifarahani 2025
All Rights Reserved.

Acknowledgments

First and foremost, I would like to express my deepest gratitude to my advisor, Prof. Hamidreza Shabgard, for his invaluable guidance, insightful advice, and unwavering support throughout my Ph.D. studies. His expertise and mentorship have been central to my academic growth and have greatly enriched my research experience. I am also sincerely grateful to Prof. Pejman Kazempoor, Prof. Wilson Merchan Merchan, Prof. Jivtesh Garg and Professor Reza Foudazi for serving on my Ph.D. committee and for their thoughtful feedback and suggestions, which have been instrumental in shaping and refining this dissertation. I would like to thank the staff of the School of Aerospace and Mechanical Engineering for their constant kindness, support, and assistance. A special thanks goes to Mr. Billy Mays and Mr. Greg Williams, as well as the students working in the machine shop; their generous help and technical support were essential to the completion of this research.

I am deeply appreciative of the generous financial support provided by the University of Oklahoma's School of Aerospace and Mechanical Engineering, alongside several scholarships. These include the James L Nicholson scholarship, Paul D Massad SHS scholarship, John E Francis scholarship, Thomas I Brown, Jr. scholarship, SHS-Frances & A Earl Ziegler Scholarhsip, C W _ Wilma Schwoerke Scholarship, and the Jim and Bee Close Scholarship, offered by the Gallogly College of Engineering. Their continued and gracious contributions have been instrumental in supporting my academic pursuits and research endeavors.

I would like to express my sincere regards and thanks to all my fantastic friends and schoolmates at OU and elsewhere, who enriched my life immensely not only when things were going well but also during tough times.

Last but not least, I extend my deepest gratitude to my family for their support during my Ph.D. journey, even though I have been thousands of miles away from them over the past years. My heartfelt thanks go to my mother, Mrs. Salehi, my father, Mr. Mohsen Shahabadi Farahani, and my brother, for their perpetual encouragement and blessings. Their constant support has been a cornerstone of my strength and perseverance during this challenging and rewarding academic endeavor.

Table of Contents

Chapter 1. Introduction 1

1.1 Background 1

1.2 Thermal Energy Storage Systems 3

1.3 Literature Review 5

1.3.1 CTES in HVAC Systems 6

1.3.2 Integrating CTES with Food Refrigeration 15

1.3.3 CTES in Data Center Cooling 19

1.3.4 Heat Pipe Assisted LHTES Systems 25

1.4 Research Gaps 36

Chapter 2. Design and Fabrication of the Novel CTES System 38

2.1 Description of Experimental Setup 38

2.1.1 HTF Conduit 39

2.1.2 PCM Storage Tank 42

2.1.3 Air-Cooling Section 44

2.2 Characterization of PCM Properties 46

2.2.1 Melting and Solidification Points 46

2.2.2 Viscosity of the PCM 47

2.2.3 Thermal Conductivity of the PCM 48

2.2.4 Thermal Expansion Coefficient of PCM 49

2.3 Experimental Procedure 50

Chapter 3. Experimental Analysis 53

3.1 Discharging Process (Melting) 53

3.2 Charging Process (Solidification) 55

Chapter 4. Numerical Model and Mathematical Formulation 58

4.1 Physical Domain and Computational Grid 58

4.2 Descriptive Equations for the Heat Pipe 63

4.3 Descriptive Equations for the PCM 65

Chapter 5. Results and Discussion 68

5.1 Experimental Results 68

5.1.1 Results for HTF Temperature of 55 ºC 68

5.1.2 Results for HTF Temperature of 50 ºC 70

5.1.3 Results for HTF Temperature of 45 ºC 73

5.2 Numerical Results 79

5.3 Performance of the System 93

5.4 Simultaneous Charge and Discharge Operation 94

Chapter 6. Concluding Remarks and Future Work 103

6.1 Concluding Remarks 103

6.2 Future Works 104

Nomenclature 107

References 110

List of Tables

Table 2-1 Thermistors of the experimental set-up..... 43

Table 2-2 Thermophysical properties of PCM, HP and fin jackets. 45

Table 2-3 PCM viscosity at different temperatures 48

Table 4-1 Complete computational domain dimensions. 59

Table 5-1 Settings used in the integrated HP–fin–PCM model implemented in ANSYS Fluent 81

Table 5-2 Comparison of predicted and measured melting and solidification times. 92

Table 5-3 Calculated heats and system thermal performance during the discharging process at varying HTF inlet temperatures at mHTF = 8.2 g/s and mHTF = 5 g/s. 94

Table 5-4 Calculated heats and system thermal performance during the charging process at varying HTF inlet temperatures at mHTF = 8.2 g/s and mHTF = 5 g/s. 94

Table 5-5 Calculated heats and system thermal performance during the simultaneous discharging and charging process at varying mass flow rates and temperatures 102

List of Figures

Figure 1-1 Schematic of the room and embedded PCM of Yanbing et al. [23] 7

Figure 1-2 Configuration of the solar air collector and PCM storage of Waqas et al. [25]. 8

Figure 1-3 schematic of the packed bed latent heat storage in the proposed setup of Nagano et al. [26, 27] during night and day. 9

Figure 1-4 schematic of working mechanism of plate-type storage system of Darzi et al. [28] . 10

Figure 1-5 the set up used for experiments of Zeinelabedein et al. [29]. 11

Figure 1-6 The schematic of the set-up of Reboli et al. [31]. 12

Figure 1-7 The schematic of the set-up of Lamrani et al. [33]. 13

Figure 1-8 The schematic of the set-up of Wang et al. [37]. 15

Figure 1-9 The schematic of the set-up of Ahn et al. [39]. 16

Figure 1-10 The schematic of a) set-up and b) cold storage unit of Liu et al. [41]. 18

Figure 1-11 Diagram of the cold storage accumulator integrated into a vapor compression cycle during (a) charging phase and (b) discharging phase of Yedmel et al. [42]. 18

Figure 1-12 schematic of the cold energy storage concept of Tareen et al. [44]. 20

Figure 1-13 the set up used for experiments of Singh at al. [45] 21

Figure 1-14 The emergency cooling system of Huang et al. [46]. 22

Figure 1-15 Schematic of the experimental set-up of Zheng et al. [47]. 23

Figure 1-16 Schematic of loop thermosyphon integrated with multi-tube TES unit of Ma et al. [48]. 23

Figure 1-17 The schematic of the test rig of Liu et al. [49]. 24

Figure 1-18 The schematic of cold thermal energy storage system of Liu et al. [50]. 25

Figure 1-19 The passive thermal management set up including PCM and finned heat set up used in Yang et al. [67]. 27

Figure 1-20 The schematic of tube-in-shell configuration LHTES system in Shabgard et al. [68]. 27

Figure 1-21 The schematic of the LHTES unit of Tiari et al. [69]. 28

Figure 1-22 The schematic of the test rig of Robak et al. [71]. 29

Figure 1-23 The thermal storage of Behi et al.[73]. 31

Figure 1-24 The experimental set up of Weng et al. [74] 31

Figure 1-25 The set up used in Krishna et al. [75] investigations. 32

Figure 1-26 The schematic of the test rig of Li at al. [76]. 32

Figure 1-27 Schematic of PCM/3D-OHP unit and (LSOHP) of Ling et al. [77]..... 33

Figure 1-28 Physical model and computational domain of Sharifi et al. [78]. 34

Figure 1-29 The schematic of the set-up of Zhong et al. [82]..... 35

Figure 2-1 Schematic of the experimental setup: a) front, b) side view; and photo of: c) experimental setup, d) key components such as the HTF conduit, PCM storage tank, and air-cooling section 39

Figure 2-2 different stages of solidification of PCM using Polystat chiller and measured beaker. 46

Figure 2-3 different stages of Melting of PCM using Polystat chiller and measured beaker. 47

Figure 2-4 measuring the viscosity of PCM using Brookfield Ametek viscometer..... 48

Figure 2-5 a) The set up of measuring the thermal conductivity for liquid PCM, b) solid PCM by C-Therm system. 49

Figure 2-6 measurements of thermal expansion coefficient using chiller and measured beaker. 50

Figure 4-1 Complete computational domain of the CTES system: (a) front view, (b) side view, (c) top view. 59

Figure 4-2 Computational domains: (a) Air-cooling section of the setup; (b) Water conduit section of the setup. Flow direction is along the x-axis. 61

Figure 4-3 The grid used for simulations. 63

Figure 5-1 Local temperature histories for $T_{HTF,\,in}$ = 55 °C and $mHTF$ = 8.2 g/s for. (a) Melting (discharging) and Solidification (Charging) of a) within the storage tank thermistors and, (b) outer storage tank thermistors 70

Figure 5-2 Local temperature histories for $T_{HTF,\,in}$ = 55 °C and $mHTF$ = 8.2 g/s for melting (discharging) and solidification (Charging) of a) within the storage tank thermistors and, (b) outer storage tank thermistors 72

Figure 5-3 Temporal evolution of melting (discharging) for $T_{HTF,\,in}$ = 55 °C and $mHTF$ = 8.2 g/s. 73

Figure 5-4 Temporal evolution of melting (discharging) for $T_{HTF,\,in}$ = 50 ° and $mHTF$ = 8.2 g/s. 73

Figure 5-5 Local temperature histories for $T_{HTF,\,in}$ = 45 °C and $mHTF$ = 8.2 g/s for melting (discharging) and solidification (Charging) of a) within the storage tank thermistors and, (b) outer storage tank thermistors. 75

Figure 5-6 Local temperature histories for a) $T_{HTF,\,in}$ =55 °C, b) $T_{HTF,\,in}$ =50 °C, and $T_{HTF,\,in}$ =45 °C at $mHTF$ = 5 g/s for melting (discharging) and solidification (Charging) of I) within the storage tank thermistors and, (II) outer storage tank thermistors. 77

Figure 5-7 Temporal evolution of melting (discharging) for $T_{HTF,\,in}$ =55 °C and $mHTF$ = 5 g/s. 78

Figure 5-8 Temporal evolution of solidification (charging) process following complete melting, with $T_{HTF,\,in}$ =55 °C and $mHTF$ = 5 g/s. 79

Figure 5-9 Temperature contours of a) HPs and fin jackets on the mid-plane (x–z) within the air-cooling section, and b) HPs within HTF conduit section (Air/water flow direction is from right to left.) 81

Figure 5-10 Computationally determined time variations of the melt fraction for a) $mHTF$ = 8.2 g/s and b) $mHTF$ = 5 g/s. 84

Figure 5-11 Computationally predicted temporal evolution of melting (discharging) for $T_{\mathrm{HTF,\,in}}$ = 50 °C and $mHTF$ = 8.2 g/s. 85

Figure 5-12 Computationally predicted temporal evolution of the solidification (charging) process following complete melting, with $T_{\mathrm{HTF,\,in}}$ =50 °C and $mHTF$ = 8.2 g/s. 87

Figure 5-13 Comparison of the liquid–solid interface for $T_{\mathrm{HTF,\,in}}$ = 55°C and $mHTF$ = 8.2 g/s: (a) Melting at $t_1 \approx 45$ min, (b) Solidification at $t_2 \approx 135$ min. (Water and air flow directions are from right to left.) 88

Figure 5-14 Heat flux to/from the PCM and average PCM temperature during discharge and charging cycle for different $T_{\mathrm{HTF,\,in}}$ and $mHTF$ = 8.2 g/s. 89

Figure 5-15 (a) PCM melt fraction, and (b) x-velocity -vectors on x-y plane crossing through the top of the PCM storage at time (I) t = 10 min and (II) t = 15min, with $T_{\mathrm{HTF,\,in}}$ =50 °C and $mHTF$ = 8.2 g/s. 90

Figure 5-16 Axial vapor velocity contours within the HPs for $T_{\mathrm{HTF,\,in}}$ =50 °C and $mHTF$ = 8.2 g/s at: (a) t = 10 min; (b) t = 30 min; (c) t = 45 min; (d) t = 60 min; (e) t = 90 min (the bottom end is in contact with the HTF) 91

Figure 5-17 Charge/discharge times vs. HTF inlet temperature and mass flow rate. 92

Figure 5-18 Local temperature histories for $T_{HTF,\,in}$ =50 °C, Tair,in $= 19 \circ$ C at $mHTF$ = 8.2 g/s and $mair$ = 150 g/s for simultaneous discharging and charging of a) within the storage tank thermistors and, (b) outer storage tank thermistors. 98

Figure 5-19 Temporal evolution of simultaneous discharging and charging $T_{HTF,\,in}$ =50 °C, Tair, in $= 19.5 \circ$ C at $mHTF$ = 8.2 g/s and $mair$ = 150 g/s..... 99

Figure 5-20 Local temperature histories for $T_{HTF,\,in}$ =50 °C, Tair,in $= 19.5 \circ$ C at $mHTF$ = 8.2 g/s and $mair$ = 75 g/s for simultaneous discharging and charging of a) within the storage tank thermistors and, (b) outer storage tank thermistors. 101

Abstract

Water scarcity and the inefficiencies of current cooling systems highlight the need for alternative cooling solutions. This study presents a cold thermal energy storage (CTES) system designed to store cold thermal energy during nighttime and release it during daytime operations. The experimental setup consists of three primary components: a hot water heat transfer fluid (HTF) conduit for melting, a vertical phase change material (PCM) tank, and an air-cooling section for solidification. Heat pipes were employed to facilitate cold thermal energy transfer from the PCM to the HTF during discharge (melting) and from the cold air to the PCM during charge (solidification). Two operational scenarios, charging (solidification) and discharging (melting), were investigated, with three distinct HTF inlet temperatures of 45°C, 50°C, and 55°C and two HTF mass flowrates of 8.2 kg/s and 5 kg/s. Local temperature measurements were collected, melting and solidification times were monitored, and thermal resistance of the systems were calculated. Results indicate that thermal resistance tends to decrease as the mass flow rate of the HTF or the HTF temperature increases, and that the useful energy exchanged by the PCM per discharge cycle is around 236–253 kJ. In addition, a transient three-dimensional numerical model was developed in ANSYS-FLUENT to provide insights into the underlying physics. The phase change was simulated using the enthalpy-porosity approach, with computational results showing reasonable agreement with experimental data. This study demonstrates a compact CTES module that stores off-peak “cold” in a PCM via heat pipes and releases it on demand, improving efficiency relative to purely mechanical cooling. The approach is a good fit for industrial, residential and data center cooling, enabling peak load management and short-duration backup while reducing water and energy use.

Keywords: CTES, Melting, Solidification, PCM, Heat pipe

Chapter 1. Introduction

This chapter sets out why industry and residential sections need cooling solutions that use far less water and power, and how thermal energy storage (TES) can make that shift practical. It begins with a short look at the competing demands for water and energy in industrial cooling and the limits of both wet systems (due to water use and regulation) and fully dry systems during hot/dry weather. Next, the chapter introduces TES as a means to produce cooling at one time and use it later, followed by a concise review of sensible, latent, and thermochemical options and how each is applied in operating plants. Afterwards, strategies for harvesting cooler nighttime conditions and integrating storage into existing equipment are outlined. Lastly, the literature review around application of CTES systems at different sections is summarized. Next chapter defines the focus of this work: a cold thermal energy storage (CTES) unit that uses phase change material (PCM) and high-conductance heat pipes to charge at night and discharge by day, cutting daytime power, shaving peaks, and reducing water use in industrial cooling.

1.1 Background

Cooling technology plays an important role in addressing water scarcity, a worsening global issue driven by increasing demand and shortage of resources. Industrial sectors like thermoelectric power, refining, petrochemicals, and data centers depend on reliable heat rejection. For example, thermoelectric power generation uses a large portion of freshwater for cooling, emphasizing the urgent need to manage water usage in industries. This issue is especially serious in arid regions, where relying on freshwater for cooling is no longer sustainable. Furthermore, water-based cooling systems are facing stricter regulations due to their environmental impacts on aquatic ecosystems, making it clear that alternative solutions are necessary. Dry cooling technologies have been developed as a solution to reduce water dependence. However, these systems face performance

challenges, particularly during hot weather, and have lower efficiency due to limited air-side heat transfer, leading to higher operational costs resulting in decreased efficiency and increased operational costs. As a result, their adoption has been limited [1, 2].

The most common industrial cooling options fall into three groups. Wet systems include once-through cooling (using rivers, lakes, or seawater), recirculating cooling towers, and closed-circuit fluid coolers. Dry systems include air-cooled heat exchangers and, in power plants, air-cooled condensers. There are also hybrid systems that combine wet and dry equipment in parallel or series and switch between modes as conditions change.

Enhancing the efficiency of cooling systems could be achieved through several methods. Active cooling strategies depending on mechanical systems and external energy sources, include combining wet and dry cooling methods such as vapor compression-based cooling (chillers), desiccant-evaporative cooling (desiccants dry the air before evaporative stages), and multi-evaporator cooling [3], implementing dew-point evaporative cooling techniques (direct/indirect evaporative coolers and dew-point evaporative systems) [4] and coupling cooling systems with renewable energy [5].

On the other hand, passive cooling methods focus on reducing energy consumption including managing internal heat gains, optimizing heat transfer through the envelope, facilitating heat exchange between indoor and outdoor air, or a combination of these approaches [6]. One of the promising passive approaches is to utilize nighttime cooling, where the cooler nighttime temperatures are captured and stored for use during the warmer daytime hours. This method is especially beneficial in regions with large day-to-night temperature differences, such as arid and semi-arid climates. By storing thermal energy during the night, these systems can address the

limitations of dry cooling technologies and reduce the dependence on water in wet cooling systems [7]. The focus of this study is on evaluating and optimizing nighttime TES systems for industrial/residential applications. Thermal energy storage systems can be applied across various energy sources, including solar, geothermal, fossil fuels, nuclear power, and industrial waste heat.

1.2 Thermal Energy Storage Systems

There are several energy storage technologies including thermal, mechanical (e.g., hydropower reservoirs, compressed-air energy storage, and flywheels), electrochemical (batteries), chemical (organic molecular carriers), as well as biological and magnetic storage methods. Thermal energy storage systems are one of the most widely studied and employed methods and can be divided into three categories:

Sensible Heat Storage (SHS)

SHS stores energy by changing the temperature of a material without a phase change. During charging, heat is added to the storage medium such as water, thermal oil, molten salt, concrete, or packed rock, leading to the greater temperature of the storage medium. During discharge, the medium cools as it gives that heat back to the process. This approach is inexpensive, and easy to scale (tanks and rock beds are common), and it works well when the supply temperature is allowed to vary over time. The balance between lower energy density (for a given temperature window) and larger volumes and insulation to limit losses; good thermal stratification and adequate heat-exchange area are usually important for this storage mechanism [8, 9].

Latent Heat Theral Energy Storage (LHTES)

Latent heat thermal energy storage systems use PCMs to absorb or release a relatively large amount of heat over a narrow temperature range as the material melts and solidifies. The

most well-known PCMs are organics (e.g., paraffins), inorganics (e.g., salt hydrates), and eutectic blends in which the phase-change temperature lines up with the process needs. Because the temperature stays approximately constant during the transition, LHS can deliver more stable outlet temperatures and much higher energy density than SHS when only a small temperature swing is allowed [10, 11]. PCM is the main material used in LHS systems. Selection of PCM is typically based on a balance between phase-change temperature, latent heat, thermal conductivity, cycling stability, and compatibility with containers [12]. PCMs show up in many applications like as building envelopes and HVAC/free-cooling, solar thermal and CSP systems, waste-heat recovery, and electronics or cold-chain thermal management [13]. For higher operating temperatures (120–1000 °C), materials such as carbonate, fluoride, and chloride salts are used for industrial storage, with their own benefits and constraints [14].

Thermochemical Heat Storage (TCHS)

Thermochemical heat storage stores energy in reversible chemical or sorption reactions. Compared with sensible (SHS) and LHTES, TCHS can achieve much higher energy density with very low standing losses because the energy is held as chemical potential rather than as temperature. The gains come with added complexity: purpose-built reactors, careful heat and mass-transfer management, control of reaction kinetics, attention to cycling durability, and safeguards for corrosion and safety [15].

Thermal energy storage systems are already widely used in cooling applications. For instance, in building cooling and air-conditioning systems, TES allows energy to be stored during low-demand hours for use during peak demand periods like pumps, pipes, and fans, ultimately lowering costs and improving efficiency [16]. To take advantage of the cooler nighttime temperatures, this research develops a LHTES system for cooling purposes. By combining PCMs

with heat pipes, the system enhances cooling efficiency. The proposed CTES system operates passively, storing cold energy during nighttime hours and releasing it during the day when cooling demand is highest. This approach reduces power consumption and helps to manage peak energy loads, offering a highly energy-efficient solution for industrial cooling systems. Moreover, the ability of the system to integrate continuously with existing infrastructure without requiring substantial modifications makes it a versatile and practical solution.

1.3 Literature Review

This section introduces progress through the challenges in cooling technologies that aim to reduce water usage and enhance efficiency. Conventional water-based cooling systems are increasingly unsustainable, while dry cooling alternatives suffer from inefficiencies, particularly during hotter periods.

The literature on CTES spans several application domains and shows how the same basic idea of storing cold and releasing it when needed works under different operating constraints. In this regard, this work is organized into four use cases, food cold-chain and storage, HVAC/buildings, electronics cooling, followed by research on heat pipe (HP)/PCM storage hybrids that address the low conductivity of PCMs, and data center cooling. For each area, we summarize how cols storage is implemented, what conditions make it effective, and the main performance metrics reported. The following chapter presents the experimental setup and describes each component of the proposed CTES system in detail.

Some studies propose the use of nighttime cooling systems, which capture cooler temperatures during the night to store energy for use during the day. This strategy has shown potential for addressing the limitations of existing systems, particularly in regions with significant

temperature differences between day and night. Storing cold during colder periods (such as nighttime) for use during peak daytime hours has been widely explored through LHTES systems utilizing PCMs. These systems offer high energy density and simplicity, requiring 5 to 14 times less space than SHS systems for the same energy capacity. An effective LHTES system comprises PCMs with suitable phase change temperatures, a storage medium, and a heat exchanger to facilitate heat transfer between the energy source, the PCM, and the target load. PCMs could be utilized either at high or low temperature. The application of PCMs in low temperature could be for ice storage, conservation and transport of temperature sensitive materials and in air conditioning, cold stores, and refrigerated trucks. However, their applications extend to high-temperature scenarios as well notable high-temperature PCM applications include solar power plants, industrial waste heat recovery, high-temperature TES, and building heating systems [11, 17-20].

1.3.1 CTES in HVAC Systems

One of the main purposes of cold storage is to maintain thermal comfort in residential, commercial, and industrial sectors by integrating it with conventional HVAC systems.

Nwaigwe et al. [21] reviewed nocturnal cooling systems, commonly known as night sky cooling, focusing on both air-based and water-based approaches. In air-based systems, building roofs function as radiators, dissipating heat to the night sky through evaporation or radiation. This cool air is then circulated indoors via fans or natural buoyancy. Conversely, water-based systems utilize water as the heat transfer medium. Cooled at night, the water is stored in tanks and later pumped through heat exchangers to cool indoor spaces. The study highlights that nocturnal cooling can potentially reduce cooling energy demand by up to 48%. However, it also notes challenges related to economic feasibility and geographic applicability.

Night radiative cooling (NRC) is an energy development method that harnesses the cooling potential of the night sky. Tsoy et al. [22] estimated the maximum possible amount of cold energy provided by NRC by calculating the heat transfer through a 1 m² radiative surface during the night across various cities, with radiating surface temperatures ranging from -30°C to 100°C. Their findings indicated that greater amounts of cold energy could be obtained in northern regions, especially during winter, when longer nights and lower temperatures prevail.

Yanbing et al. [23] introduced an innovative Night Ventilation with PCM Packed Bed Storage (NVP) system, where cool outdoor air is directed through a LHTES system and then released into the room during the day. Their research included both mathematical modeling and experimental studies, focusing on optimizing factors such as the surface area-to-volume ratio of the PCM for effective heat transfer, aligning the PCM melting point with day-night temperature variations, and ensuring sufficient airflow to meet varying cooling demands. The findings demonstrated an enhancement in indoor thermal comfort levels.

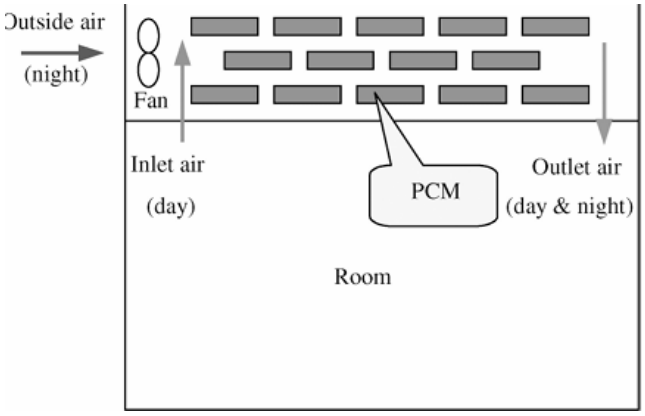

Figure 1-1 Schematic of the room and embedded PCM of Yanbing et al. [23]

Waqas and Kumar [24] explored the use of a latent heat storage unit to enhance comfort ventilation in buildings located in hot and dry climates. They developed a system that incorporates

PCMs to store cool energy during nighttime, which is then utilized for ventilation during the hotter daytime periods. Through both experimental and numerical analyses, the researchers assessed the system's thermal performance, focusing on its ability to maintain indoor thermal comfort and reduce reliance on conventional air conditioning. The findings indicated that the PCM-based storage unit effectively moderated indoor temperatures, thereby enhancing occupant comfort and potentially lowering energy consumption in arid region.

In another research, Waqas et al. [25] analyzed the performance of a PCM storage unit designed to provide both heating and cooling for buildings. The system harnesses solar energy and cool ambient night temperatures to store thermal energy, which is later used to maintain indoor comfort, Fig. 1-2. They utilized a flat-plate glazed solar air collector to absorb solar energy during the day. The collected energy was stored in a phase change material (PCM) chamber and used to heat airflow during cold nights. They found that the PCM storage unit performed optimally with melting points of 29°C in summer and 21°C in winter. The ideal temperature for year-round operation was determined to be 27.5°C.

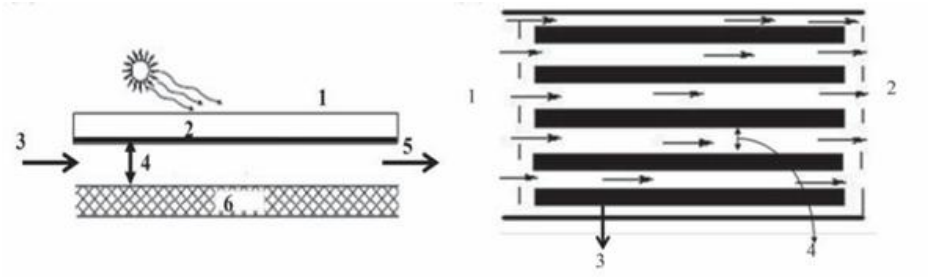

1: Glass Cover. 2: Absorber Plate. 3 Air inlet. 4: Air flow channel. 5:Air outlet 6: Insulation

1: Air inlet to PCM storage. 2:Air outlet from PCM storage 3: Storage material slabs 4: Air flow channel

Figure 1-2 Configuration of the solar air collector and PCM storage of Waqas et al. [25].

In their experimental and numerical studies, Nagano et al. [26, 27] proposed a floor supply air conditioning system that integrates packed bed latent heat storage within the building's structure. The system utilizes PCM granules consisting of granulated porous media with particles

approximately 1–3 mm in diameter, combined with paraffin wax as the PCM. Bench tests were conducted on a small-scale floor sample measuring 0.5 m², incorporating 30 mm deep PCM boards with a melting and solidification point around 20°C. Cool air from the air conditioning system circulates beneath the floor, charging the PCM packed bed with cold energy, which is later released into the interior space during air conditioning operation. The results indicated that integrating PCM boards allowed for the storage of 1.79 MJ/m² of heat overnight, enabling the air conditioning system to operate for only three hours during the day.

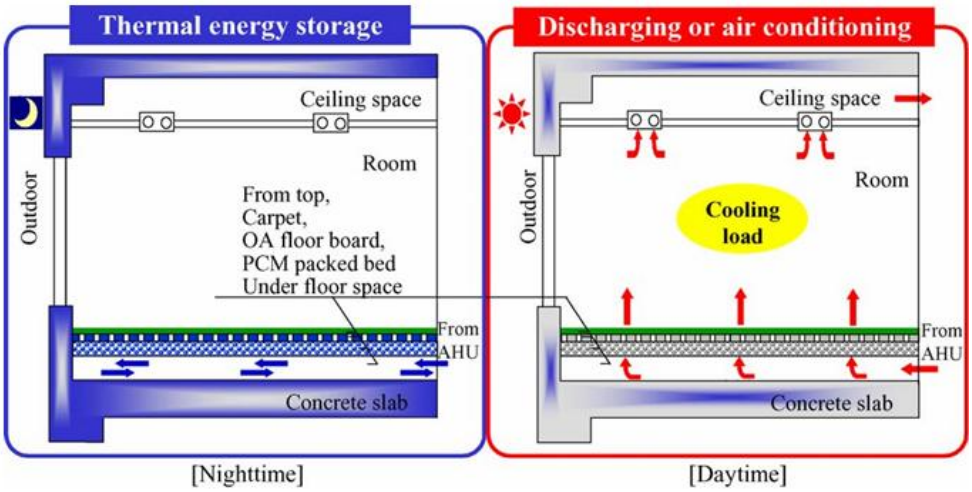

Figure 1-3 schematic of the packed bed latent heat storage in the proposed setup of Nagano et al. [26, 27] during night and day.

Darzi et al. [28] conducted a numerical study to optimize a plate-type storage system filled with PCM for use in night ventilation systems. They examined how variables such as air mass flow rate, PCM plate thickness, and inlet air temperature influenced cooling power, outlet temperature, PCM melting behavior, and overall thermal performance. The PCM used had a melting point between 22°C and 24°C, while room temperatures ranged from 23.5°C to 25.5°C. Their findings indicated that a smaller temperature difference between the indoor environment and the PCM's melting point enhanced heat exchanger efficiency. Additionally, PCM melting during

the day was directly proportional to PCM thickness; however, outlet temperature and cooling power remained unaffected by this parameter. Increasing the mass flow rate was identified as the sole method to boost cooling power.

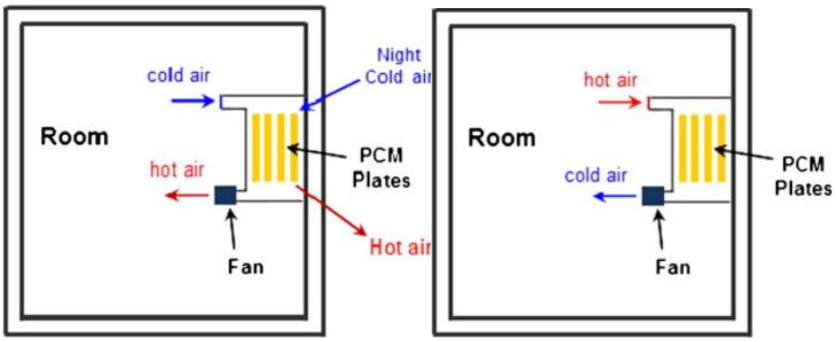

Figure 1-4 schematic of working mechanism of plate-type storage system of Darzi et al. [28]

Zeinelabedein et al. [29] experimentally investigated a modular PCM energy storage for free cooling of buildings at hot-arid climate condition. They studied the effect of PCM arrangement versus air flow in the PCM-air heat exchanger. They used paraffin RT28HC as PCM for rapid solidification and melting transition temperature range of 27-29 ºC. Their set up included macro-encapsulated PCM modulus embedded within an aluminum enclosure and a ducting system shown in Fig. 1-5.

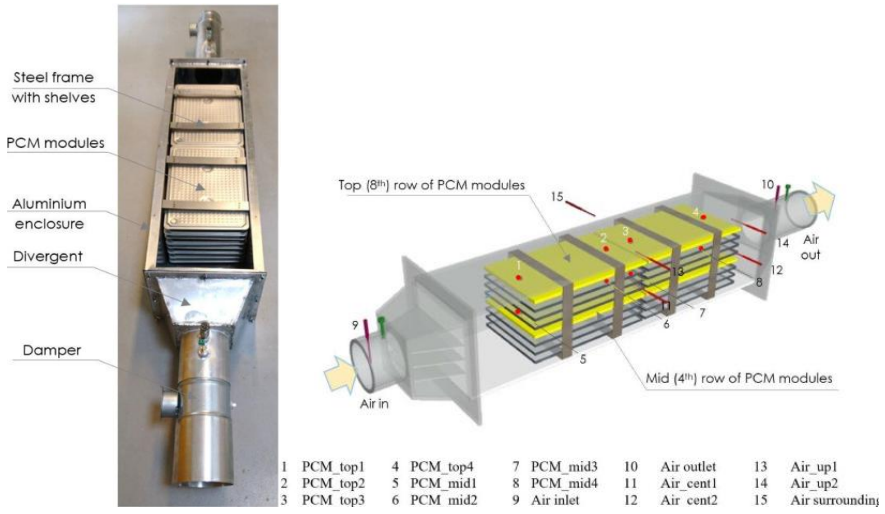

Figure 1-5 the set up used for experiments of Zeinelabedein et al. [29].

They reported that the air inlet temperature impacted the charging and discharging duration. They recommended higher air flow rates for accelerating the solidification process. Also, narrower air channels increased the cooling process and shorter solidification time, however it led to higher pressure drop and fan power consumption.

In another study, Hu et al. [30] investigated the performance of an HVAC system integrated with a PCM storage. Their set up included PCM storage, a heat pump and ventilation ducts. They monitored the impact of the PCM quantity on the charge and discharge process, the impact of air temperature and airflow rate on the discharge process. They found out that the PCM closer to the inlet melts/solidifies faster than that one closer to the outlet. They proposed different sizes of PCM storage for different applications and recommended big size PCM storage for long charge period applications like solar energy storage. Comparing the HVAC system integrated with PCM storage and without it, the system save energy bill for 7% for similar thermal comfort zone condition.

An experimental study performed by Reboli et al. [31], they focused on the discharge process of a full-scale, shell-and-tube CTES module. They evaluated the impact of HTF inlet temperature, mass flow rate, and flow direction (top-to-bottom vs. bottom-to-top) on discharge and output power. They found out that by doubling the HTF mass flow, peak power increased by 25%, and increasing the inlet temperature by 6 °C roughly doubled peak power. However, flow direction mattered insignificantly as buoyancy dominated during late-stage discharge. They reported the total thermal resistance of 0.0038 K/W for their system and a round-trip efficiency above 90% for the latent store.

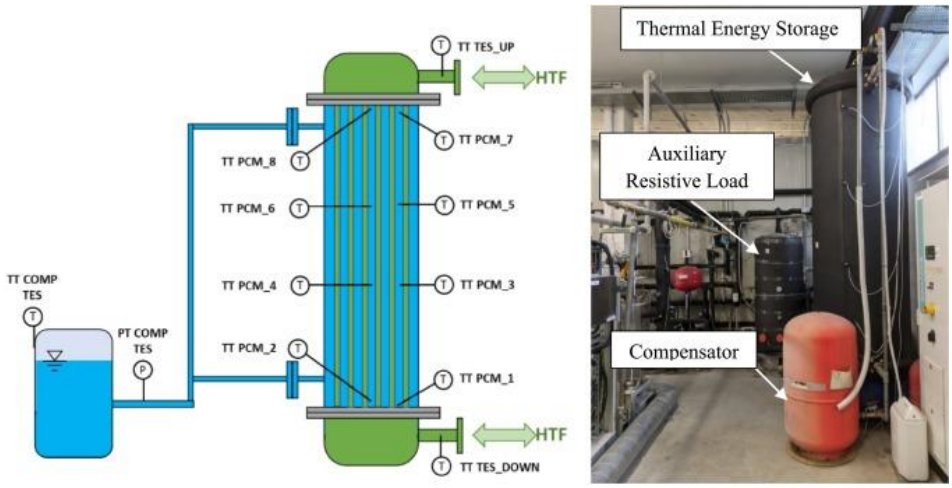

Figure 1-6 The schematic of the set-up of Reboli et al. [31].

Wang et al. [32] used TRNSYS for dynamic simulations of a clathrate hydrate ice-structured cold storage and tested how well it worked over a full year. They surveyed the differences of thermal performance between the hydrate cold storage and ice-cold storage systems. They used annual cooling loads from Shanghai, China to evaluate the operational costs and energy consumptions. The hydrate storage could move cooling to off-peak hours and cut peak power when it was run in the right temperature and pressure range. They reported lower energy consumption for the hydrate cold storage system in comparison to ice cold storage system.

Lamrani et al. [33] compared thermal performance of sensible (chilled water) and CTES options for building/district cooling in a realistic, time-varying operation. They built a lumped dynamic model for a shell-and-tube store, validate it against published experiments, and then ran simulations using water (sensible) and two commercial PCMs (RT4, RT5HC) as the storage medium. They observed that latent stores mechanisms offer much higher storage density when the operating condition matches the PCM's melt range, while chilled-water stores were sampler and less primary cost, when land is expensive or space is tight. They reported that PCM RT5HC extended the stable cold delivery in comparison to chiller water for a factor of 4.5. PCM RT5HC

had better performance versus PCM RT4 due to higher latent heat of fusion and greater energy storage capacity.

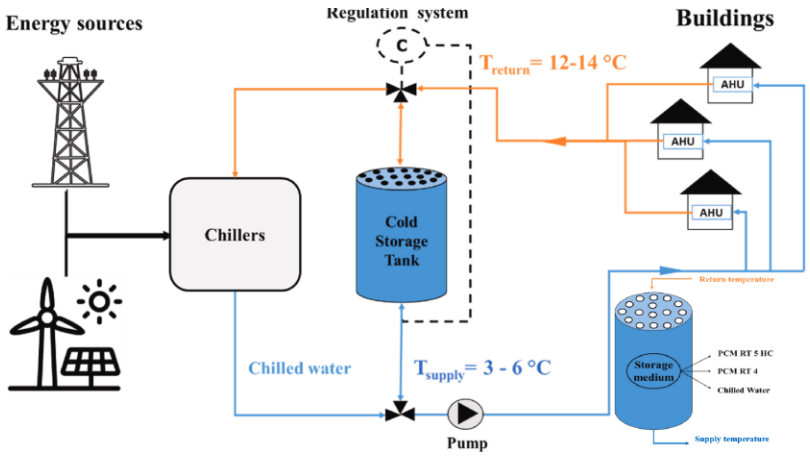

Figure 1-7 The schematic of the set-up of Lamrani et al. [33].

Alam et al. [34] reviewed mechanisms how cold thermal energy storage systems (CTES) have been being paired with renewable energy sources in air conditioning systems due to the rising cooling demand and the need to cut grid stress and emissions. They introduced main CTES options such as chilled water, ice, and PCM-based stores, and explained how they are charged by on-site PV/wind or off-peak power and then discharged at peak to reduce compressor work and shift load. Their research showed that CTES technologies including enhanced PCMs, improved ice storage systems, and innovative advanced materials had higher thermal storage of around 15%-25%. The output of their surveyed studies was practical that renewable assisted CTES reliably lowers peak electricity when the charge times aligns with local renewable output and tariff structure, while challenges remain around added capital cost, controls complexity, and long-term material durability.

Fang et al. introduced five main cold storage systems such as: chilled water storage system, coil pipe cool storage system, packed bed cool storage system, gas hydrate cool storage system

and ice slurry cool storage system. In above systems PCM can be employed to improve the performance of the cooling systems [35].

Yang et al. [36] reviewed research around the CO_2 hydrate slurry as a medium for cold energy storage, release, and transport. CO_2 hydrate slurry has high latent heat, is pumpable like a fluid, and is CO_2-friendly. Bringing together recent lab data and models, the authors emphasized an operating sweet spot: with the right promoter recipe and hydrate fraction, systems can lift overall efficiency (less compressor work, lower pumping penalty) compared with naïve settings. They also pointed out there still need more understanding about how the additives actually speed up freezing and melting, keeping storage and release stable in real plants, and clarifying how heat and fluid move inside the slurry.

Wang et al. [37] studied a multi-stage cold storage packed bed for air conditioning that used a modified sodium-sulfate decahydrate ($Na_2SO_4 \cdot 10H_2O$) PCMs to better match low-temperature cooling needs. Their idea was that instead of one PCM, they stacked three slightly different melting points (5.1 °C, 7.1 °C, 12.9 °C) within cylindrical capsules so the bed charged and discharged more effectively across the operating band (Fig. 1-8). Using a two-dimensional CFD model of the packed bed, they compared the cold storage capacity of various cases of filling ratio of the three PCMs, and the best multi-stage mix against a single-PCM bed. Their results showed a 4:2:4 split among the three PCMs raised cold storage density by 7.3% versus a single-stage bed and could cover at least an hour of emergency cooling for an AC unit.

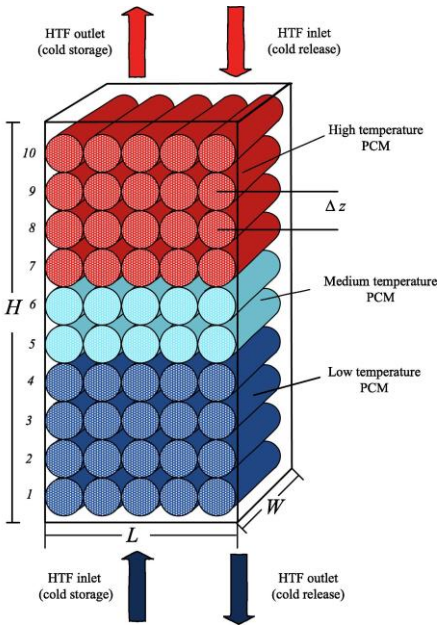

Figure 1-8 The schematic of the set-up of Wang et al. [37].

Hlanze et al. [38] studied an in-duct PCM storage concept that adds thin PCM panels to an air ducts of a building, and the system can charge off-peak (supply air set below the PCM solidification point) and discharge on-peak (warmer supply air use the stored cold). They built and calibrated a panel-level numerical model, then did simulation with EnergyPlus and a calibrated variable-speed DX system, testing five U.S. cities under actual time-of-use (TOU) tariffs. Using simple rule-based control, the PCM storage cut on-peak cooling energy by 23–32% and lowered seasonal cooling cost by up to 16%, with a simple payback of 7.5 to 27 cooling months depending on climate and rates.

1.3.2 Integrating CTES with Food Refrigeration

CTES is increasingly used in the food sector to keep products within temperature limits, reduce moisture loss, and maintain cooling during brief power interruptions or compressor restarts.

Ahn et al. [39] examined ice thermal energy storage (ITES) for food cold storage. In their study they monitored the performance of direct-contact, evaporative discharge cooling for food

cold storage while protecting product quality by minimizing latent heat transfer. They built a laboratory scaled rig including a commercial ice-making device (contains a reciprocating compressor, condenser, capillary tube for the expansion device, and an evaporator), a digital scale (the amount of ice stored in the ice storage was measured and then moved to the cooling unit), and a cooling unit (Fig. 1-9). They surveyed the effect of various parameters like inlet air temperature and humidity, face air velocity, and the amount of ice in the store on the cooling performance for different scenarios. The results showed direct-contact ITES can be tuned to deliver efficient evaporative cooling and they reported performance depends on both the air conditions and how much ice is exposed at a high face velocity. They found out that the weight loss ratio of the fresh food increased as the amount of ice increased. In the case of products with low weight-loss sensitivity (e.g., potatoes), the authors recommend using the ice amount that maximizes COP, while for items (e.g., mushrooms) sensitive to the amount of moisture, it is better to limit the ice to keep weight loss low.

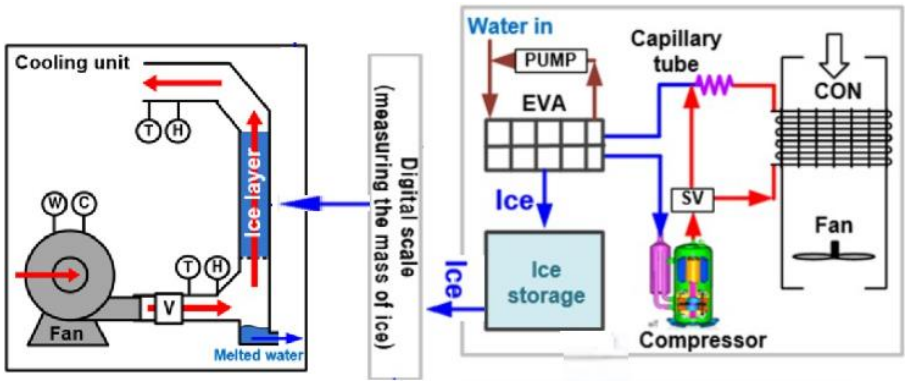

Figure 1-9 The schematic of the set-up of Ahn et al. [39].

In a review research Ouaouja et al. [40] surveyed what PCMs actually work best for CTES in refrigeration and cooling systems. Authors explored the usage of conventional PCMs including water/ice, hydrated salts, and paraffins and how they are built into chillers, display cases, cold-

chain packs, and building cooling so that “cold” can be made off-peak and used when it is needed. They also explored that bio-based PCMs could deliver similar performance with a smaller environmental footprint. They concluded that across the studies surveyed, utilizing the right PCM at the right temperature can decrease energy use, provides stabilized temperatures, and can lower emissions, while bio-based options look increasingly viable if durability and supply are managed.

Wang et al. [20] did a focused review on the recent advances of CTES in refrigeration cooling systems and how CTES should be operated and controlled in real cooling systems. They surveyed the main CTES storage media and layouts used in buildings and refrigeration with more focus on PCM mediums. They also classified the CTES systems as building cooling, cold chain logistics, and other refrigeration systems, based on the driven energy of passive and active cooling systems. They did performance optimization on various groups of the operational control strategies, cold load predictions and economic evaluation methods.

Liu et al. [41] experimentally tested a controllable separate heat pipe (CSHP) based cold storage temperature control system, and coupled it with a PCM tank to tackle uneven temperatures and slow response in cold TES. As shown in Fig. 1-10, their set-up comprised CSHP, cold storage unit, and cold supply loop (to simulate the operating conditions of the evaporator in a household refrigeration system), the usual loop hardware (pump, valves), sensors, and a data acquisition system. Different parameters such as temperature field distribution of the PCM and temperature control performance were monitored through charging and discharging process. Their system could keep the temperature of the fresh food compartment at 7 °C for an acceptable period. Also decrease in the temperature of ethylene glycol solution accelerated the storage rate of PCM.

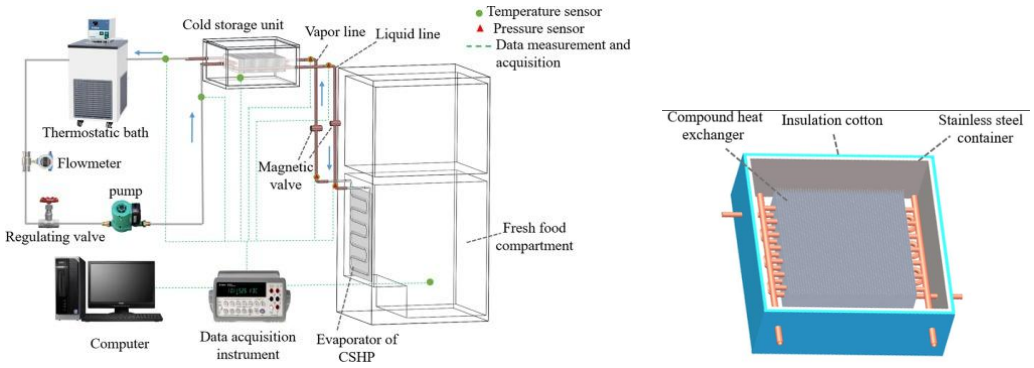

(a) (b)

Figure 1-10 The schematic of a) set-up and b) cold storage unit of Liu et al. [41].

Yedmel et al. [42] introduced a passive cold-storage accumulator that combined a thermosyphon with a PCM to capture cooling whenever needed and release it later. The two-phase loop of thermosyphon moves heat quickly into and out of the PCM block, so the storage medium charges and discharges with much lower thermal resistance than a plain PCM unit. In tests and modeling, the hybrid showed faster discharge/charge and more uniform temperatures than conventional alternatives. In cabinet tests that simulated a 1.5–2-hour shutdown, the hybrid held the rear duct air within the allowable range for 72 minutes versus 3 minutes without the accumulator. The air temperature rise was noticeably slower than the no storage case.

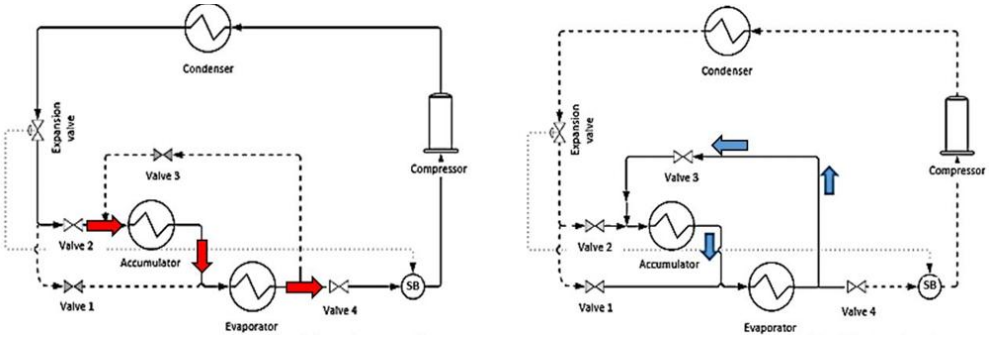

(a) (b)

Figure 1-11 Diagram of the cold storage accumulator integrated into a vapor compression cycle during (a) charging phase and (b) discharging phase of Yedmel et al. [42].

Continuing the previous study as Yedmel et al. [42] introduced their novel thermosiphon thermal accumulator (TTA), in another study they expanded their research to evaluate the performance of their system through various types of PCMs, ambient and thermostat temperatures, product loads, and door-opening scenarios [43]. They observed that discharging and charging performance was affected considerably by thermal loads and operating conditions.

1.3.3 CTES in Data Center Cooling

Data centers benefit from CTES because it delivers short, reliable cooling when the plant is stressed; during generator start, compressor trips, or hot-hour peaks without adding large mechanical capacity.

Tareen et al. [44] evaluated a seasonal ground cold energy storage concept for data center cooling that used passive thermosyphons to capture winter cold and release it during warmer months. Cold energy was stored in the saturated ground in form of sensible heat as well as latent heat of fusion of water. Using available climate datasets, the authors compared five Canadian cities and rank them by (i) how much cold can realistically be stored in the ground and (ii) the resulting carbon-footprint reduction for both new builds and existing facilities. The study linked location to outcome by accounting for local weather patterns and ground conditions in the storage model, then contrasts the thermosyphon approach with conventional mechanical cooling. They found that location matters significantly as some cities offer substantially higher storage potential and deeper CO_2 cuts. Also, their analysis provided practical guidance for where seasonal cold storage can deliver the biggest impact in data-center cooling.

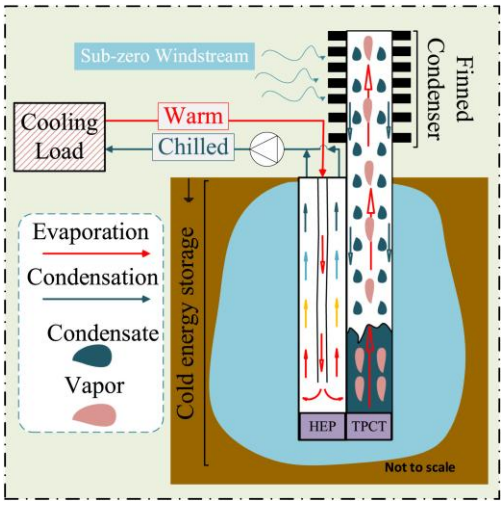

Figure 1-12 schematic of the cold energy storage concept of Tareen et al. [44].

Singh at al. [45] proposed a heat pipe based cold energy storage strategy for data centers, with the goal of cutting chiller run time, lowering electricity cost, and reducing associated CO_2. They framed two practical options, an ice storage system and a chilled water (cold water) store. They used heat pipe/thermosyphon heat exchangers to grab free ambient cold (when available) and move it efficiently into the store, then discharge that "cold" during peak or outage periods. Their results showed that both ice and cold water options were technically and economically viable for data centers. Ice storage is especially attractive in very cold climates (seasonal storage) while cold water storage is simpler where deep winter is not available. In all cases, the authors emphasized retrofit feasibility in the existing datacenters facilities with no major change in design.

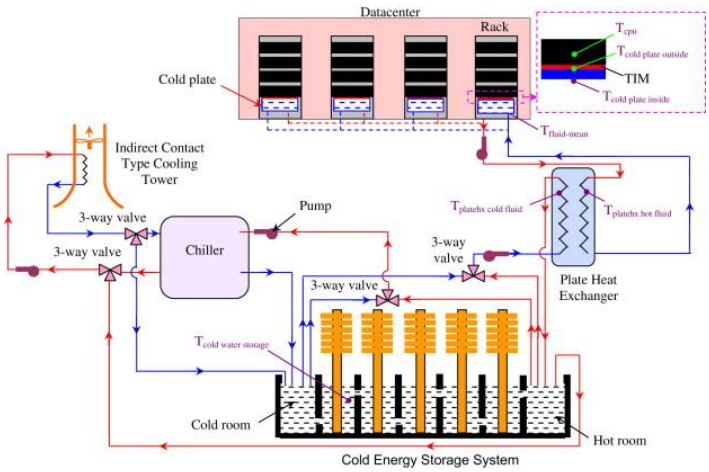

Figure 1-13 the set up used for experiments of Singh at al. [45]

Huang et al. [46] designed a PCM based cold storage unit for emergency cooling in an air cooled modular data center, in order to save time during outages without relying only on backup chillers. They tested two encapsulated PCM units within 1) smooth plates, and 2) smooth plates equipped with arcuate fins. The unit was mounted with the ceiling air-conditioner, so it could charge during normal operation (the PCM freezes) and discharge on demand (the PCM melts and absorbs heat). Authors built a test rig to measure charging/discharging behavior under realistic supply air conditions and airflow rates. Their results demonstrated that both PCM plate designs met the cooling need for 300s in the case of wind speed 1.5 m/s and inlet air temperature of 31 to 39 °C. for the case of 900s cooling, smooth plates could meet the need when the inlet air temperature was lower than 31 °C.

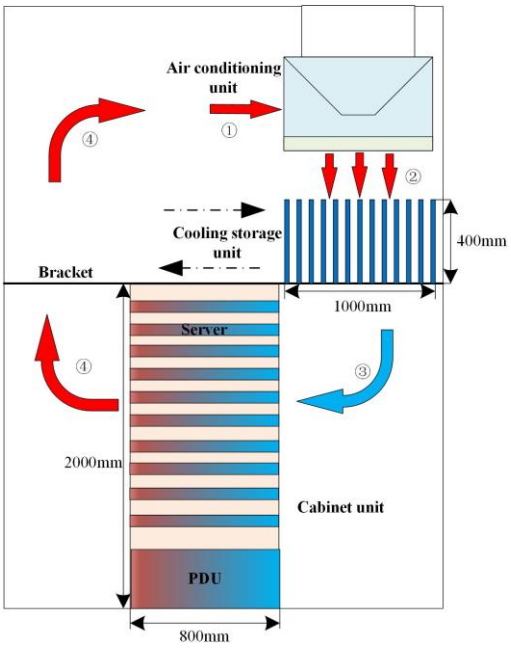

Figure 1-14 The emergency cooling system of Huang et al. [46].

In another research around cooling of data centers Zheng et al. [47] proposed an air-based phase-change cold storage (APCCS) unit for emergency cooling in internet data centers (IDC). They prepared the APCCS tailored to IDC supply air temperatures, built a test rig to measure charging and discharging, and developed a validated model for the discharge phase. The design of APCCS was cascaded from one to five PCM stages and was optimized using exergy analysis, and the PCM stages were designed from in-line to staggered configuration to improve heat transfer of air and PCM. They reported a raise in average exergy efficiency by 7.8%, added 19 kJ of exergy, and extended effective cooling time from 1300s to 1960s, moving from a single to a five-stage cascade. However, four-stage staggered arrangement performed best overall, delivering 10% higher average exergy efficiency and 25 kJ more exergy than the single-stage unit.

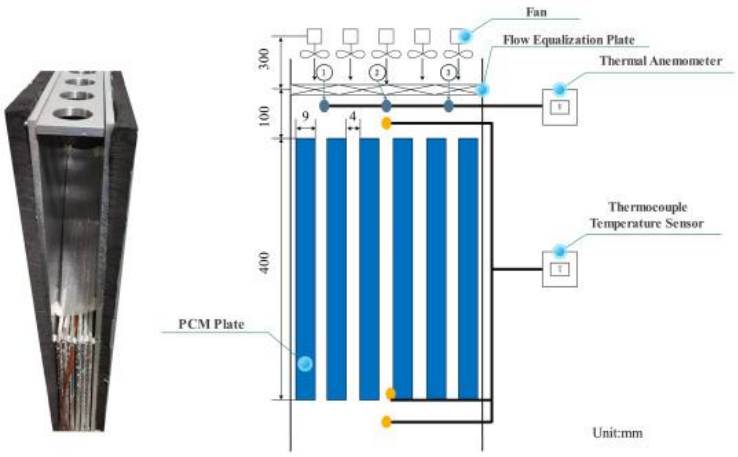

Figure 1-15 Schematic of the experimental set-up of Zheng et al. [47].

In an experimental and numerical study Ma et al. [48] proposed a passive solution for data centers that integrated a loop thermosyphon with a LHTES unit to absorb server heat during a chiller outage. Their system included a water-cooled loop thermosyphon (an evaporator, a vapor pipe, a condenser, and a liquid pipe) and a multi-tube PCM storage unit (Fig. 1-16). They could keep the operational condition of the servers for around 6 mins in the case of outrage of chiller. They also mentioned that if the thermal conductivity of PCM increased from 0.2 W/(m °C) to 2 W/ (m °C), the emergency cooling time rose to 15 mins.

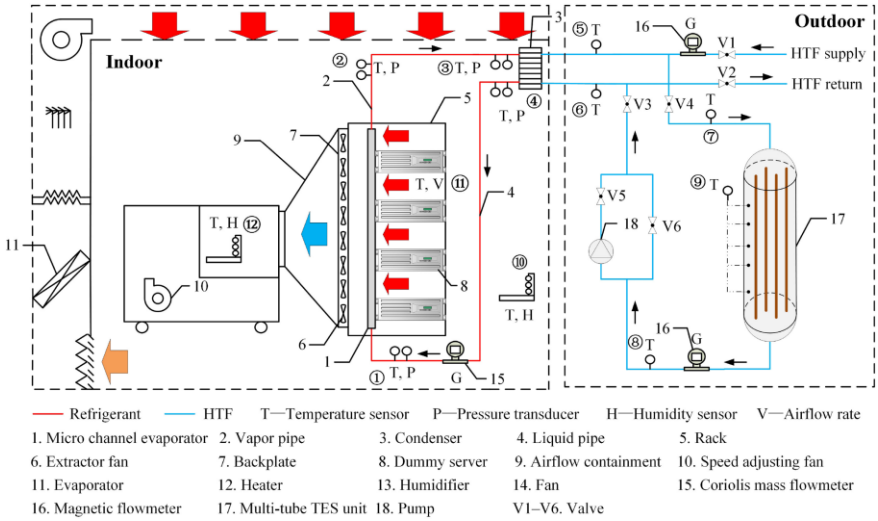

Figure 1-16 Schematic of loop thermosyphon integrated with multi-tube TES unit of Ma et al. [48].

Liu et al. [49] built and tested a novel thermosyphon integrated LHTES condenser (TLTEC) for data center cooling. The heat exchange mechanism of their condenser comprised of start-up, latent heat, sensible heat and fluctuating stages. They used two-phase HTF with varying condition. They studied the effect of filling ratio of HTF (refrigerant volume to evaporator, LTES, and connection lines volume) on the thermal performance. They showed that the two-phase path cuts thermal resistance and speeds transient response compared to conventional exchangers. Their results showed decrease in cooling capacity when the filling ratio increased form 48.7% to 82.5%.

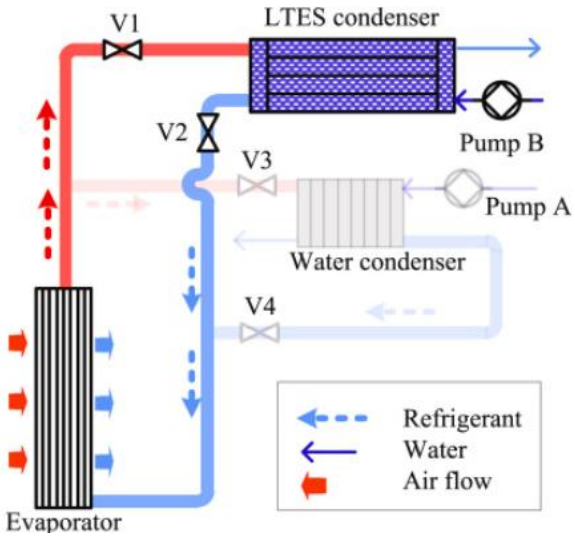

Figure 1-17 The schematic of the test rig of Liu et al. [49].

In a numerical investigations Liu et al. [50] studied a CTES block that was equipped with micro heat pipe arrays (MPHA-CTES). As seen in Fig. 1-18, their CTES included refrigeration unit, CTES device, heat exchanger, valves and pumps. Authors used a Taguchi design to see which fin features mattered most, finding that fin height had most contribution to melting/solidification time (70%), while fin thickness most strongly affects compactness (59%) (the ratio of cold energy storage material volume to the total CTES volume). They also tested a response surface method to capture interactions and run a multi objective optimization for goals of shorter solidification time, small heat-exchange temperature difference, and high compactness. The optimized design cuts

solidification time by 26.6%, holds the temperature difference to 4 °C, and reaches a compactness factor 0.822.

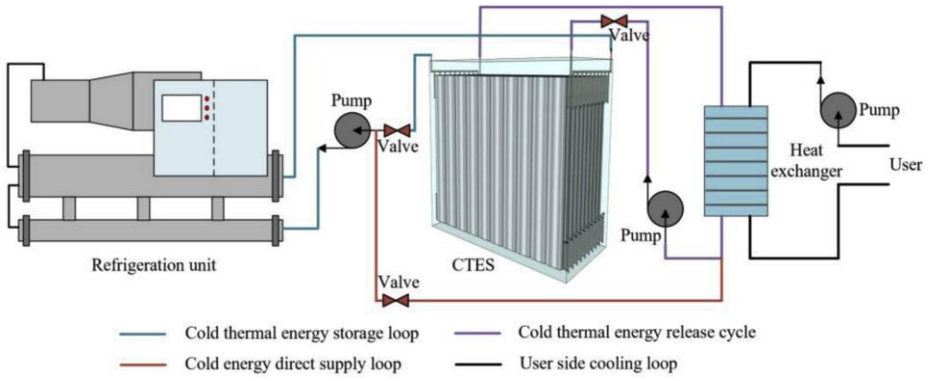

Figure 1-18 The schematic of cold thermal energy storage system of Liu et al. [50].

1.3.4 Heat Pipe Assisted LHTES Systems

A significant limitation of PCMs is their naturally low thermal conductivity, which affects their ability to efficiently store and release energy during the charging and discharging cycles and phase-change side effects such as subcooling or phase segregation. To address this issue, researchers have explored various strategies, including the integration of heat pipes, the use of nanoparticles, encapsulation, and embedding materials like fins or porous metal foams into PCMs to enhance thermal performance [51-59].

While these methods have contributed to energy storage considerably, there are still challenges particularly in balancing cost, system complexity, and overall efficiency. Among the proposed solutions, heat pipes stand out due to their high thermal conductivity, passive operation, and adaptability to different configurations. The integration of heat pipes is a key innovation to overcome the primary limitation of PCMs, low thermal conductivity. Heat pipes efficiently transfer heat passively, enabling faster and more uniform energy storage and release within the PCM. Despite their potential, further research is necessary to refine the design and integration of heat

pipes into LHTES systems, ensuring their practical applicability and maximizing their efficiency in real-world settings[60-65]. The direct integration of heat pipes with PCMs to overcome low PCM conductivity and accelerate discharge/charge, there have been various research around it.

Khalifa et al. [66] performed numerical and experimental investigations to improve the thermal performance of a concentrating solar power plan by the help of a high-temperature latent heat storage system equipped with finned heat pipes. In their proposed systems finned heat pipes were suspended in PCM adjacent to the outer surfaces of heat transfer flow channel. Fins were kept vertical to not hindering the natural convection effects in charging process. Their experimental part included a solidification process in which they observed significant improvement of the process after 45 minutes from the start of test compared to the initial stage. Furthermore, they observed better performance of the system by increasing the number of heat pipes.

Yang et al. [67] proposed a passive thermal management set up including PCM, low melting point metals (LMPM) and finned heat pipe (FHP) as shown in Fig. 1-19. The LMPM used in their experiments was a nontoxic eutectic alloy, Bi31.6In48.8Sn19.6 (E-BiInSn). They did their experiments for different cases like as FHP without PCM, Octadecabol/FHP, E-BilnSn/FHP, and Octadecanol/FHP. Their system showed excellent heat extraction capability due to its high thermal conductivity and high volumetric latent heat. They found out that the finned heat pipe can prohibit the temperature rise as it starts melting to protect the heat source from overheating.

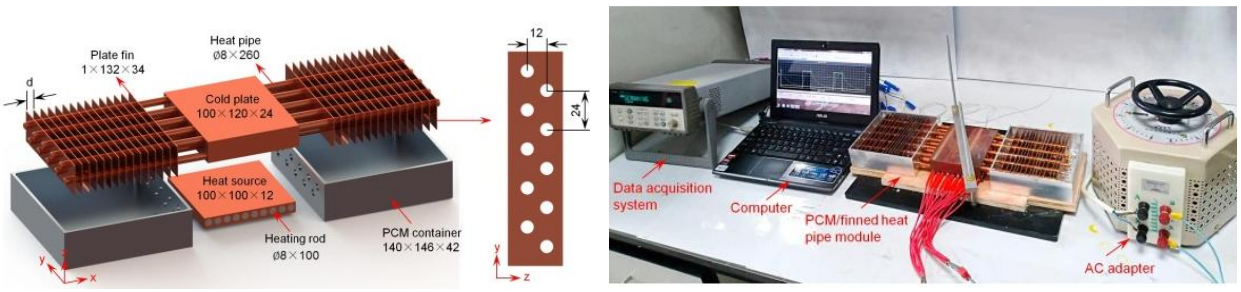

Figure 1-19 The passive thermal management set up including PCM and finned heat set up used in Yang et al. [67].

Shabgard et al. [68] studied the performance of a tube-in-shell configuration LHTES system. In their system shown in Fig. 1-20, PCM filled within either the tube (Module a) or the shell side (Module b). Their goal was to examine the benefits of the integration of heat pipes with LHTES systems, and they proposed a thermal network model. They found out that the heat pipe orientation has not a significant role in the thermal response of the Module 1 system, while it is an important factor for Module 2. They showed the thermal performance enhancement of the system by heat pipe effectiveness factor.

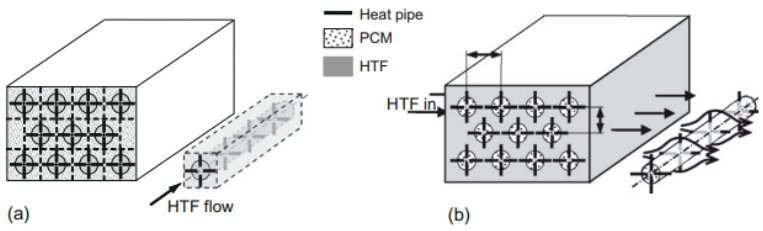

Figure 1-20 The schematic of tube-in-shell configuration LHTES system in Shabgard et al. [68].

Tiari et al. [69] numerically studied the charging process of a LHTES system with PCM filled in a square enclosure. The constant heat flux imposed on the base wall of the container was the mechanism of conductive heat transfer to the storage tank. One or multiple heat pipes along with fins mounted on the adiabatic and condenser sections of heat pipe are embedded in the PCM. Fig. 1-21 demonstrates the schematic of the LHTES unit of this study. They used Ansys Fluent commercial code for their investigations. Potassium Nitrate (KNO3) was considered as the PCM for their study. They examined the effect of heat pipes spacing and the number and length of fins and the effect of natural convection on the system performance. They observed 30% reduction in the time of charging by considering the natural convection in the simulations. Also, they showed

that by increasing the number of heat pipes (decrease the heat pipe spacing), the melting rate increases. The increase in the length of the fins help uniform temperature distribution within the PCM.

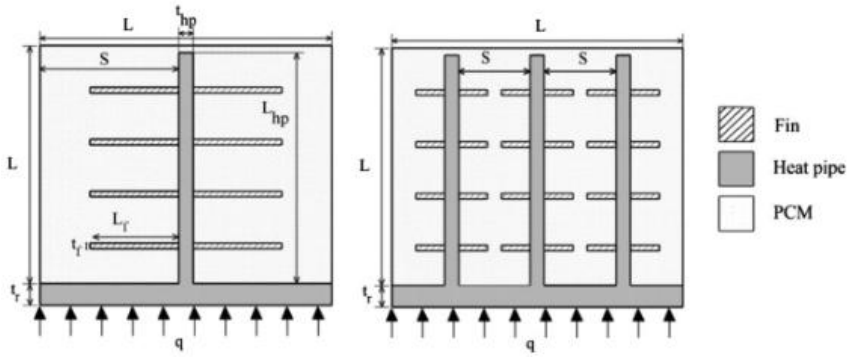

Figure 1-21 The schematic of the LHTES unit of Tiari et al. [69].

In a numerical research, Liu et al. [70] investigated the effects of inlet temperature of heat pipe and initial temperature of the PCM in charging process in a heat storage system. They examined these parameters regarding the thickness and temperature of the PCM, total heat storage capacity, and heat storage rate of the system. They used 13 heat pipes in their system and a specific paraffin with a melting point of 55 ºC as the PCM. They found that the heat storage capacity for the PCM of initial inlet temperature of 25 ºC is larger than the ones of 30 ºC and 35 ºC. The temperature of the outlet part of heat pipe increased gradually during sensible heat storage in solid and liquid states of the PCM, while it kept constant trend during the melting process or latent storage. The heat storage capacity was larger inlet heat pipe temperature of 70 ºC compared to 60 ºC and 65 ºC.

Robak et al. [71] experimentally investigated the performance of a cylindrical thermal energy storage for three different scenarios of with and without heat pipes and with fins. In the case of fins, heat pipes were replaced by stainless steel rods. The PCM they utilized was a n-

octadecane paraffin. The schematic of their experiments is shown in Fig. 1-22. There was a heat pipe in the center of cylinder and 4 others in a square pattern around it. They found out that the overall melting rate for the storage system integrated with heat pipes was on average 70% greater than the case of without heat pipes and 50% greater than the storage system integrated with fins. Also, the heat pipe-assisted case has 100% greater solidification rate compared to the case without heat pipes in discharging process.

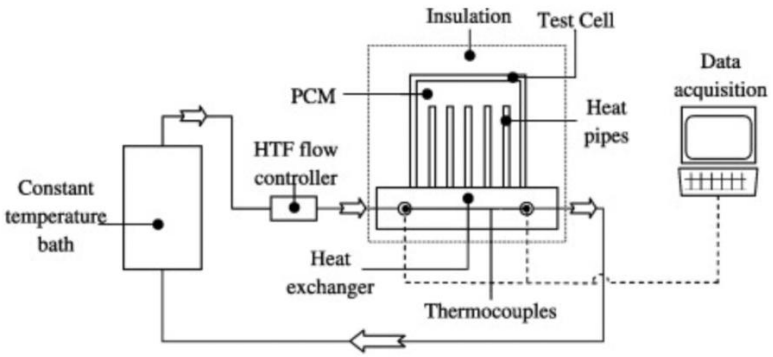

Figure 1-22 The schematic of the test rig of Robak et al. [71].

Ladekar et al. [72] did experimental study to compare the performance of a LHTES system while embedded with heat pipe or copper pipe. Their set up comprised of flat plate collectors, a sensible heat storage tank, and two LHTES tanks which one of them equipped by heat pipes and the other with copper rods. Seven heat pipes/copper rods were used for experiments and half of the copper/heat pipes were filled in PCM and the other half in water. Paraffin wax with melting temperature of 50-55 ^{o}C was considered as the PCM. They reported 187% improvement in the charging time for the configuration with embedded optimized heat pipe compared with the copper pipe embedded case. They also reported better charging and discharging process for the cases with larger diameter heat pipes from 16mm to 18mm.

Ali [62] in a comprehensive study reviewed researches considering latent heat storage systems integrated by heat pipes. He discussed some benefits of the combined system such as resolving the low thermal conductivity of the PCM and overheating of heat pipes. Combined system reduces the rate of temperature rise and makes safer operation working condition. The void formation is an important parameter regarding the solidification of PCM leading to thermal stresses and diminishing the heat transfer rate. Increasing the number of heat pipes increases the rate of heat transfer in charging and discharging. Heat pipes along with metallic foam, fins, and foil has better performance compared to heat pipe.

Behi et al. [73] studied the thermal performance and cooling capacity of a thermal storage including PCM and heat pipe. They examined two different configurations of the energy storage of PCM storage embedded with horizontal and vertical heat pipe. The test rig and schematic of the test process is shown in Fig. 1-23. They used RT42 from Rubithern Co. as the PCM with the melting point range of 38 ºC - 43 ºC. They reported up to 86% contribution of the proposed system to the cooling application for the working range of the heating power from 50 W – 80 W. They mentioned that employing the proposed system would lead to a reduction in the size of electronic cooling devices.

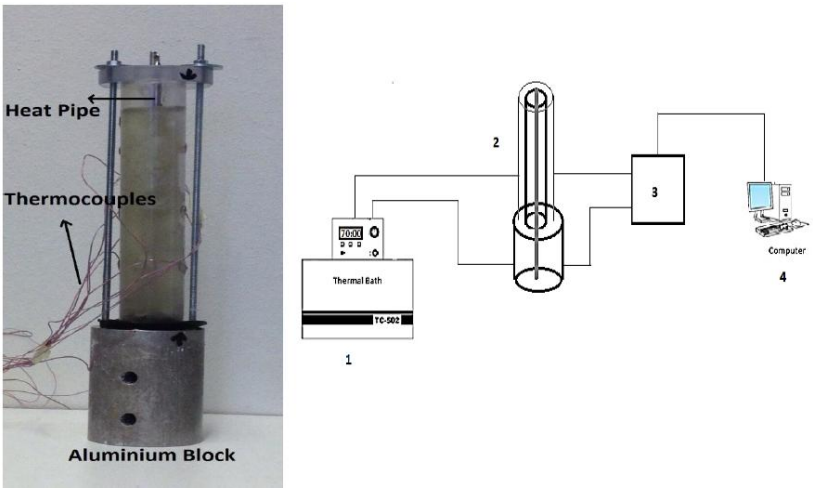

Figure 1-23 The thermal storage of Behi et al. [73].

Weng et al. [74] performed an experimental investigation on a thermal storage system cooling purposes showing in Fig. 1-24. Their system included a heat pipe, and their tests were done for different fan and heating powers, different filling volume of PCM, and also, they compared their results while using water instead of PCM. Their results showed that using Tricosane as PCM in the heat pipe module can result in a reduction of up to 46% in fan power consumption and an average heater temperature decrease of 12.3°C when compared to not using any thermal storage material.

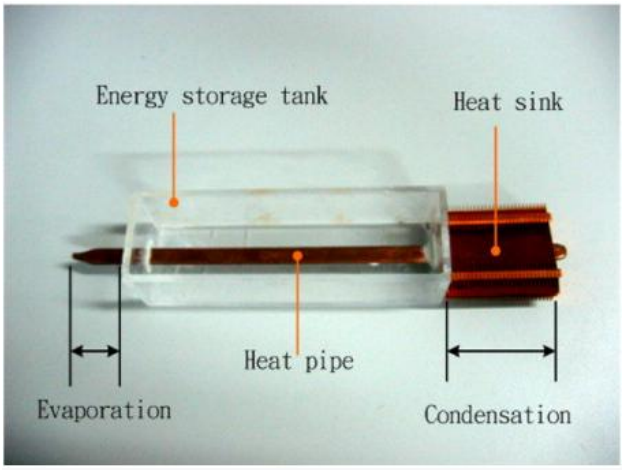

Figure 1-24 The experimental set up of Weng et al. [74]

In another research Krishna et al. [75] performed experiments for nano-enhanced PCM with different volume percentages of 0.5%, 1%, and 2% of Al2O3 nanoparticles on the set up close to the previous research shown in Fig. 1-25. They examined the effect of PCM material and quantity, heat input, fan voltage and nano-particles concentration on the performance of cooling module. They reported the reduction in the temperature of the evaporation part of the set up by 25.75% when PCM is replaced by 1% volume of nano enhanced PCM for energy storage. They

also reported the capability of storage of 30% energy supplied from the evaporator part at by nano enhanced PCM contributing to the lower fan consumption.

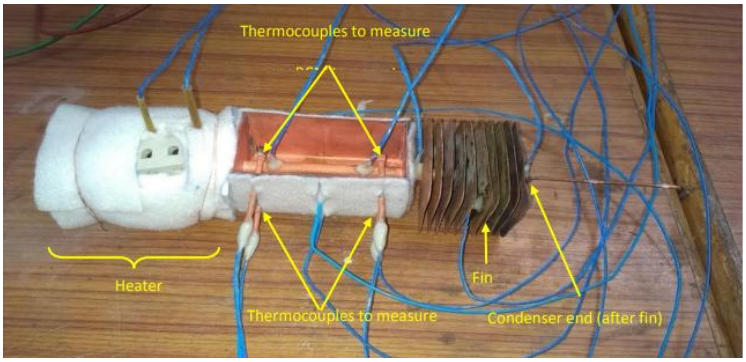

Figure 1-25 The set up used in Krishna et al. [75] investigations.

Li at al. [76] carried out experiments on a system including enhanced thermal and thermoelectric structure using flat heat pipe shown in Fig. 1-26. They used encapsulated PCMs in a polycarbonate cavity as storage mechanism. They reported considerable increase in the phase change heat transfer for the case of heat pipes assisted compared to pure PCM. They reported a 7ºC difference between PCM and heat pipes during the solidification process.

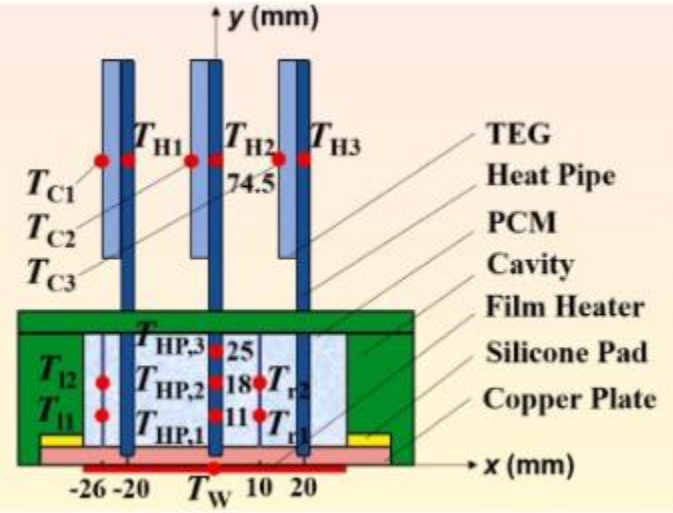

Figure 1-26 The schematic of the test rig of Li at al. [76].

Ling et al. [77] studied on the electronics cooling by pairing PCM with a three-dimensional oscillating heat pipe (3D-OHP) to see whether this hybrid system can outperform plain air cooling under realistic operating conditions. The contractual law was utilized to provide a leaf-shaped three-dimensional oscillating heat pipe (LSOHP). The mechanism was straightforward that the heating power of 25-100W was transferred to PCM, while the 3D-OHP transferred that stored heat to ambient air. Different cooling air velocity, wind direction, and heat input were tested in their study. In tests, the proposed mechanism held surface temperature of electric devices around 35 °C lower than conventional air cooling, cutting thermal resistance by up to 36.3%. The LSOHP configuration reduced a further 2 °C from the device surface versus a typical 3D-OHP.

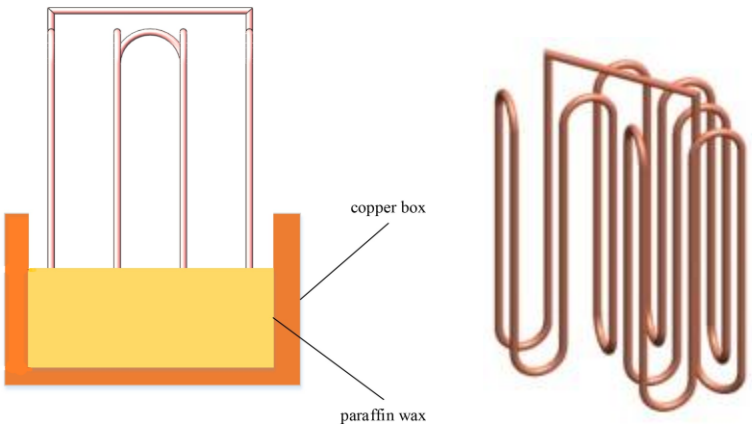

Figure 1-27 Schematic of PCM/3D-OHP unit and (LSOHP) of Ling et al. [77]

Sharifi et al. conducted a numerical investigation on the melting behavior of Phase Change Material (PCM) integrated with three different configurations: a vertically-oriented heat pipe, a solid rod, and a hollow tube. In their study, the condensation area of the heat pipe was in direct contact with the PCM as shown in Fig. 1-28. The simulations were performed using a finite volume-based model, exploring various heating methods applied to the top and bottom parts of the heat pipe by changing the gravity direction. Their findings demonstrated that the vertically-oriented heat pipe significantly outperformed the other two configurations in terms of PCM

melting rate. This performance was due to the heat pipe's ability to enhance heat transfer effectively. Additionally, they observed that increasing the length of the condensation section or the diameter of the heat pipe further improved the melting rate [78].

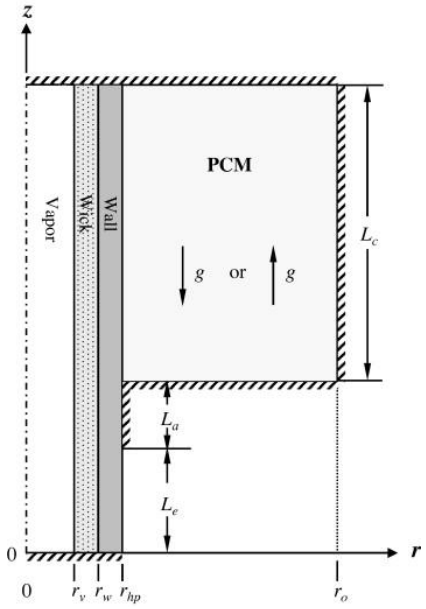

Figure 1-28 Physical model and computational domain of Sharifi et al. [78].

Liu et al. [79] reviewed several studies including heat pipes with PCMs as an effective way to overcome low conductivity demonstrating typical layouts and operating mechanisms.

Qu et al. [80] designed a three-dimensional oscillating heat pipe (3D-OHP) integrated in a LHTES including PCM, so a two-phase oscillatory flow can move heat quickly into and out of the storage volume. They did tests on a LHTES unit utilized 6 turns 3D-OHP and LHTES unit assisted by a conventional heat pipe (CHP) for different composite PCMs and heating powers. Their results showed that the 3D-OHP design reduced thermal resistance, speeded melt/solidify times and improved temperature uniformity in the PCM compared with the baseline (CHP), making it a practical alternative to faster cycling in latent-heat stores.

Maldonado et al. [81] compared a conventional shell and tube LHTES and heat pipe based design of LHTES to see which moves heat through the PCM more effectively under the same operating conditions. They built five prototypes, one shell-and-tube unit and four heat pipe configurations and ran discharging tests at fixed HTF temperature and flow, logging temperature histories, calculating heat-transfer rates, and visually tracking the melt front. Their results showed that the heat pipe assisted designs discharged faster and more uniformly than the shell-and-tube model, showing higher effective power during transients. Authors recommend heat pipes as a strong alternative when compactness and fast cycling are priorities.

In an experimental and numerical research Zhong et al. [82] on a thermoplastic elastomer-based form-stable phase change material. Their system comprised a sealed thermosyphon and form-stable PCM (FSPCM) section as shown in Fig. 1-29. Their system showed latent heat of the FSPCM has minor effect on the melting time. The extension of the evaporator section led to faster phase change of PCM up to a threshold, and this effect decayed after that. In other words, when the evaporator was long enough, thermal resistance went to condenser section (FSPCM).

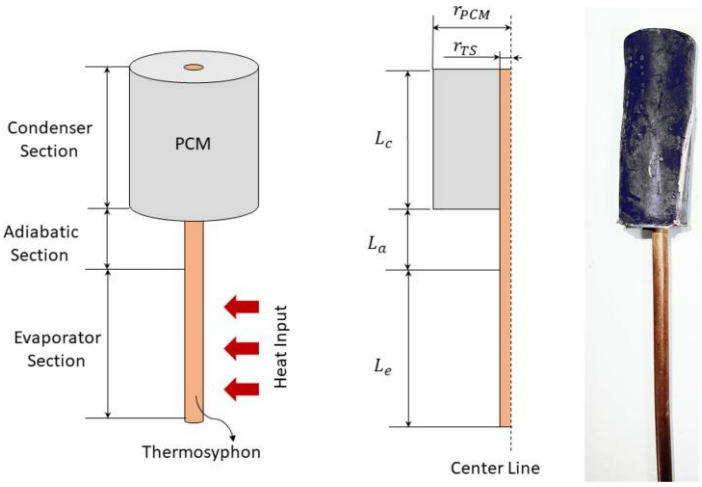

Figure 1-29 The schematic of the set-up of Zhong et al. [82].

In another numerical study, Sharifi et al. [83] investigated conjugate heat transfer within a module that integrates PCM with a vertically-oriented HP. Their study analyzed the melting and solidification processes under three distinct operational modes: charging-only, simultaneous charging and discharging, and discharging-only. Their simulations incorporated all relevant heat transfer mechanisms, including conduction through the wick and wall sections of the HP, evaporation and condensation of the HP's working fluid, and natural convection of the molten PCM within the cavity. The results indicated that increasing the aspect ratio (the height-to-diameter ratio) of the PCM cavity led to a relative improvement in melting efficiency during the simultaneous charging and discharging process. This suggests that optimizing the cavity geometry can enhance the thermal performance of the system, particularly when both charging and discharging occur concurrently.

1.4 Research Gaps

A review of the prior CTES literature reveals a few clear gaps. Many published systems are actively driven; pumps, compressors, or complex controls run throughout the cycle which improves power but also raises operating cost and complexity. In contrast, the approach taken here is mainly passive, using simple design using HPs for heat transfer through discharge and charging process. A second gap is that, to the authors' knowledge, only one prior study has developed a numerical model in ANSYS-FLUENT for an HP–fin–PCM system that attempts to resolve the governing equations of heat pipes, specifically in the context of battery thermal management applications [84]. The present research represents the second effort in this area and extends the application of such modeling to CTES systems. Most existing studies involving HP–fin–PCM configurations continue to simplify HP behavior by representing them as regions of high effective thermal conductivity or using thermal resistance networks. In contrast, the present study advances

the numerical modeling framework by explicitly solving the full governing equations of heat pipes while concurrently capturing conjugate heat transfer within the PCM and fin structures. This integrated and detailed approach provides a more physically accurate representation of the coupled thermal phenomena, positioning the current work as a valuable contribution to the field. Finally, most demonstrations use the storage only for discharge and rely on a separate heat exchanger or a second unit to recharge. The module developed here performs discharge and charge in the same storage medium and can even do both simultaneously without any extra heat exchanger. Together, these choices target simpler integration, reduce auxiliary energy use, and a storage block that is closer to how real plants would use it.

This experimental and numerical study explores the potential for integrating the proposed CTES system into existing cooling systems, demonstrating its feasibility for improving energy efficiency and sustainability with providing a detailed performance analysis of the proposed systems. The innovative design of the proposed system presents a new approach for cold energy storage, offering a model for applications in various industrial/residential sectors. The proposed configuration is designed to be easily integrated into conventional industrial cooling systems, thereby contributing to significant reductions in both energy consumption and water usage. This aligns with global efforts aimed at improving sustainability and energy conservation.

Chapter 2. Design and Fabrication of the Novel CTES System

In this chapter, the innovative CTES system is introduced, and its working mechanism is explained in full. The section starts with the description of the CTES system and different sections of that. A practical CTES module is designed to charge at favorable times (nights) and discharge by the peal times, combining a PCM storage core with embedded heat pipes (HPs) so “cold” can be stored and moved. The two other subsystems, heat transfer fluid (HTF) conduit and air-cooling section, are then described in this chapter. Materials are selected, PCM with a phase change temperature in the desirable range (high latent heat, good cycling stability), and heat pipes (envelope, wick, working fluid) chosen for heat transfer in repeated cycles, copper fins to maximize the heat transfer in air cooling section, and thick acrylic walls for better heat loss inhibition. For measurement and control, thermistors with the proper range/accuracy are placed at different locations, and the heating method used in lab charging is chosen to be compatible with the PCM melting point to ensure repeatable boundary conditions. A prototype is then built and tested, quantifying discharge/charge times and delivered cooling, and to calibrate and validate the numerical model of the CTES.

2.1 Description of Experimental Setup

Figure 2-1 presents a schematic diagram and a photograph of the experimental setup The experimental setup is consisted of three subsections: (i) a HTF conduit, (ii) a PCM storage tank, and (iii) an air-cooling section. Each section is detailed in the following to ensure a thorough understanding of the system's design and operational principles.

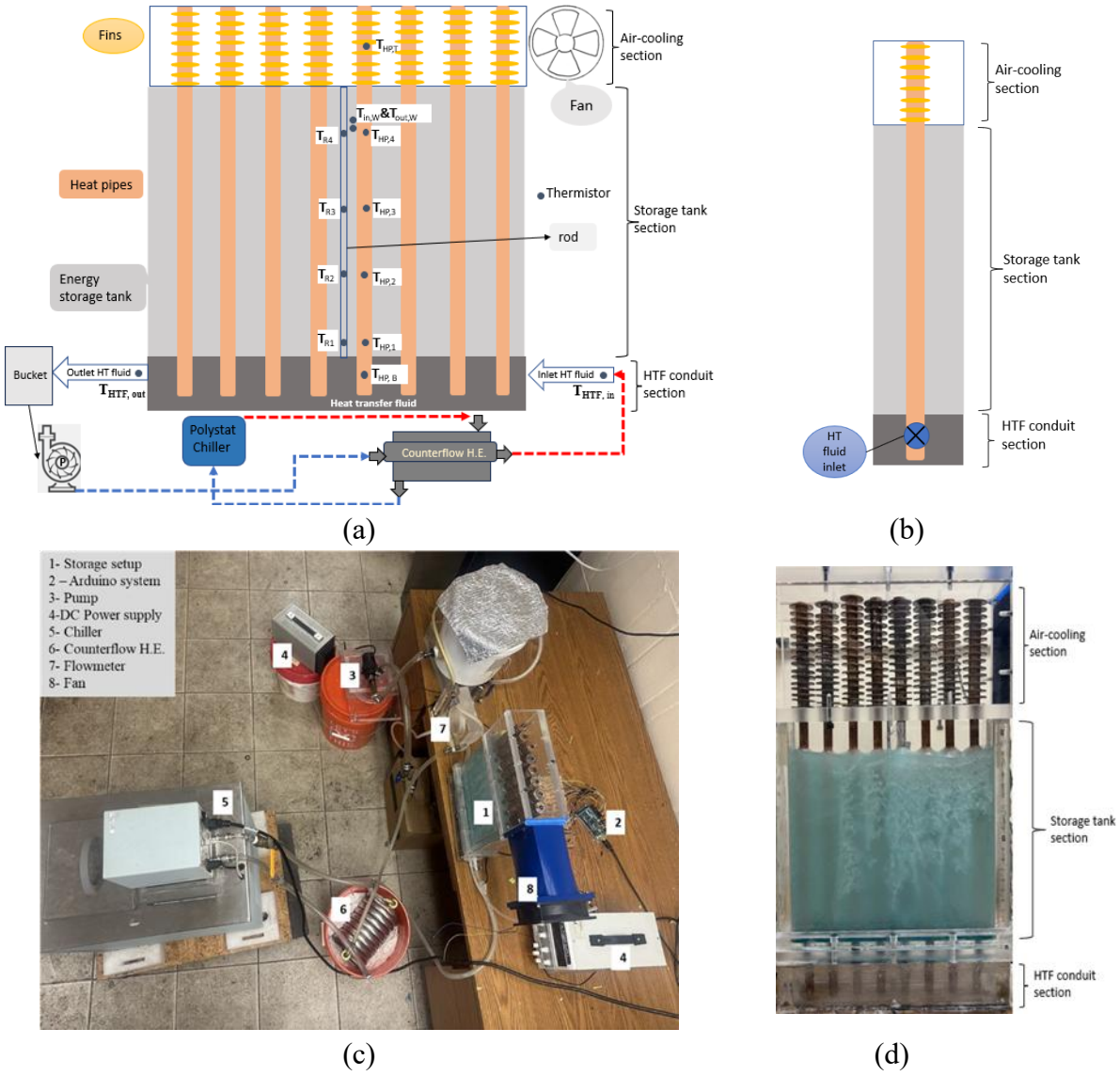

Figure 2-1 Schematic of the experimental setup: a) front, b) side view; and photo of: c) experimental setup, d) key components such as the HTF conduit, PCM storage tank, and air-cooling section

2.1.1 HTF Conduit

Water was used as the heat transfer fluid (HTF) for this experiment. The water conduit was fabricated from a 13-mm-thick acrylic sheet, assembled through adhesive bonding to form inner dimensions of 22cm × 3.5 cm × 5.3 cm. The HTF inlet and outlet ports are 11.2 mm in diameter and symmetrically positioned 18.5 mm above the chamber base. These openings functioned as

inlet and outlet, as shown in the schematic (Fig. 2-1(b)) and actual photograph (Fig. 2-1(c)). Two mass flow rates of water inside the conduit were 8.2 and 5 g/s. A Cole-Parmer variable-area flowmeter was used to measure and maintain a constant HTF flow rate during each test. This configuration enhanced the system's operational integrity and thermal performance during experimental evaluations.

As shown in Fig. 2-1(c), the water exiting the conduit was collected in a bucket and recirculated using a pump (INTG3-552), which is powered by a DC power supply (INSTEK GPS-185000). The water was heated through a custom-designed counterflow helical tube-in-tube heat exchanger. The heating fluid supplied to the heat exchanger was water from a Cole-Parmer Polystat recirculating chiller (CP3211978). The integration of the heat exchanger into the setup ensures precise control of the water temperature at the inlet of the conduit, maintaining consistent thermal conditions throughout the system. Also, using the heat exchanger prevents any PCM that may leak from the storage tank reaching to the chiller, avoiding performance issues.

Eight copper-water HPs (ATS-HP-D10L400S49W-172), each with an outer diameter of 10 mm and a length of 0.4 m, were employed to enhance heat transfer between the water inside the conduit, the PCM in the storage tank, and the air in the air flow conduit. HPs were inherently efficient heat transfer devices capable of passively transferring heat across small cross-sectional areas by utilizing the phase change process of evaporation and condensation of their working fluid [85]. As depicted in Fig. 2, the HPs were arranged in one row of eight HPs. These HPs were positioned within the conduit, ensuring efficient heat transfer communication and maintaining flow segregation. HPs were inserted into the system through the pre-designed holes on the caps of the bottom conduit and storage tank. Silicon sealant was used to seal and secure the HPs. The

spacing of the adjacent HPs was 25 mm, and the clearance of the HPs and water conduit wall was 12.5 mm. The length of HPs inside the water conduit was about 50 mm.

As illustrated in Fig. 2-1(a), a total of fourteen thermistors were installed at strategic locations within the experimental setup to monitor local temperature variations, three water-proof thermistors (GA10K3435DM010) and eleven standard thermistors (SC30F103V). Four thermistors, designated as T_{R1}, T_{R2}, T_{R3}, and T_{R4}, were embedded within the PCM at different vertical positions along the centerline of the storage tank to measure the PCM temperature profile. To secure the thermistors in place, a 2 mm diameter stainless-steel tube was used. Small holes, precisely drilled at intervals of 1 cm, 7 cm, 13 cm, and 18 cm from the tube's end at the bottom of the storage tank, were designed to accommodate the thermistor beads. This configuration allowed the thermistor beads to be accurately positioned within the tank while the connecting wires pass through the tube.

To monitor the surface temperatures of the HPs, six thermistors were installed on one of the middle HPs (the fourth HP from the right side in 2-1(a). Four thermistors, designated as T_{HP1}, T_{HP2}, T_{HP3}, and T_{HP4}, were positioned along the HP surface within the storage tank at vertical distances of 1 cm, 7 cm, 13 cm, and 18 cm from the bottom of the storage tank. Additional thermistors were attached to the HP surface within the water conduit ($T_{HP,\,B}$) and the airflow channel ($T_{HP,\,T}$). The thermistors were secured to the HP surface using aluminum tape to ensure stable positioning and accurate temperature measurement. Two thermistors were attached to the wall of the storage tank at vertical distance of 18 cm to measure the temperature of the inner ($T_{wall,in}$) and outer ($T_{wall,out}$) wall of the storage tank.

The water temperatures at the inlet and outlet of the water conduit were measured using two thermistors, labeled $T_{HTF, in}$, and $T_{HTF, out}$, respectively, embedded in the inlet and outlet tubes connecting to the HTF conduit.

Three HTF inlet temperatures of 45°C, 50 °C, and 55 °C were examined in this study. These temperatures were chosen to evaluate the thermal performance of the HP-PCM CTES system under varying thermal gradients, which are representative of realistic low-grade heat dissipated by data centers and condenser unit of thermoelectric powerplant. These HTF temperatures is in the temperature range of a plant can actually supply (e.g., condenser/return water or waste heat loops) and give a decent ΔT above the PCM melt range so melting is repeatable and quick without overheating the material or stressing seals, wicks, or sensors, and finally keep the heat pipe in a stable, high-conductance regime. Using 5 °C steps provides a clean sensitivity covered. It lets the study quantify how the HTF temperature affects melt time, delivered power, outlet temperature, and the validation of the numerical model. The placement accuracy of the thermistors is approximately ±1 mm.

2.1.2 PCM Storage Tank

In this study, a paraffin based PCM with a melting temperature of approximately 32°C, namely PCM-32 from Microtek [86], was selected as the storage material. While various PCMs with different melting temperatures have been used in the literature, nighttime air temperatures in most hot/arid regions usually drop to about 20–25 °C, creating a sufficient temperature difference for the cold storage process. This operating range is also practical for most of the year, including both summer and winter. Moreover, this PCM is safe for use up to 100°C, is not corrosive,is very stable and readily available.

The storage tank was constructed from a 13-mm thickness acrylic sheet with internal dimensions of 21.5 cm × 22 cm × 3.5 cm (width × height × depth). The tank was assembled using acrylic glue and sealed with silicone sealant to ensure structural integrity and prevent leakage. Eight holes, each with a diameter of approximately 1 cm, were drilled into the top and bottom acrylic walls of the tank to allow the HPs to pass through and be securely positioned. Silicone sealant was applied around the HPs at the entry points to ensure a tight seal. The bottom wall of the tank was coupled with the water conduit, while the top wall was mated with the air-cooling channel. It is noteworthy that the original color of the PCM was clear and transparent; however, as shown in Fig. 2-1(d), it changed to a light blue, possibly due to interaction with the copper HPs. The impact of PCM discoloration on its thermophysical properties was examined by measuring density, and thermal conductivity of the PCM before and after color change, and no noticeable difference was observed. The mass of PCM within the storage tank is about 1.067 kg.

Table 2-1 Thermistors of the experimental set-up

Number	**location**	**Name**
1	Attached to rod, bottom one	T_{R1}
2	Attached to rod, second from the bottom	T_{R2}
3	Attached to rod, third from the bottom	T_{R3}
4	Attached to rod, the top one	T_{R4}
5	Attached to heat pipe, bottom one	T_{HP1}
6	Attached to heat pipe, second from the bottom	T_{HP2}
7	Attached to heat pipe, third from the bottom	T_{HP3}
8	Attached to heat pipe, the top one	T_{HP4}
9	Attached to evaporation part of heat pipe	$T_{HP, B}$

10	Attached to condensation part of heat pipe	$T_{HP,\,T}$
11	Within the inlet hose	$T_{HTF,\,in}$
12	Within the outlet hose	$T_{HTF,\,out}$
13	Attached to the inner wall of storage tank	$T_{wall,\,in}$
14	Attached to the outer wall of storage tank	$T_{wall,\,out}$

2.1.3 Air-Cooling Section

Following the fabrication of the water conduit and the PCM storage tank, an airflow channel was constructed using acrylic sheets and subsequently sealed to ensure airtight operation. The channel has a cross-sectional area of approximately 11 cm × 6 cm. Approximately 10.5 cm of the HPs' length was positioned within the air channel. As shown in Fig. 2-1(c), a 3D-printed connecting piece was fabricated and connected to the air channel to direct airflow from a fan (MS1238E48B1+6-FHR). Air flew through the channel at a speed of approximately 19 m/s.

To enhance convective heat transfer between the air and the HPs inside the air channel, a set of eight copper fin jackets was fabricated and installed on the HPs. Each annular jacket was 11 cm in length with an inner diameter of approximately 10 mm and a wall thickness of 1 mm. A total of 16 annular copper fins, each with inner diameter and outer diameters of 12 mm and of 25 mm, respectively, and thickness of 1.8 mm, were brazed onto the outer surface of each jacket with a spacing of 7 mm. A high-conductivity thermal paste (Noctua, $k \approx 4$ W/m·K) was applied between the HPs and the fin jackets to minimize thermal contact resistance.

The HPs were inserted through pre-machined holes in the top and bottom acrylic walls of the PCM storage tank, ensuring accurate alignment within both the PCM domain and the water conduit. Silicone sealant was used to seal the interface between the HPs and the acrylic walls to

prevent leakage and ensure mechanical integrity, as shown in Fig. 2-1(d). Finally, the airflow channel was assembled onto the system to complete the setup. An Arduino MEGA 2560 was employed as a custom-designed data acquisition system to collect data from the thermistors. The thermistors were calibrated using boiling water and ice water mixture prepared from distilled water to ensure accurate and consistent readings. According to the thermistors manufacturer's data, the uncertainty in the measured temperatures is ± 0.5°C.

Table 2-2 presents the thermophysical properties of PCM, HP, and fins. It should be noted that, since the PCM manufacturer provided only the melting temperature and the latent heat of fusion, other thermophysical properties were directly measured using available laboratory equipment and instrumentation.

Table 2-2 Thermophysical properties of PCM, HP and fin jackets.

	PCM	**HP working fluid**	**HP wall (≈ 0.5 mm) and wick (≈ 1 mm, porosity of 0.9), and fin jackets**	**Conduits and storage tank**
Material	Microtek PCM-32	Water [84]	Copper [87]	Acrylic [87]
Density, ρ (kg/m^3)	819 (solid) 737 (liquid)	996.6 (liquid)	8978	1150
Thermal conductivity, k (W/mK)	0.25 (solid) 0.15 (liquid)	0.613 (liquid) 0.019 (vapor)	387.6	0.2
Specific heat, c_p (kJ/kg K)	2	4181 (liquid) 1882 (vapor)	381	1.47
Viscosity, μ (Pa.s)	0.0045	8614×10^{-7}(liquid) 91.74×10^{-7} (vapor)		
Latent heat of fusion, h_{sl} (kJ/kg)	185[86]			
Latent heat of vaporization, h_{fg} (kJ/kg)		2434.9		
Thermal expansion coefficient, β (K^{-1})	0.00101			

Melting temperature, T_m (°C)	32

2.2 Characterization of PCM Properties

Since the PCM datasheet did not include several key properties, this section outlines the methodologies used to characterize key thermophysical properties of the PCM, including density, thermal conductivity, viscosity, and thermal expansion. Calculating the density, the weight of the melted/solid PCM within a measured beaker were examined and the densities of melted and solid PCM were calculated 737 kg/m3 and 819.5 kg/m3.

2.2.1 Melting and Solidification Points

To determine the melting and solidification temperatures, the PCM was first fully melted and poured into a beaker, which was then placed in a temperature-controlled water bath (Polystat chiller, cp321978). For solidification testing, the bath temperature was gradually decreased by 1°C per hour, starting from 33°C, to ensure thermal equilibrium between the PCM and the surrounding water. The onset of solidification was identified visually and recorded at approximately 31°C.



Figure 2-2 different stages of solidification of PCM using Polystat chiller and measured beaker.

A similar procedure was followed for the melting temperature measurement: the solidified PCM was subjected to a gradual increase in water bath temperature from 31°C, again

in 1°C increments per hour, until the onset of melting was observed. The melting temperature was found to be approximately 33°C, as depicted in Fig. 2-2.



Figure 2-3 different stages of Melting of PCM using Polystat chiller and measured beaker.

2.2.2 Viscosity of the PCM

The viscosity of the PCM was measured using a Brookfield Ametek viscometer (DV1MLVTJ0). To enhance precision for low-viscosity fluids, particularly when the viscosity is below 10 cP, a UL adapter was utilized. The PCM temperature was carefully regulated using a temperature-controlled water bath chiller, allowing for precise control near the melting point. As the PCM approached its melting temperature (~33°C), the measured viscosity stabilized at approximately 4.48 cP or 0.00448 Pa·s (±2%). This value was selected as the representative viscosity of the PCM in its molten state. It is important to note that further reduction in temperature beyond this point risked the formation of solid particles within the sample, which could compromise the accuracy of the viscosity measurements due to partial phase change.



Figure 2-4 measuring the viscosity of PCM using Brookfield Ametek viscometer.

Table 2-3 PCM viscosity at different temperatures

Working Temperature (°C)	Viscosity (cP)
40	3.83
35	4.28
34	4.39
33	4.48

2.2.3 Thermal Conductivity of the PCM

The thermal conductivity of the PCM was evaluated using a C-Therm thermal conductivity analyzer (TCi-3-A). Given the ambient room temperature of approximately 22 °C and the solidification temperature of the PCM near 32 °C, the C-Therm sensor was placed on a temperature-controlled hot plate to ensure the PCM remained in the liquid phase during testing.

To ensure the accuracy and reliability of the C-Therm system in conjunction with the hot plate, preliminary validation tests were conducted using water as a reference fluid. Once validated, thermal conductivity measurements were performed on the liquid PCM, yielding an average value of 0.145 W/m·K. Following this, the hot plate was deactivated, and the PCM was allowed to fully solidify under ambient conditions. After sufficient time had elapsed to ensure complete

solidification, the thermal conductivity of the solid PCM was measured and found to be approximately 0.25 W/m·K. Fig. 2-5 shows the set-up of measuring the thermal conductivity for liquid/solid PCM.



(a) (b)

Figure 2-5 a) The set up of measuring the thermal conductivity for liquid PCM, b) solid PCM by C-Therm system.

2.2.4 Thermal Expansion Coefficient of PCM

The thermal expansion coefficient (β) of the PCM was determined experimentally by monitoring the volumetric change of the liquid PCM over a specified temperature range. The PCM was initially poured into a calibrated glass beaker, and its volume was recorded at a stabilized temperature of 41 °C, maintained for approximately 20 minutes to ensure thermal equilibrium. The temperature was measured using a thermocouple centrally placed within the PCM. At this condition, the PCM volume was measured as 30.0 mL. Subsequently, the PCM was heated to a temperature of 70.8 °C and held for about 30 minutes to allow for full thermal expansion. Under these conditions, the PCM volume increased to 30.9 mL. Based on the observed volumetric change and corresponding temperature difference, the volumetric thermal expansion coefficient was calculated using:

$$\beta = \frac{\Delta V/V_0}{\Delta T} = \frac{(30.9 - 30.0)/30.0}{70.8 - 41} \approx 0.00101\ K^{-1} \quad (1)$$

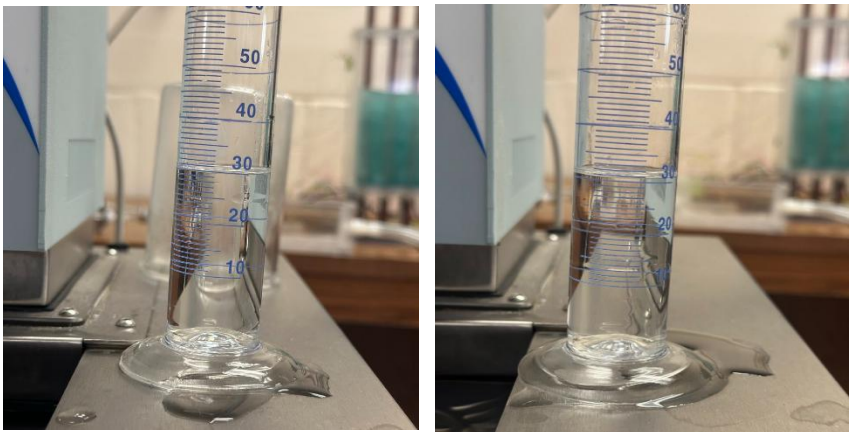

V = 30 ml @41 ºC V = 30.9 ml @70.8 ºC

Figure 2-6 measurements of thermal expansion coefficient using chiller and measured beaker.

2.3 Experimental Procedure

To fill the setup with PCM and prepare it for experimentation, the setup was first leveled to ensure uniform filling and proper alignment. Approximately 1.07 kg of PCM was melted in a beaker placed inside a water bath, CPX3800H, with the water bath temperature set to 60 °C. Once the PCM was fully melted, it was carefully poured into the storage tank through the opening on the top acrylic wall using a funnel. Initially, about one-third of the total PCM volume was introduced into the tank. The setup was then allowed to cool naturally under ambient air condition ($T_{air} < T_m$) for about 2 hours to solidify the PCM. Once the initial layer of PCM had solidified, the pouring and solidification process was repeated once more to add all the PCM to the storage tank, reaching a final height of 19 cm from the bottom of the tank. To accommodate the expansion of the PCM upon melting during later experimentation, an air gap of approximately 2.5 cm was maintained within the storage tank.

In the context of CTES systems utilizing PCM, the charging process involves storing cold energy by solidifying the PCM, removing latent heat from the liquid PCM, effectively "charging" it with cold energy. During the discharging process, this stored cold energy is released as the PCM absorbs heat from a warmer environment and undergoes melting. In the present system configuration, cold energy is delivered by a stream of relatively cold ambient air flowing through the airflow channel, which extracts heat from the PCM via embedded HPs. These HPs, in turn, draw thermal energy from the relatively warm water circulating within the water conduit, thereby facilitating indirect cooling of the water via the cold-stored PCM.

This study experimentally investigates two distinct operational scenarios: (i) the melting process, representing the discharging phase, and (ii) the solidification process, representing the charging process.

The temperature of PCM returned to ambient temperature before each test as tests were done in separate days, and the entire system had sufficient time to reach thermal equilibrium. The inlet water temperature was controlled using the chiller and the counterflow heat exchanger described earlier in the HTF conduit section. The chiller set point was adjusted to establish the desired inlet water temperature at the conduit entrance. After the water temperature stabilized at the target value, the water flow was introduced into the conduit, marking the start of the discharging (melting) experiment. Temperature data were recorded at a 1-Hrtz frequency using the data acquisition system. To monitor the progression of the melting process, photographs were taken at intervals of approximately 10 minutes. Each melting experiment was concluded when the PCM was fully melted.

The charging (solidification) process was initiated immediately after the completion of the discharging process, with the PCM in a fully melted state. The water circulation in the conduit was

stopped, and the fan was switched on. Heat was extracted from the PCM to the relatively cold air via the HPs, causing the PCM to gradually solidify. Temperature data were continuously collected throughout the solidification process, and photographs were taken at regular intervals to document the progression. The charging experiments were concluded once the PCM had completely solidified.

Chapter 3. Experimental Analysis

Experimental analyses were conducted to determine the energy efficiencies of both the charging and discharging processes. The control volume was defined to include the acrylic storage tank, PCM, and HPs. The energy balance of the system was evaluated by applying the first law of thermodynamics (conservation of energy) to the defined control volume during each operational phase.

3.1 Discharging Process (Melting)

The energy conservation equation for the defined control volume is expressed as follows:

$$Q_{tot} = Q_{pcm} + Q_{wall} + Q_{sen,HP} + Q_{loss,HP} + Q_{loss} \quad (2)$$

where, Q_{tot} represents the total amount of thermal energy extracted from the circulating warm water within the water conduit throughout the entire melting period (0 to $t_{stop,\ disch}$).

$$Q_{tot} = \int_0^{t_{stop,disch}} \dot{m}_{HTF} c_{HTF} \left(T_{HTF,in} - T_{HTF,out}\right) dt \quad (3)$$

The total energy absorbed by PCM, Q_{PCM}, is the sum of its sensible and latent heat components:

$$Q_{PCM} = Q_{PCM,sen} + Q_{PCM,\ lat} \quad (4)$$

where

$$Q_{PCM,sen} = Q_{PCM,sen,s} + Q_{PCM,sen,l} = m_{PCM} C_{PCM,s} (T_m - T_i) + m_{PCM} C_{PCM,l} \left(T_m - T_{stop,disch}\right) \quad (5)$$

Here, T_i and $T_{stop,disch}$ represent the average temperatures measured by thermistors T_{R1} through T_{R4} at the start and end of the discharging process, respectively. T_i corresponds to the initial temperature of the solid PCM at the beginning of the experiment, while $T_{stop,disch}$ denotes the

temperature of the fully melted PCM at the conclusion of the discharging period. The latent heat absorbed by the PCM is:

$$Q_{PCM,lat} = m_{PCM} h_{sl} = 1.07kg \times 185 \frac{kJ}{kg} = 197.4kJ \quad (6)$$

The energy stored within all acrylic walls of the setup at $t_{stop,\ disch}$ is:

$$Q_{wall} = m_{wall} C_{wall} (T_{wall} - T_i) \quad (7)$$

which is around 117.5 kJ for the case with $T_{HTF,in}$ = 50°C and $\dot{m}_{HTF}$ = 8.2 g/s. The heat absorbed by all HPs and fin jackets due to their thermal mass during discharging, denoted as $Q_{sen,HP}$, is based on the total mass of HPs and fins (around 1.6 kg) and temperature difference of the start and end of discharging.

$$Q_{sen,HP} = m_{HPs\ \&\ fins} C_{Copper} \left(T_{stop,disch} - T_i\right) \quad (8)$$

The total heat absorbed by all HPs and fin jackets due to their thermal mass calculated to be around 15kJ for the case with $T_{HTF,in}$ = 50°C and $\dot{m}_{HTF}$ = 8.2 g/s. Additionally, the heat loss from the fin jackets to the stagnant air within the airflow channel up to $t_{stop,disch}$ is accounted for by estimating convective losses based on the local temperature difference and heat transfer coefficient.

$$Q_{loss,HP} = h_{NC,fin} A_{fin} \left(T_{fin} - T_{air}\right) \quad (9)$$

Here, $h_{NC,fin}$, A_{fin}, and T_{fin} represent the natural convection heat transfer coefficient between the jackets exposed to the airflow channel, the total inner surface area of the fin jackets within the airflow domain, and the surface temperature of the fin jackets at up to t_{disch}, respectively. To determine $h_{natural,fin}$ of the jacket, the correlation for natural convection over vertical cylindrical surfaces proposed by Churchill and Chu [88] was used. It should be noted that the additional surface area provided by the fins was also included in the calculations [89]. The total heat loss

from the fin jackets to the ambient air via natural convection is estimated to be approximately 18.3 kJ for the case with $T_{HTF,in}$ = 50°C and $\dot{m}_{HTF}$ = 8.2 g/s.

The corresponding heat loss from the external surfaces of all acrylic walls to the ambient air is given by:

$$Q_{loss,acrlic} = \sum h_{air} A_w \left(T_{w,out} - T_{air}\right) \quad (10)$$

The heat loss from the acrylic walls is calculated based on the convective heat transfer from the outer side of the walls including storage tank and water conduit, taking into account the temperature difference between the outer surfaces of the wall for each section of the setup and ambient temperature measured at the start of each test. The same approach for calculating natural convective coefficient for the vertical cylinder was used for estimating h_{air} for the vertical walls of storage tank and HTF conduit. The heat loss, $Q_{\text{loss,acrlic}}$, is estimated to be approximately 35.45 kJ during the discharge up to $t_{stop,disch}$ for the case with $T_{HTF,in}$ = 50°C and $\dot{m}_{HTF}$ = 8.2 kg/s.

3.2 Charging Process (Solidification)

Equation (1) remains applicable for the charging (solidification) process, with the following modifications: Q_{total} represents the total amount of heat extracted from the PCM during the solidification phase, transferred through the HPs to the cold air flowing within the airflow channel at the conclusion of the charging process, denoted as $t_{stop,\ ch}$. Additionally, $Q_{loss,\ HP}$ refers to the heat transferred from the HPs to the stationary air within the empty water conduit during this phase. It is important to note that the water inside the conduit was emptied before the charging process began, and no water was circulating during this phase.

$$Q_{loss,HP} = h_{natural,HP} A_{HP} \left(T_{HP} - T_{HTF,in}\right) \quad (11)$$

where $h_{natural,\ HP}$ is the natural convection heat transfer coefficient between the HP surfaces and the stationary air within the water conduit, A_{HP} is the surface area of the HPs within the water conduit, and T_{HPT} is the surface temperature of the HPs within the water conduit , Tair is the stationary air temperature within the conduit. The total heat released from the HPs to the air through natural convection is estimated to be about 8 kJ for the case $T_{HTF,in}$ = 50°C and $\dot{m}_{HTF}$ = 8.2 kg/s. The heat loss from the external surfaces of all acrylic walls to the ambient air is given by:

$$Q_{loss} = \sum h_{air} A_w \left(T_{w,out} - T_{air}\right) \tag{12}$$

The total heat transfer to ambient from the acrylic walls of the storage tank during the solidification estimated around 18.5 kJ for the case $T_{HTF,in}$ = 50°C and $\dot{m}_{HTF}$ = 8.2 g/s.

The overall performance of the latent heat storage system can be evaluated through its thermal resistance, which reflects how effectively heat is transferred from the HTF to the PCM. A lower thermal resistance indicates more efficient heat exchange and faster energy storage within PCM. In this study, the thermal resistance of the system during the melting process was determined using the following relation:

$$R = \frac{\Delta T \times \Delta t}{Q_{tot}} \tag{13}$$

where ΔT represents the average temperature difference between the inlet and PCM average (average of T_{R1}, T_{R2}, T_{R3}, and T_{R4}) temperature during the total melting period, Δt is the duration of the melting process, and Q_{PCM} denotes the total heat transferred to the PCM in that interval. This term provides a simple way to capture the combined influence of the driving temperature difference, time, and heat input on the performance of the system. A smaller value of R corresponds to a more efficient thermal interaction between the HTF and PCM, as heat is transferred more

readily through the system. Conversely, a higher thermal resistance suggests slower energy exchange, which may result from reduced convection, weaker thermal contact, or lower conductivity within the storage medium. Similarly, for discharging process ΔT represents the temperature difference of the ambient temperature through cooling process and the average temperature within the PCM reservoir, Δt is the duration of solidification process, and Q denotes the total heat transferred from PCM.

It should be noted that the calculations for both the charging and discharging processes were performed for each experimental case, corresponding to the different HTF inlet temperatures of 45°C, and 50°C and 55°C, and two different HTF mass flow rates of 8.2 g/s, and 5 g/s.

Chapter 4. Numerical Model and Mathematical Formulation

A three-dimensional numerical model was developed using ANSYS-FLUENT 2023 to investigate the underlying physical mechanisms of the system, providing insights beyond those achievable through experimental studies alone. This model also supported optimization of the setup's design and performance. The transient enthalpy-porosity technique was employed to simulate phase change behavior. The governing conservation equations for mass, momentum, and energy were fully solved across the entire computational domain. The heat transfer processes were influenced by transient and coupled effects, including: (i) conduction through solid components such as the fins and the walls and wicks of the HPs, (ii) vaporization, condensation, and the flow of the HPs' working fluid, (iii) natural convection within the PCM during phase transitions, and (iv) forced convection in the air-cooling section and the water conduit of the setup. A User-Defined Function (UDF) was implemented in FLUENT for detailed modeling of HPs.

4.1 Physical Domain and Computational Grid

The complete computational domain is illustrated in Fig. 4-1, with detailed dimensions provided in Table 4-1. The domain exhibits symmetry along the mid x-z plane, as indicated in Fig. 4-1.

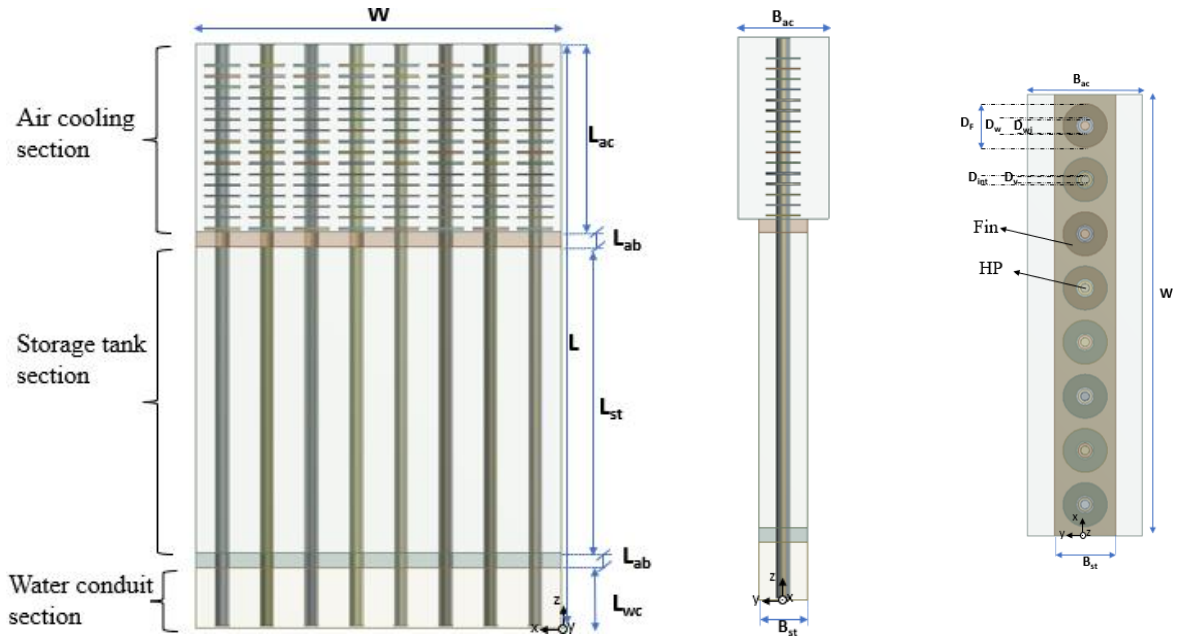

(a) (b) (c)

Figure 4-1 Complete computational domain of the CTES system: (a) front view, (b) side view, (c) top view.

Table 4-1 Complete computational domain dimensions.

Symbols	Dimensions (cm)
L	40.6
W	22
B_{ac}	6.1
B_{st}	3.5
L_{wc}	5
L_{st}	21.5
L_{ac}	11.5
Lab	2.6
D_F	2.8
D_w	1
D_{wi}	0.8
D_{int}	0.5
D_v	0.49

L_{wc}: length of the HPs within the water conduit section

L_{st}: length of the HPs within the storage tank section

L_{ac}: length of the HPs within the air-cooling section

L_{ab}: length of adiabatic section of the HPs

To simplify the numerical simulation of the melting and solidification of the HP assisted CTES, the average convective heat transfer coefficients between the finned HPs and air as well as between the HPs and water were determined separately. Calculation of the heat transfer coefficients was done in two parts. In the first part, airflow over the finned HPs within the airflow channel was simulated to determine the average convective heat transfer coefficients. The computational domain for this part is shown in Fig. 4-2(a). Due to symmetry along the x–z plane, only half of the physical domain was modeled, which included four HPs. The average convective heat transfer coefficients obtained from this simulation were uniformly applied as convective thermal boundary conditions on the exterior surfaces of the fin jacket exposed to the airflow within the computational domain shown in Fig. 4-2(a).

In the second part, the water conduit section of the setup was simulated. The computational domain for this part is illustrated in Fig. 4-2(b). Similar to the first component, symmetry along the x–z plane allowed for the modeling of only half of the physical domain, which included half of HPs. The average convective heat transfer coefficients obtained from this simulation were uniformly imposed as convective thermal boundary conditions on the exterior surfaces of the HPs exposed to the water flow inside the water conduit, as represented in the computational domain in Fig. 4-2(a). Solid rods were used exclusively in these two computational domains for two reasons: i) the HPs temperatures are fairly uniform in the air and water conduits, and ii) the convective heat transfer coefficients are insensitive to small changes in temperatures. However, in the computational domain shown in 4-2(a), HPs were considered instead of solid rods.

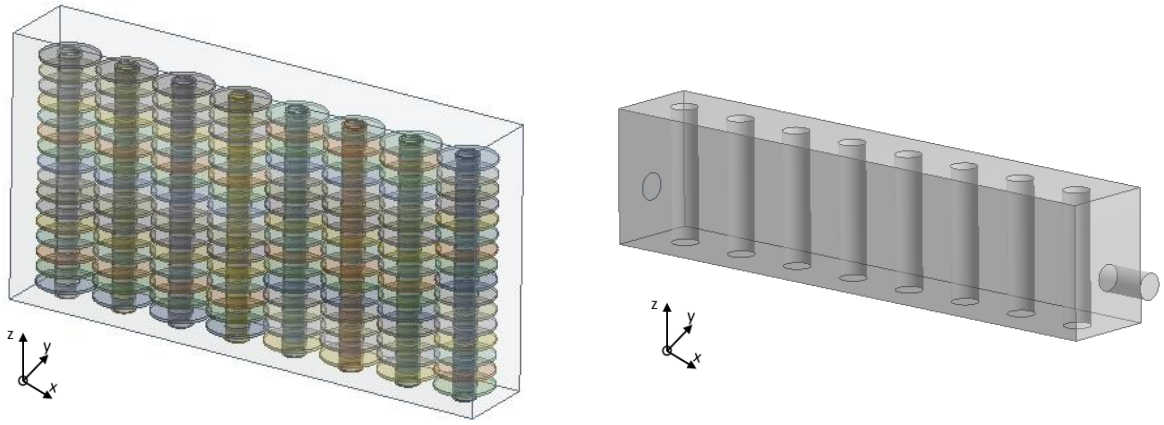

(a) (b)

Figure 4-2 Computational domains: (a) Air-cooling section of the setup; (b) Water conduit section of the setup. Flow direction is along the x-axis.

The model was developed based on several key assumptions. All thermophysical properties were treated as constant, except for the vapor phase of the HP working fluid, which was modeled as an ideal gas with a density that varies as a function of both temperature and pressure. The PCM was assumed to be pure, and the density of the molten PCM was considered identical to that of the solid phase. However, it was assumed that the thermal conductivity of the solid and liquid PCM phases differs. Natural convection within the molten PCM was modeled using the Boussinesq approximation and discharge simulations began with a laminar flow assumption. As the Rayleigh number in the vertical annular PCM–HP configuration stays below 10^6 (based on the gap thickness, height of HPs in contact with PCM, and temperature difference of the HPs and PCM melting point), the flow regime remains laminar natural convection[90]. Thermal radiation was neglected due to the relatively low operating temperatures. The vapor phase of the HPs' working fluid was modeled as, laminar, and incompressible flow, with the wick assumed to be fully saturated. At the wick-vapor interface, both the vapor and liquid phases of the working fluid were considered to be in thermodynamic equilibrium. It was also assumed that the porous wick generated sufficient capillary pressure to sustain the liquid flow through the wick under the operating conditions of this study.

The computational domain, as shown in Fig. 4-1(a), is delineated by multiple physical boundaries that separate various materials, and components within the conjugate system. Thermal contact resistances were ignored. The system is governed by specific boundary and initial conditions. Symmetry conditions were applied along the mid x–z plane of the setup. During the discharging process, the surface temperature of the HPs within the water conduit was set equal to the HTF average temperature ($T_{HTF,\ in}$ and $T_{HTF,\ out}$). The convection heat transfer coefficient, obtained from the computational domain shown in Fig. 4-2(b), was uniformly applied to the external surfaces of the HPs within the water conduit. All external surfaces of the fin jackets located in the airflow channel were assumed to be adiabatic. Conversely, during the charging process, the convection heat transfer coefficient derived from the computational domain shown in Fig. 4-1(a) was uniformly applied to the external surfaces of the fin jackets within the airflow channel. The external surfaces of the HPs located within the water conduit were considered adiabatic to account for the absence of circulating water.

The remaining external boundaries were treated as adiabatic and impermeable, with no-slip conditions applied to the fluid flow. The initial temperature throughout the entire domain was set to the ambient laboratory temperature of T_i.

Computational grid

Achieving accurate simulations, the quality of the mesh is very important, especially for the small area of interface inside the heat pipe where the wick and vapor area are detached. It was tried to make a structural mesh for the whole domain study for more accurate results and better convergency. A dense mesh was provided at the regions of interface that are small and needs smaller elements to be captured. Trying to decrease the time and cost of simulations, half of the domain study was considered for simulations and symmetry conditions were applied. The grid

used for the simulations of the symmetry case is shown in Fig. 4-3. The number of grids for the domain study is around 315000 elements.

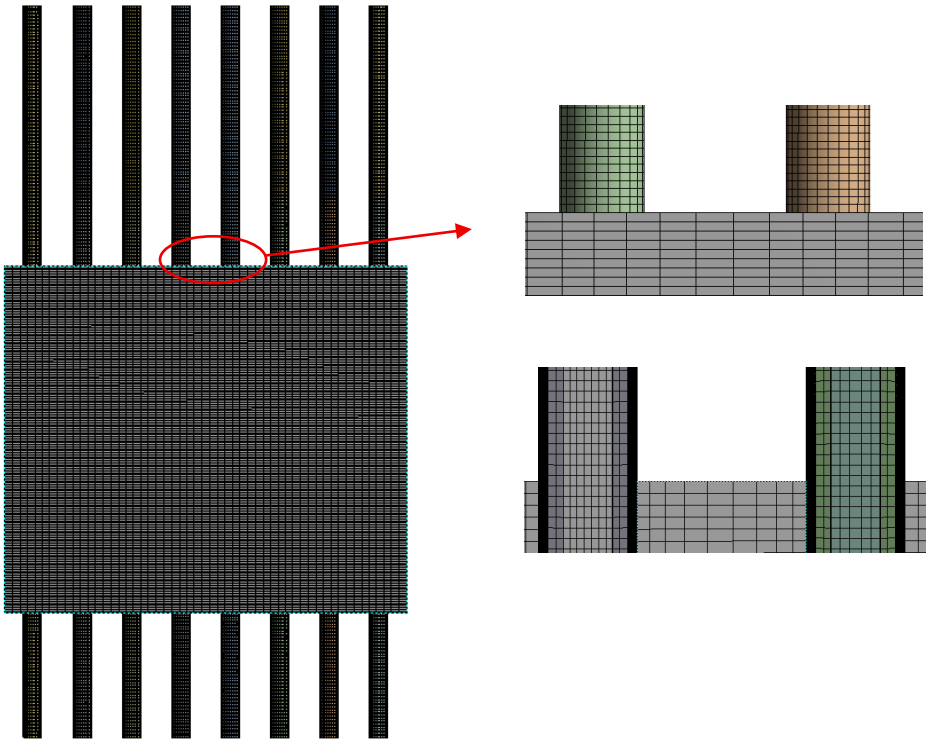

Figure 4-3 The grid used for simulations.

4.2 Descriptive Equations for the Heat Pipe

The transport of vapor within the HP can be mathematically represented by the following equations [84]:

$$\frac{\partial \rho_v}{\partial t} + \nabla \cdot (\rho_v \vec{u}) = 0 \tag{14}$$

$$\frac{\partial (\rho_v \vec{u})}{\partial t} + \nabla \cdot (\rho_v \vec{u}\vec{u}) = -\nabla p + \mu \nabla^2 \vec{u} \tag{15}$$

$$\rho_v c_{p,v} \left(\frac{\partial T}{\partial t} + \vec{u} \cdot \nabla T\right) = k(\nabla^2 T) \tag{16}$$

The ideal gas law is used to determine the vapor density as a function of its pressure and temperature.

$$\rho = \frac{P}{R_g T} \tag{17}$$

where R_g represents the specific gas constant. The compressibility factor was found to be approximately 0.99 and remained nearly constant throughout the operating conditions of this study, thereby validating the assumption of ideal gas behavior for water vapor within the HP.

A UDF was implemented to account for the transmission of the local mass transfer rate due to evaporation and condensation at the wick-vapor interface., as well as the temperature distribution within this region and along the walls at the interface between the vapor zone and the wick. At the vapor-wick interface, the saturation pressure and temperature are correlated using the Antoine equation, which is derived from the Clausius-Clapeyron equation. The explicit temperature-based form of the Antoine equation can be expressed as [91]:

$$T_{v,i} = T_{sat}\left(P_{v,i}\right) = \frac{1730.63}{8.07 - \log P_{v,i}} - 233.42 \tag{18}$$

The variable $T_{v,i}$ denotes the saturation temperature at the inner part of the wick-vapor interface. The constants A, B, and C are associated with the working fluid, which in this case is water, and their values are: A = 8.07, B = 1730.63, and C = 233.42. Additionally, the mass of the vaporized fluid within the evaporator section of the HP was calculated and incorporated as a source term in the energy equations for the vapor control volumes at the interface. The UDF used in these simulations is divided into multiple sections. The initial section determines the vapor temperature in both the interface and vapor regions of the HP, accounting for the pressure in these zones. The heat flux within the interface zone is then used to calculate the mass of condensed vapor in this region. This calculation was performed by applying the equation [84]:

$$q''_{interface} = \left(\dot{m}h_{fg}\right)_{interface} = (\rho_v v_v h_{fg})_{interface} \quad (19)$$

It is assumed that the wick zone of the HP is fully saturated with liquid water. The heat conduction equation governing all solid components of the HP can be expressed as:

$$\frac{\partial(\rho c_p)_w}{\partial t} = k_w \nabla^2 T \quad (20)$$

4.3 Descriptive Equations for the PCM

To model the phase change phenomenon of the PCM, the fundamental conservation equations must be solved throughout the computational domain. The numerical approach used to address the phase change process is the enthalpy-porosity method, where the solid-liquid mushy zone is treated as a porous medium. The governing balance equations for mass, momentum, and energy are as follows [92]:

$$\nabla \cdot \vec{u} = 0 \quad (21)$$

$$\frac{\partial \vec{u}}{\partial t} + \nabla \cdot (\vec{u}\vec{u}) = -\left(\frac{1}{\rho}\right)\nabla p + \nu \nabla^2 \vec{u} + \frac{S_b + S_h}{\rho} \quad (22)$$

$$\frac{\partial h}{\partial t} + \vec{u} \cdot \nabla h = k/\rho(\nabla^2 T) \quad (23)$$

In the above equations, $\vec{u}$ represents the velocity vector, P denotes the pressure, $\vec{g}$ is the gravitational acceleration vector, T stands for the temperature, C is the heat capacity, μ is the viscosity, ρ is the density of the liquid PCM, and k refers to the thermal conductivity. The density gradient, which varies with temperature, contributes significantly to natural convection, which is a dominant heat transfer mechanism in the liquid phase of PCM. In contrast, the conduction term is predominant in the solid phase of the PCM and HPs. To account for the temperature dependence of density, the

Boussinesq approximation is employed, where the density is treated as a constant in all equations except for the buoyancy term in the momentum equation [93].

$$S_b = \rho_{ref} g\beta(T - T_{ref}) \tag{24}$$

The enthalpy term in the energy equation can be formulated as follows:

$$h = h_s + h_l = h_{ref} + \int_{T_{ref}}^{T} C_p dT + \alpha L \tag{25}$$

Where, h_{ref} represents the enthalpy of the solid phase at the initial PCM temperature. The latent heat, $h_l = \alpha L$, varies between 0 when the PCM is in solid state and reaches L when the PCM is in the liquid state. This variation is essential for accurately modeling the phase change behavior of PCM. The fourth term in the momentum equation represents a source term that accounts for the momentum sink in the x and y directions. This effect is due to the reduced porosity in the mushy zone, where the PCM undergoes a transition from solid to liquid, impacting the flow characteristics and energy transport within the material.

$$S_h = A(\alpha)\vec{u} \tag{26}$$

The porosity function, denoted as $A(\alpha)$, is defined as:

$$A(\alpha) = \frac{A_{mushy}(1-\alpha)^2}{\alpha^3 + \varepsilon} \tag{27}$$

where $Amushy$ is the constant associated with the mushy zone which was set to 500000 provided a satisfactory agreement with the experimental data; $\varepsilon = 0.001$. The liquid volume fraction, denoted as α, is defined as:

$$\alpha = \begin{cases} 0 & T < T_s \\ \dfrac{T - T_s}{T_l - T_s} & T_s \leq T \leq T_l \\ 1 & T > T_l \end{cases} \tag{28}$$

Chapter 5. Results and Discussion

After providing a comprehensive explanation of the experimental design, procedure, and the underlying physical model, the results from both experimental and numerical analyses are presented and discussed in this section. It is organized into two subsections: the first addresses the experimental results, analyzing the data obtained from physical tests, while the second focuses on the numerical results derived from computational simulations. A comparative analysis is conducted to evaluate the performance of the HP–PCM cold storage system.

5.1 Experimental Results

Each experiment was conducted two/three times on separate days to assess the repeatability of the results and evaluate the impact of initial temperature variations on the outcomes. The detailed experimental procedures are described in the experimental procedure section. The initial temperature for each trial was approximately 19°C, with a variation of ±1C. Minor discrepancies were observed between the two sets of results, with instantaneous temperature measurements differing by no more than 1°C. The experimental data presented in this study represent the average values derived from both trials to ensure accuracy and reliability.

5.1.1 Results for HTF Temperature of 55 °C

Two experimental trials were performed on September 6, 2025, and September 26, 2025, using an inlet HTF temperature of $T_{\mathrm{HTF,\,in}}$ = 55 °C. The initial average temperature of the PCM for these trials was approximately T_{i} = 19.5°C.

Figure 5-1 depicts the temperature distributions at various locations within the system for $T_{\mathrm{HTF,\,in}}$ = 55 °C at $\dot{m}_{HTF}$ = 8.2 g/s. During the melting phase, the cylindrical region surrounding the

HPs is the first to undergo phase change, as indicated by a rapid temperature increase in this area immediately after the test begins. As depicted in Fig. 5-1(a), the temperature of the HPs rises sharply, quickly reaching the HTF temperature as evaporation occurs within the HPs. Concurrently, thermistors embedded within the PCM capture a gradual temperature rise at different spatial points. Initially, heat transfer is predominantly governed by conduction, leading to a uniform temperature increase across the PCM height. As melting progresses, natural convection becomes the dominant mechanism, with the heated molten PCM rising and accelerating the phase transition from the top downward.

This process is distinctly reflected in thermistor readings. The first thermistor to register a sharp temperature increase is T_{R4}, positioned at the top of the rod, corresponding to the onset of melting in that layer. Subsequently, T_{R3}, T_{R2}, and T_{R1} exhibit similar sharp temperature rises as melting propagates downward. The thermistor positioned at the HTF inlet maintains a constant temperature of 55°C throughout the process, whereas the outlet thermistor records a slightly lower temperature, approximately 2.8°C lower, due to heat exchange.

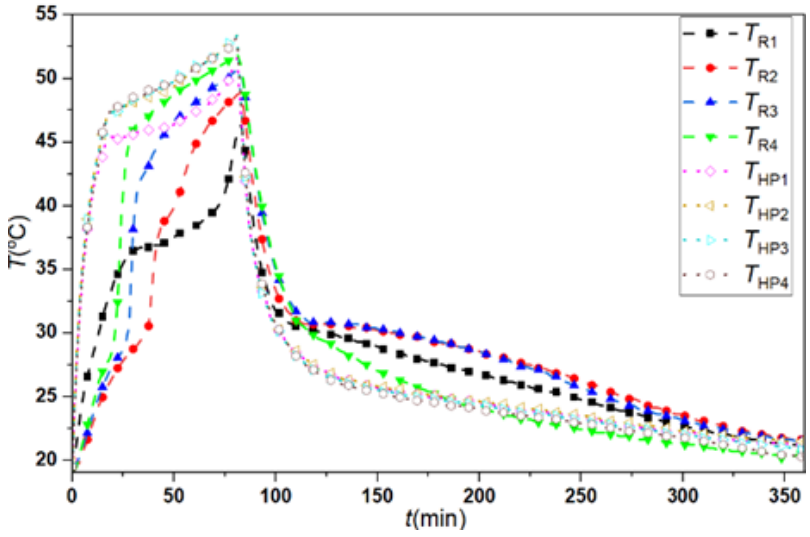

(a)

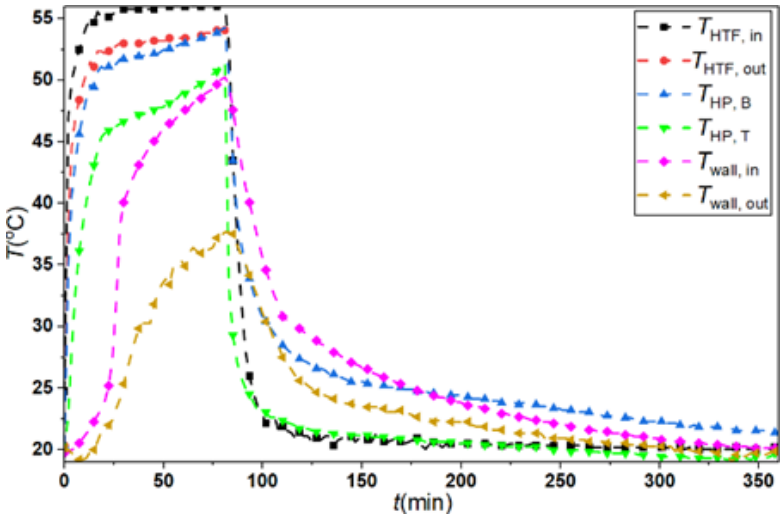

(b)

Figure 5-1 Local temperature histories for $T_{\text{HTF, in}}$ = 55 °C and $\dot{m}_{HTF}$ = 8.2 g/s for. (a) Melting (discharging) and Solidification (Charging) of a) within the storage tank thermistors and, (b) outer storage tank thermistors

5.1.2 Results for HTF Temperature of 50 °C

Three experimental trials were performed on September 5 and September 22, September 23 2024, using an inlet HTF temperature and mass flowrate of $T_{\text{HTF, in}}$ = 50 °C and $\dot{m}_{HTF}$ = 8.2 g/s. The initial average temperature of PCM for these trials was approximately T_i = 19°C.

Figure 5-2 presents the local temperature variations at different locations within the setup for $T_{\text{HTF, in}}$ =50 °C at $\dot{m}_{HTF}$ = 8.2 g/s. The overall trends observed in this case are consistent with those recorded for the scenario where $T_{\text{HTF, in}}$ =55 °C, except for the melting and solidification times. In this case, it took around 111 minutes for the entire PCM to melt, which results from decreasing the HTF inlet temperature by 5 °C. Sensible heat transfer from the liquid PCM to the heat pipes lasted approximately 28 minutes, less than the corresponding period for $T_{HTF,in} = 50°C$ (32 minutes). As shown in Fig. 5-2(a), the average temperature measured by the thermistors located on the rod (T_{R1}, T_{R2}, T_{R3}, and T_{R4}) at the time of complete melting is lower than that in the $T_{HTF,in} = 55°C$ case. Therefore, it was expected that the sensible heat transfer from the melted PCM would

take less time. Furthermore, the temperature difference between $T_{HTF,in}$ and $T_{HTF,out}$ is lower in this case, indicating a lower heat transfer rate from the HTF to the heat pipes due to the decreased inlet temperature.

Melting is completed in approximately 111 minutes, after which HTF circulation ceases, and a fan is activated. This transition is marked by a sharp temperature drop in the thermistors located on the HPs, except for the thermistor in the condensation section at the top of the HP, which maintains a steady temperature. During the initial stage of solidification, the thermistors embedded in the PCM display a rapid temperature decline, indicating sensible heat transfer from the liquid PCM to the HPs over approximately 28 minutes. Beyond this point, the temperature decrease becomes more gradual as the phase change process stabilizes. Solidification initiates in the vicinity of the HPs, as illustrated in Fig. 5-4, forming a cylindrical solid zone that expands progressively to encompass the entire storage tank. Throughout this phase, the PCM transitions through a mushy zone, existing in a mixed solid-liquid state. The majority of the solidification process occurs within 100 minutes, after which the rate of phase change slows significantly, proceeding at a microscale that is not visually discernible.

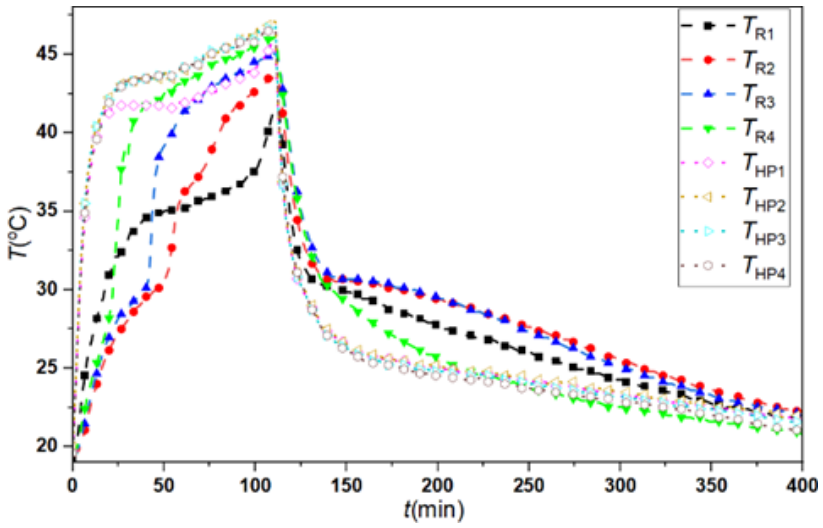

(a)

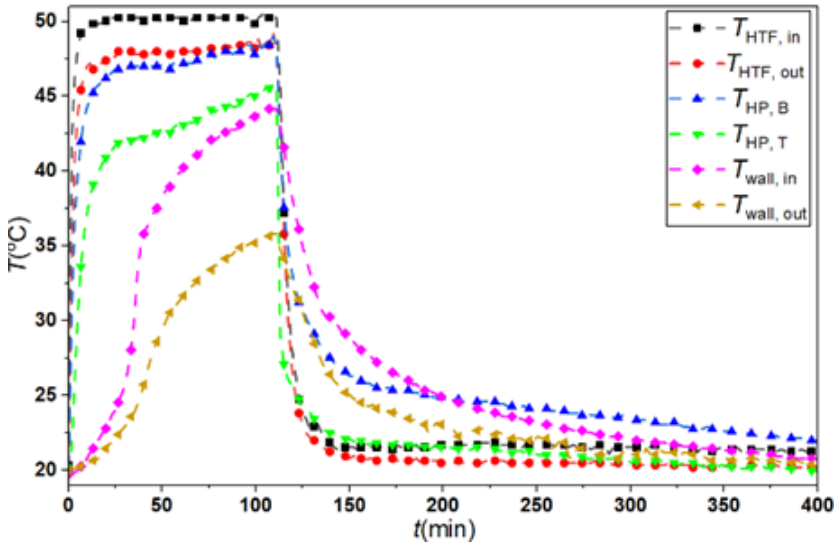

(b)

Figure 5-2 Local temperature histories for $T_{HTF, in}$ = 55 °C and $\dot{m}_{HTF}$ = 8.2 g/s for melting (discharging) and solidification (Charging) of a) within the storage tank thermistors and, (b) outer storage tank thermistors

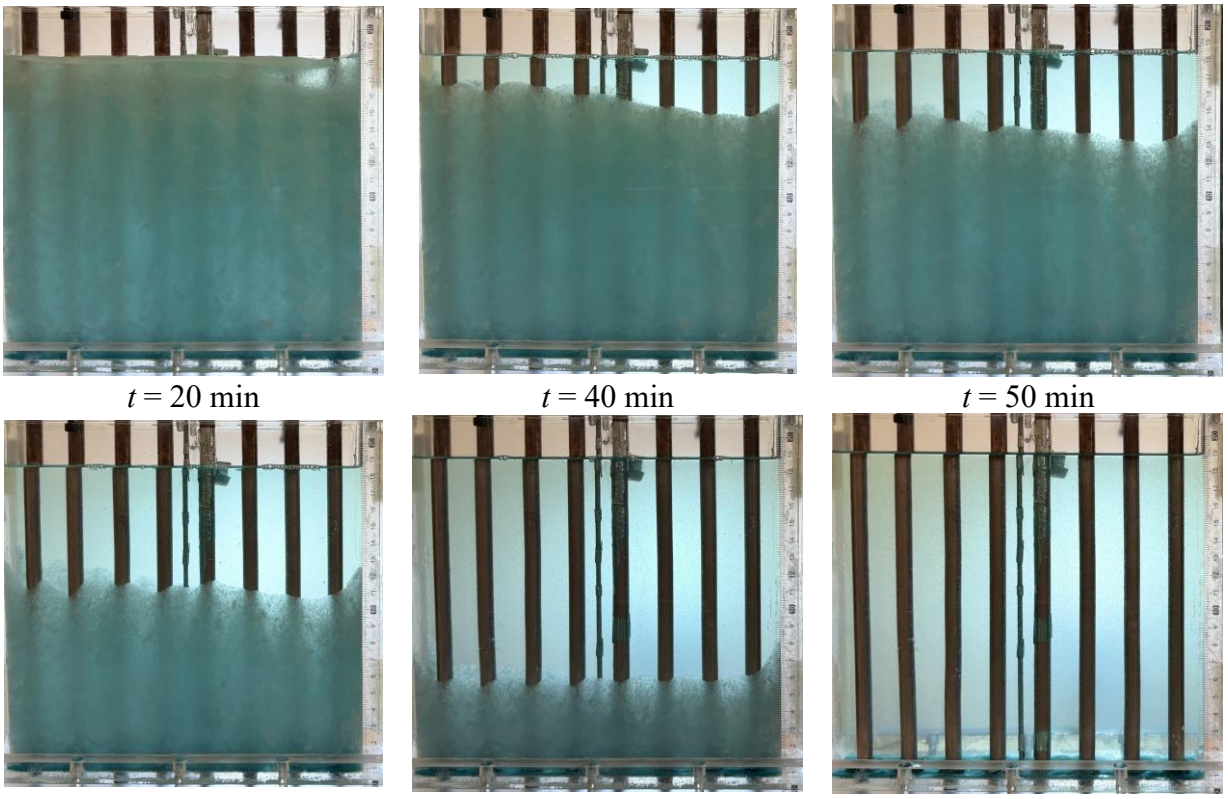

t = 20 min t = 40 min t = 50 min

t = 60 min t = 80 min t = 111 min

Figure 5-3 Temporal evolution of melting (discharging) for $T_{\text{HTF, in}}$ = 55 °C and $\dot{m}_{HTF}$ = 8.2 g/s.

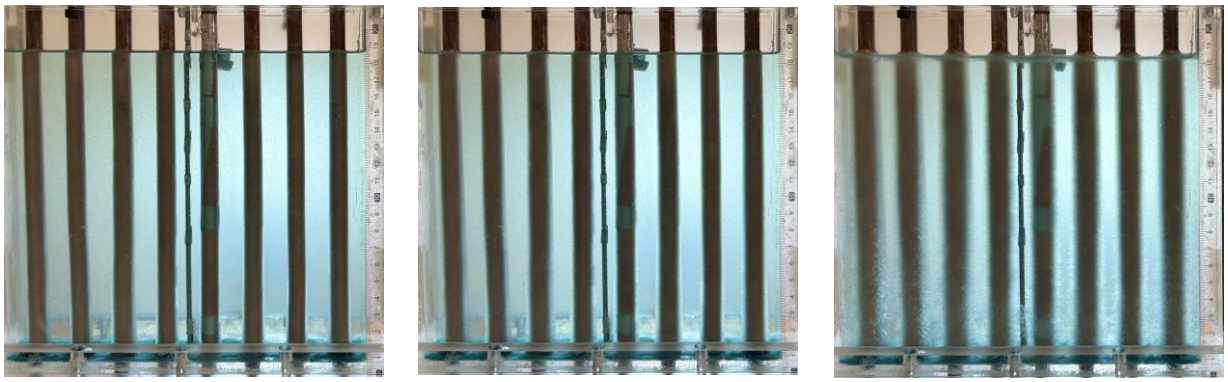

t = 15 min t = 20 min t = 30 min

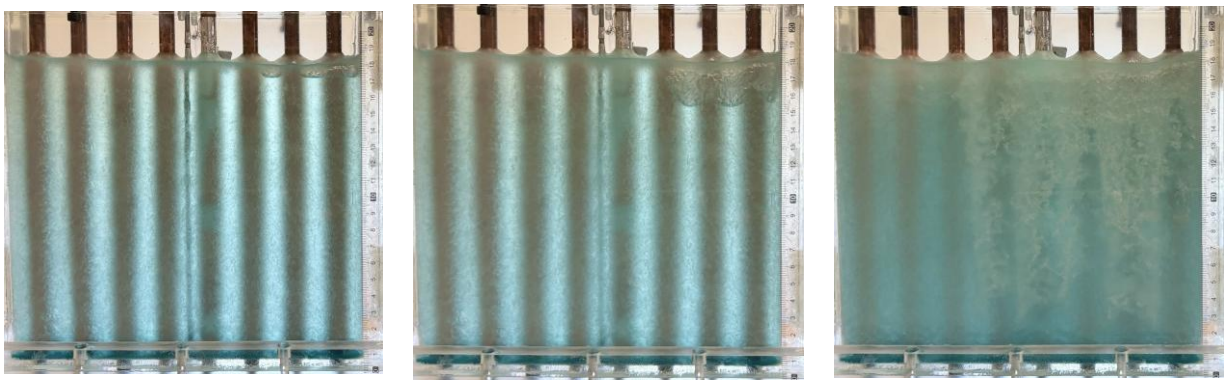

t = 40 min t = 50 min t = 238 min

Figure 5-4 Temporal evolution of melting (discharging) for $T_{\text{HTF, in}}$ = 50 ° and $\dot{m}_{HTF}$ = 8.2 g/s.

5.1.3 Results for HTF Temperature of 45 °C

Two experimental trials were performed on September 10, 2025, September 24, and October 1, 2025, using an inlet HTF temperature of $T_{\text{HTF, in}}$ = 45°C. The initial average temperature of the PCM for these trials was approximately T_{i} = 19°C. Fig.6-5 illustrates the temperature distributions at various locations within the system. The observed thermal response follows a similar trend to the cases with $T_{\text{HTF, in}}$ = 55°C and 50 °C with this exception of the melting and solidification period. In this scenario, the complete melting of the PCM occurred after roughly 155 minutes, a result of decreasing the HTF inlet temperature by 5 °C compared to the case $T_{HTF,in} = 50°C$. The sensible heat transfer from the liquid PCM to the heat pipes continued for about 24 minutes, which is shorter

than the duration observed when $T_{HTF,in} = 50°C$. As illustrated in Fig.5-5(a), the average temperatures recorded by the thermistors along the rod at the point of full melting were lower than those in the $T_{HTF, in}$ = 55°C and 50 °C cases. Consequently, the sensible heat transfer from the melted PCM was expected to persist for a shorter period.

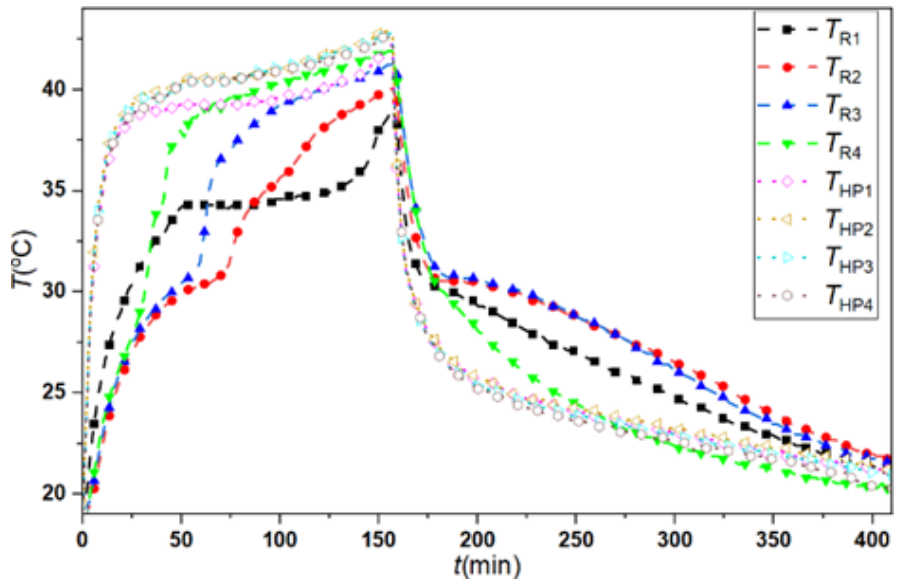

(a)

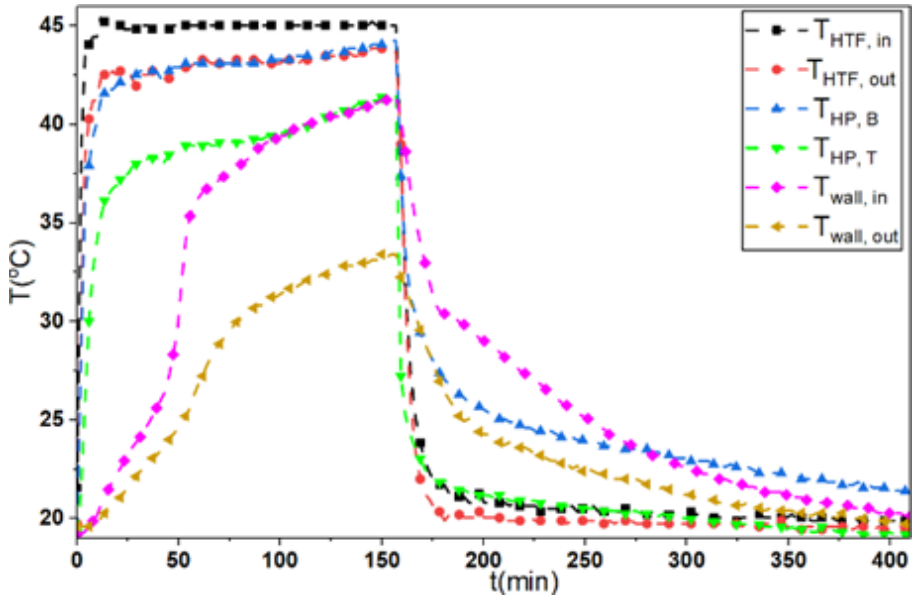

(b)

Figure 5-5 Local temperature histories for $T_{HTF,\,in}$ = 45 °C and $\dot{m}_{HTF}$ = 8.2 g/s for melting (discharging) and solidification (Charging) of a) within the storage tank thermistors and, (b) outer storage tank thermistors.

Figure 5-6 indicates same figures for the case of mass flowrate $\dot{m}_{HTF}$ = 5 g/s at different HTF temperatures of a) $T_{HTF,\,in}$ =55 °C, b) $T_{HTF,\,in}$ =50 °C, and $T_{HTF,\,in}$ =45 °C. The melting and solidification durations show dependence on the mass flow rate at the same HTF temperature. As the HTF flow rate decreases, the total melting time increases noticeably due to the reduced rate of convective heat transfer between the fluid and the HPs. For instance, at an inlet temperature of 45 °C, the melting time increases from about 155 min at 8.2 g/s to nearly 170 min at 5 g/s, representing roughly a 10% increase. A similar trend is observed at higher temperatures. During the solidification stage, the cooling is provided by fans operating at constant power rather than by the HTF. Consequently, the solidification time remains nearly independent of the previous HTF operating conditions, since the same air flow rate and cooling power are applied in all cases. The small differences observed in total time solidification and melting durations are mainly attributed to the slight variations in initial PCM temperature at the beginning of each charging cycle.

Although $T_{\mathrm{HTF,in}}$ is kept constant, $T_{HP,B}$ shows a gentle increase during melting. At the early stage, much of the HP's middle part is embedded in solid PCM, so the external thermal resistance is high and the HP transports less heat, the HP's internal saturation/metal temperatures are lower. As melting progresses and more of the middle part becomes wet by liquid PCM (better heat transfer), the effective middle side UA rises, the condensing rate and vapor mass flow increase, and the pipe operates at a slightly higher saturation temperature**.** This lifts the whole HP's temperature field by a few degrees showing as a slight upward trend in $T_{HP,B}$ even though the HTF temperature is constant.

Figure 5-7 and Fig. 6-8 demonstrates the melting and solidification process for the case $\dot{m}_{HTF}$ = 5 g/s at different $T_{HTF,\,in}$ =55 °C. Compared with the higher flow case of $\dot{m}_{HTF}$ = 8.2 g/s at the same $T_{HTF,\,in}$, complete melting took 8 min longer, and the full discharge-charging cycle was around 20 min longer. During melting, regions adjacent to the heat pipes liquefied first, while PCM near the side walls melted later, consistent with the stronger local heat transfer around the HPs. During the freezing period, columns of solid PCM formed around the HPs and grew radially, setting the initial geometry for the next cycle. The way that the solidification runs and finishes, it affect the format of melting especially at the primary times. In Fig. 5-3, melting began more rapidly on the right side of the tank. This early asymmetry is consistent with stronger local heat transfer at the upstream HPs and with the previous day's refreezing pattern, which left a denser solid band around the HPs. After a partial melt formed, buoyancy-driven natural convection dominated and the front flattened, so melting proceeded more uniformly along the length of the storage tank. In Fig. 5-7, the tank had been allowed to refreeze passively (no forced airflow) before the test was started. Solidification from the corners and walls made more solid PCM at the side walls (see t =15 min). This reason combined with the lower HTF flow ($\dot{m}_{HTF}$ = 5 g/s) made the melt front nearly uniform from the start of the test. These front melt shape differences are transient and, within experimental scatter, do not impact the overall melting time. Shorter time steps are shown during solidification to highlight the liquid-to-mushy transition at early times

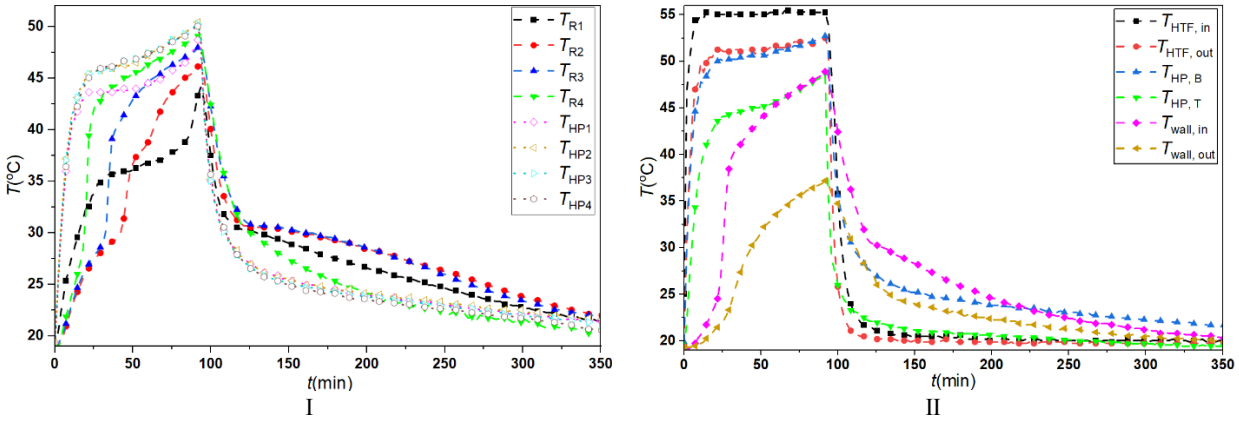

I II

(a)

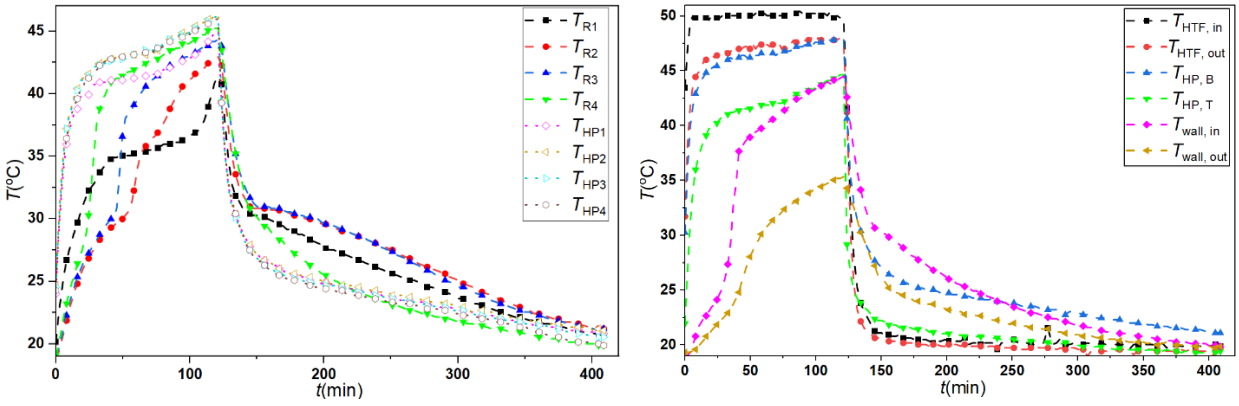

I II

(b)

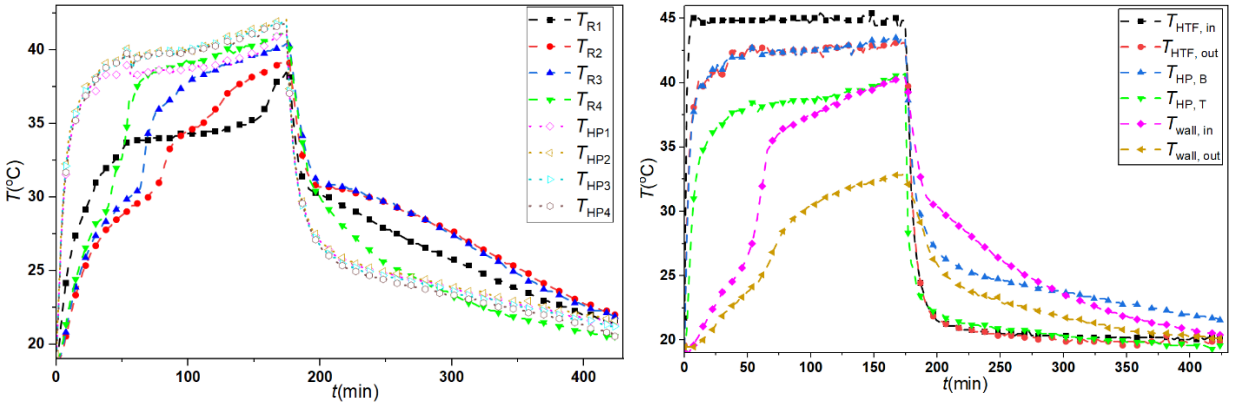

I II

(c)

Figure 5-6 Local temperature histories for a) $T_{HTF, in}$ =55 °C, b) $T_{HTF, in}$ =50 °C, and $T_{HTF, in}$ =45 °C at $\dot{m}_{HTF}$ = 5 g/s for melting (discharging) and solidification (Charging) of I) within the storage tank thermistors and, (II) outer storage tank thermistors.

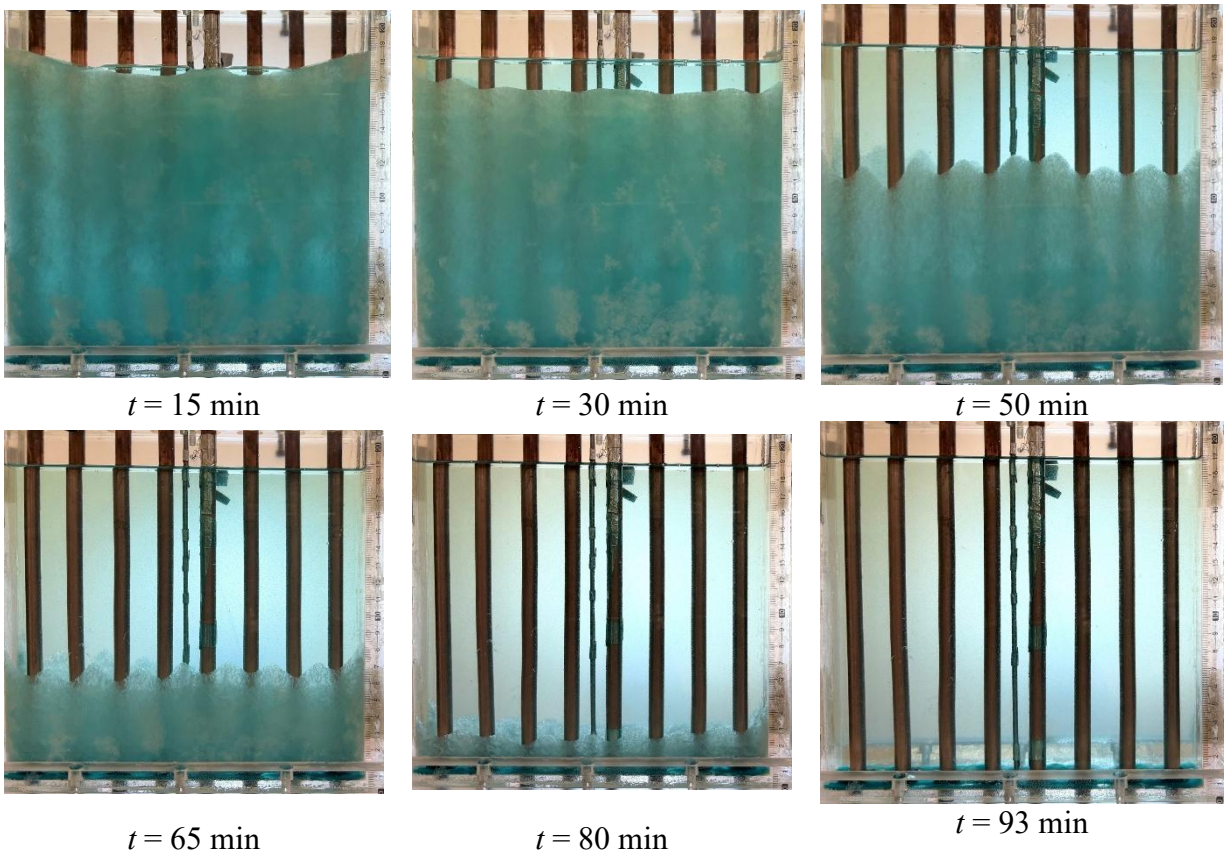

t = 15 min t = 30 min t = 50 min

t = 65 min t = 80 min t = 93 min

Figure 5-7 Temporal evolution of melting (discharging) for $T_{\mathrm{HTF,\,in}}$ =55 °C and $\dot{m}_{HTF}$ = 5 g/s.

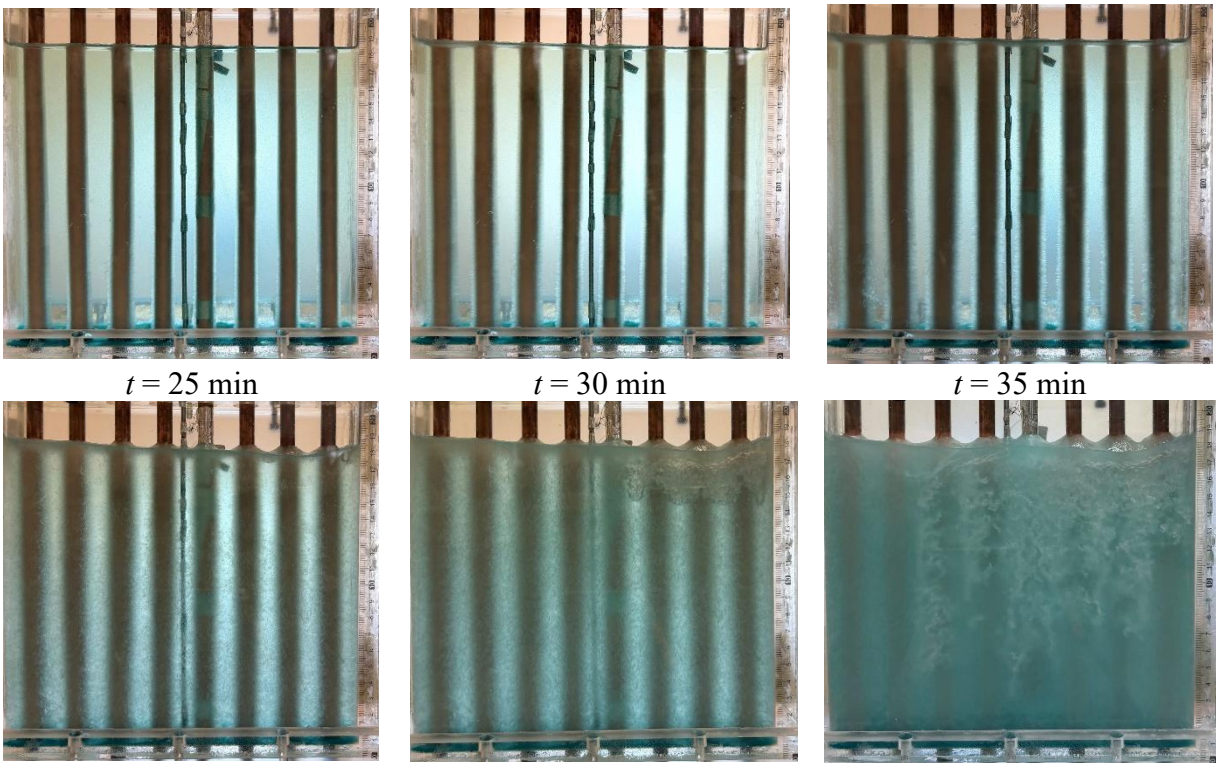

t = 25 min t = 30 min t = 35 min

t = 45 min t = 70 min t = 240 min

Figure 5-8 Temporal evolution of solidification (charging) process following complete melting, with $T_{\text{HTF, in}}$ =55 °C and $\dot{m}_{HTF}$ = 5 g/s.

5.2 Numerical Results

Numerical simulations were performed to complement the experimental findings and provide a more comprehensive understanding of the underlying heat transfer mechanisms. The convective heat transfer coefficients in the air-cooled section of the HPs were determined computationally using the domain depicted in Fig. 5-2 (a) (air speed ≈ 29 m/s). The distance from the inlet to the HPs was shorter than the length required for the boundary layer to transition into a turbulent regime, ensuring that the airflow over the fin jackets remained laminar. Additionally, the Richardson number was calculated to be approximately 0.00003 at the air speed, indicating that the flow was sufficiently fast to suppress the effects of natural convection at the given velocity.

A constant surface temperature of 50°C (from measurement) was imposed on the internal surfaces of the fin jackets within the airflow channel. Once steady-state conditions were established, the average heat flux and temperature distributions across fin jackets were evaluated. The heat flux was then divided by the temperature difference between the exposed fin jackets surfaces and the average air temperature of (T_{air} = 19.5°C) within the air channel nearby the jackets to compute the average convective heat transfer coefficient, which was found to be 136.7 W/m²·K.

Similarly, the average heat transfer coefficient for water-HP interactions within the water conduit, considering laminar flow (Fig. 5-2(b)), was computed as 1047 W/m²·K for the HTF mass flow rate of 8.2 g/s and 841.5 W/m²·K for 5 g/s. This was achieved by imposing a constant temperature of 22°C (setup initial temperature) at the outer surface of the HPs in the water conduit while maintaining the inlet water temperature at 50°C. The initial temperature of the computational

domain was set based on the ambient temperature recorded on the respective experimental data, about 19°C. Temperature contours corresponding to the computational domains shown in A1 and A2 are provided in Appendix A. It is important to note that the average convective heat transfer coefficients are assumed to remain constant and unaffected by variations in water and ambient air temperatures.

Figure 5-9(a) illustrates the temperature distribution over the surfaces of the fin jackets, as obtained from the numerical simulations of the computational domain presented in Figure 4-9(a). This temperature field was used to evaluate the convection heat transfer coefficient associated with the heat exchange between the fin jackets and the flowing air.

Similarly, Fig. 5-9(b) displays the temperature distribution across the HPs located within the water conduit, based on the numerical simulations of the computational domain depicted in Figure 4-9(b). This temperature field was employed to evaluate the convective heat transfer coefficient governing the heat exchange between the HP surfaces and the circulating water within the conduit.

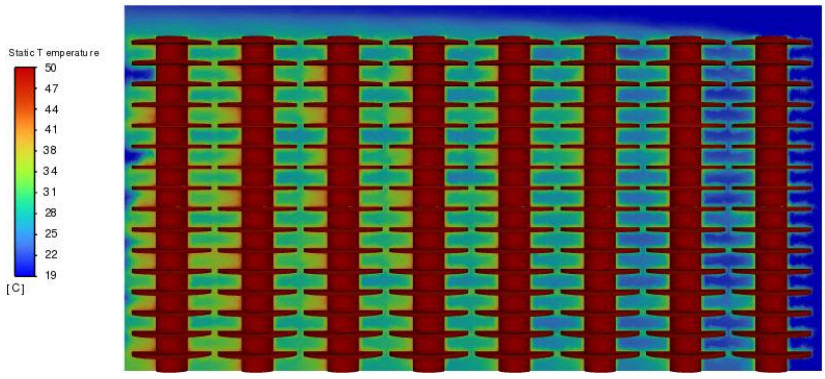

(a)

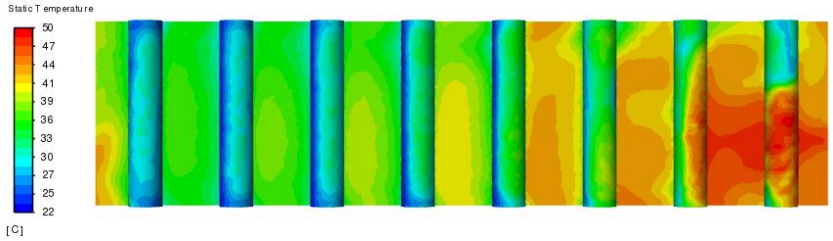

(b)

Figure 5-9 Temperature contours of a) HPs and fin jackets on the mid-plane (x–z) within the air-cooling section, and b) HPs within HTF conduit section (Air/water flow direction is from right to left.)

The following Fluent settings outlined in Table 6-1 were employed in the integrated HP–fin–PCM model:

Table 5-1 Settings used in the integrated HP–fin–PCM model implemented in ANSYS Fluent

Velocity-pressure coupling algorithm	SIMPLE
Gradient spatial discretization scheme	Least squares cell based
Pressure spatial discretization scheme	PRESTO
Density spatial discretization scheme	QUICK
Momentum spatial discretization scheme	QUICK
Energy spatial discretization scheme	QUICK
Transient formulation	First order implicit
Mesh size (Number of control volumes)	315000 (resulting in a liquid fraction change of no more than 2% at any given instant during the simulation)
Under relaxation factors	Pressure: 0.2 Density: 1 Momentum: 0.3 Liquid fraction: 0.9 Energy: 1
Residuals	Continuity: 10^{-5} velocity: 10^{-5} Energy: 10^{-6}
Mushy zone constant	5×10^{5}
Time step size	0.5s (200 iterations per time step, results in a stepwise dependence in the liquid fraction history)

Figure 5-10 illustrates the numerically predicted evolution of the liquid fraction (VF_l) of the PCM during both the discharging (melting) and charging (solidification) phases for inlet heat

transfer fluid (HTF) temperatures of 55°C, 50°C, and 45°C at a) $\dot{m}_{HTF}$ = 8.2 g/s and b) $\dot{m}_{HTF}$ = 5 g/s. The initial temperature of the computational domain was same as the experiments around 19°C, representing the ambient conditions.

For $T_{\text{HTF, in}}$ = 55°C at $\dot{m}_{HTF}$ = 8.2 g/s, the melting process is completed after approximately 85 minutes, followed by an additional 15-minutes interval before the onset of solidification at around 100 minutes. The solidification phase lasts for about 240 minutes. After about 270 minutes of solidification, less than 10% of the PCM remains. Overall, the total duration of the phase transition in this case is approximately 326 minutes.

For the case with $T_{\text{HTF,in}}$ = 50°C at $\dot{m}_{HTF}$ = 8.2 g/s, the melting process is completed within approximately 106 minutes, followed by an additional 11-minute interval before the onset of solidification at t = 117 min. Before this period and after the completion of the melting process, sensible heat is extracted from the melted PCM until it reaches the mushy-zone state, where latent heat extraction begins. The solidification process extends for approximately 235 minutes. As expected, the melting duration is shorter than the solidification period, primarily due to the enhanced thermal transport during melting, driven by buoyancy-induced natural convection in the liquid PCM. In contrast, natural convection is significantly suppressed during solidification, resulting in slower heat transfer rates. After t = 300 min, residual liquid PCM remains only corners and edges, contributing negligibly to the phase change process. The total phase transition time for this case is approximately 340 minutes.

For $T_{\text{HTF,in}}$ = 45°C at $\dot{m}_{HTF}$ = 8.2 g/s, the complete melting phase lasted around 145 minutes. Solidification initiated approximately 8 minutes after the conclusion of the melting phase, with about 90% of the PCM solidifying within around 200 minutes of the solidification.

The remaining 10% solidified more gradually over the next 50 minutes, resulting in a total phase change duration of approximately 377 minutes.

Regarding the case of $\dot{m}_{HTF}$ = 5 g/s, the melting time of the PCM increases as the instant thermal power transferred to the heat pipes decreases and it take longer time for the melting. The same pattern also was seen in the experiments. In general, a decrease in the inlet temperature of the HTF leads to an increase in the total duration required for both the melting and solidification processes.

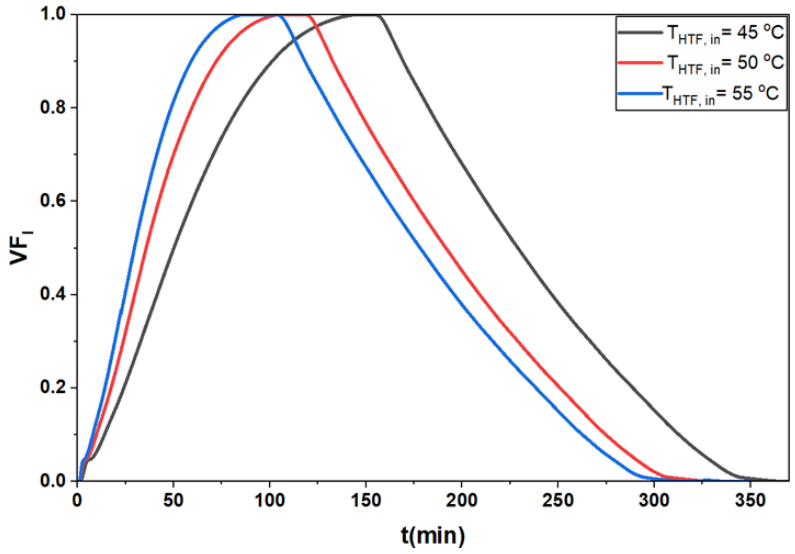

(a)

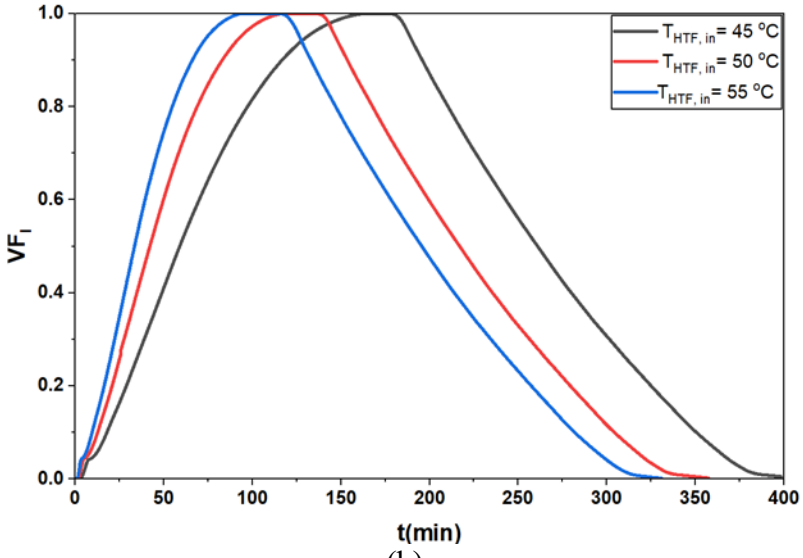

(b)

Figure 5-10 Computationally determined time variations of the melt fraction for a) $\dot{m}_{HTF}$ = 8.2 g/s and b) $\dot{m}_{HTF}$ = 5 g/s.

As a representative case, the evolution of the PCM liquid fraction during both the melting and solidification phases is presented and discussed for the condition with $T_{HTF,\,in}$ = 50°C only.

Fig. 5-11 depicts the PCM liquid fraction on the wall of the PCM chamber corresponding to the pictures of the real tests during the melting process. It is obvious that melting is more intense in the center of the chamber closer to HPs but to have a comparison with experiments the melt pictures on the wall of the storage tank are shown. The HPs are also included in the visualization to enhance clarity regarding the evolution of the PCM liquid-solid interface, particularly in regions adjacent to the HPs.

Melting initiates at approximately t = 10 min in the regions surrounding the HPs, where elevated temperatures result from direct thermal interaction with the hot water inside the water conduit. As the process progresses, buoyancy-driven convection within the molten PCM facilitates the upward movement of the liquid phase, leading to an accelerated melting rate in the upper section of the storage tank. The liquid-solid interface progresses radially from each HP centerline while simultaneously advancing from the top to the bottom of the storage tank. This behavior is consistent with the physics observed in the experimental photographs presented in Fig. 5-4.

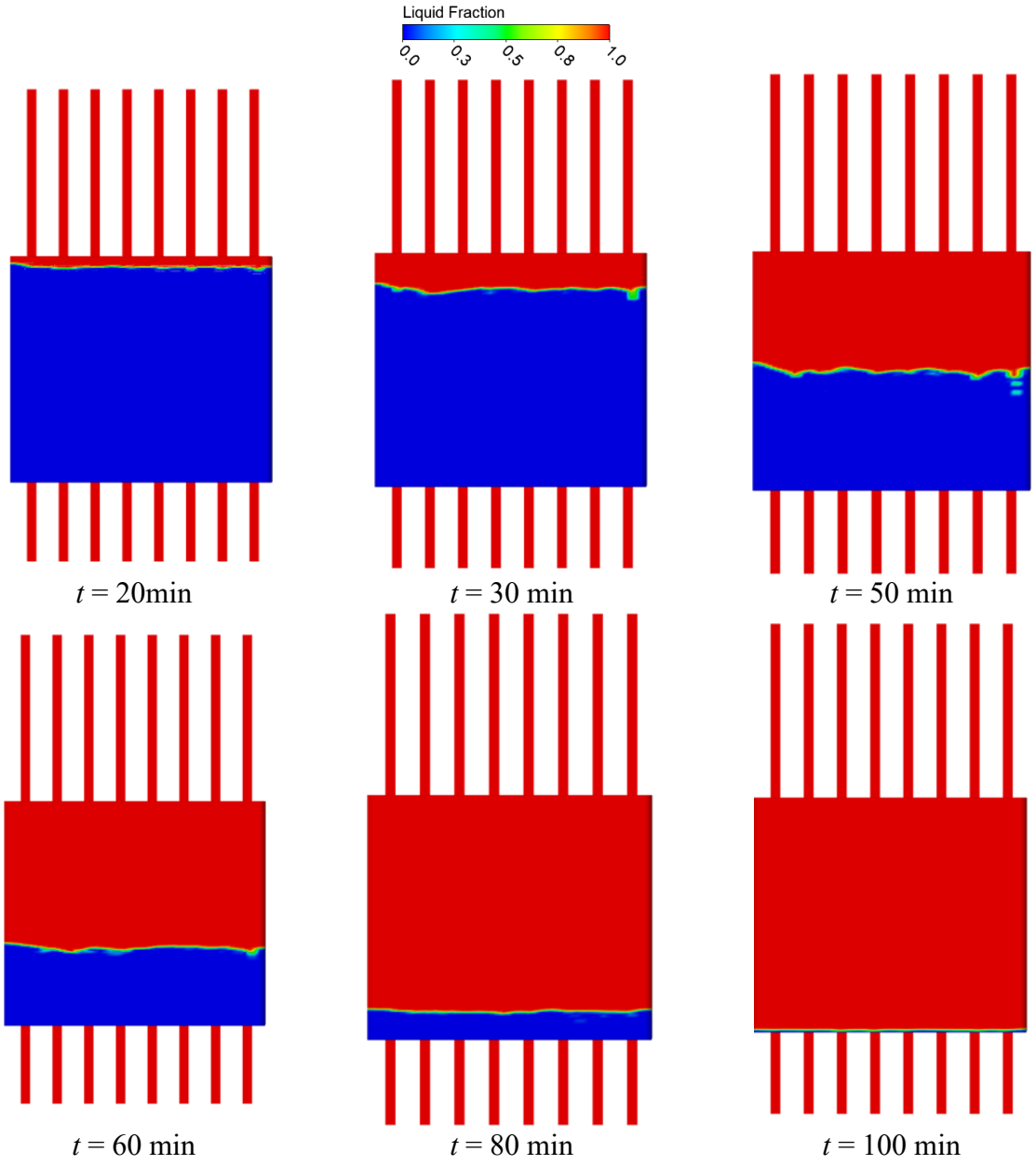

Figure 5-11 Computationally predicted temporal evolution of melting (discharging) for $T_{\mathrm{HTF,\,in}}$ = 50 °C and $\dot{m}_{HTF}$ = 8.2 g/s.

Figure 5-12 illustrates the solidification process. Having better comparison to experiments, the solidification on the symmetry wall within the middle of the storage along x-z axis is shown.

It is clear that the solidification on the walls and edges takes longer time. Solidification initiates in the regions surrounding the HPs, as these components exhibit the lowest temperatures within the storage tank, falling below the PCM's melting point. Unlike the melting process, where natural convection significantly influences phase transition dynamics, the solid-liquid interface during solidification progresses predominantly in a radial manner from each HP centerline. This behavior confirms that natural convection has a considerably weaker effect during solidification compared to the melting process, which aligns with the physics illustrated in Fig. 6-4.

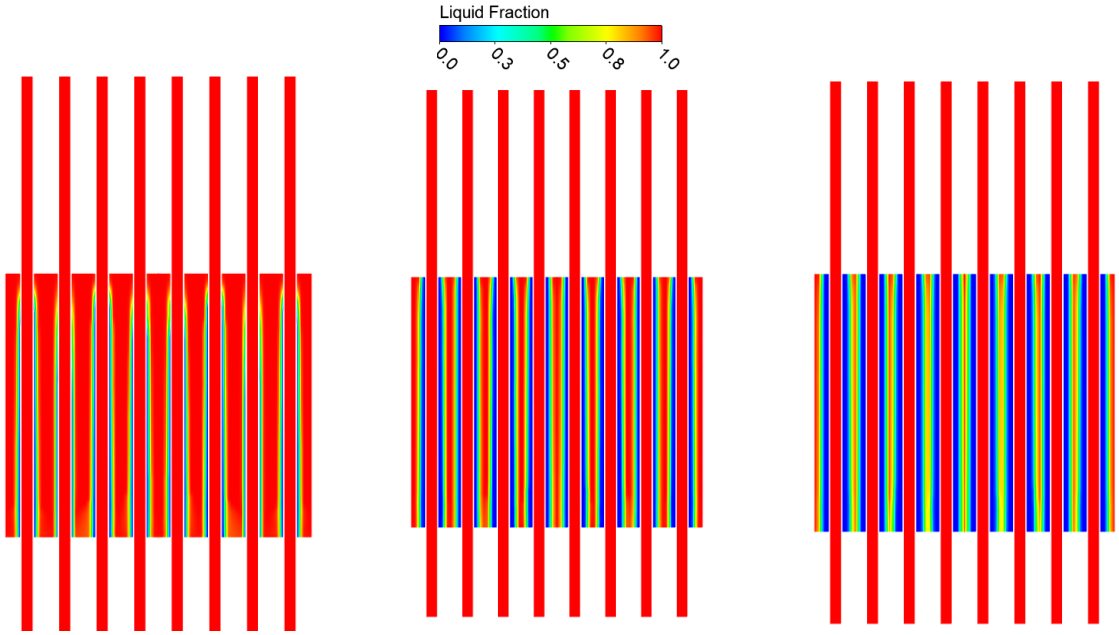

t = 140min t = 160 min t = 180 min

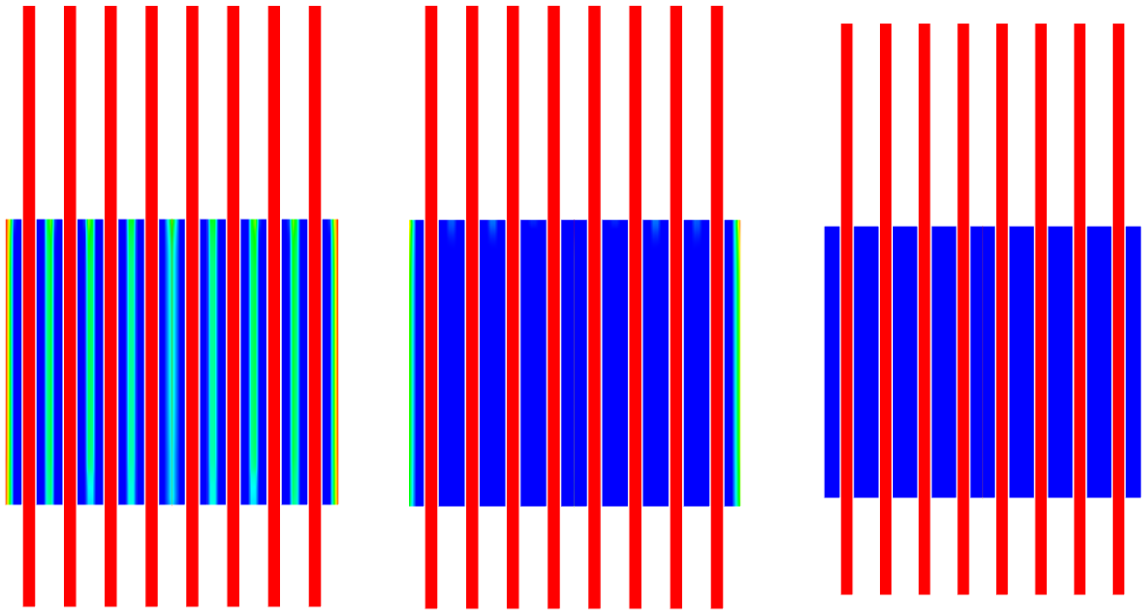

Figure 5-12 Computationally predicted temporal evolution of the solidification (charging) process following complete melting, with $T_{\text{HTF, in}}$ =50 °C and $\dot{m}_{HTF}$ = 8.2 g/s.

For improved clarity and to facilitate comparison between numerical predictions and experimental observations of the liquid–solid interface, the PCM phase interfaces for the case of $T_{\text{HTF, in}}$ = 55°C and $\dot{m}_{HTF}$ = 8.2 g/s at representative time instances $t_1 \approx 45$ min (during melting) and $t_2 \approx 135$ min (during solidification) are presented in Fig. 5-13. Overall, the comparisons demonstrate reasonable agreement, with discrepancies primarily attributed to the modeling assumptions employed in the numerical simulations.

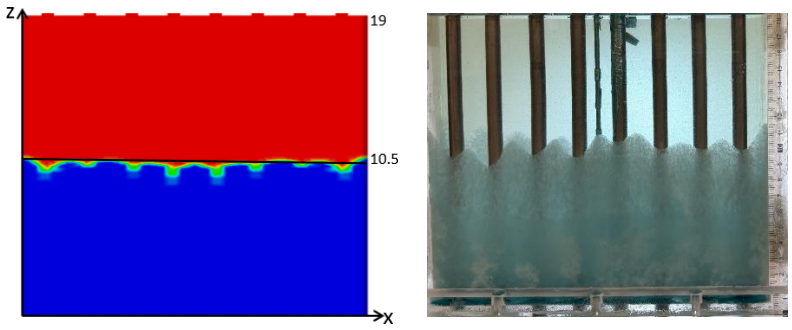

(a)

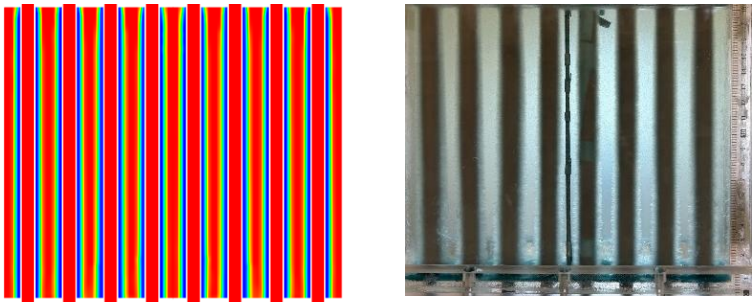

(b)

Figure 5-13 Comparison of the liquid–solid interface for $T_{\mathrm{HTF,\,in}}$ = 55°C and $\dot{m}_{HTF}$ = 8.2 g/s: (a) Melting at $t_1 \approx$ 45 min, (b) Solidification at $t_2 \approx$ 135 min. (Water and air flow directions are from right to left.)

Figure 5-14 illustrates the heat flux at the PCM (solid lines) along with the volume averaged PCM temperature (dashed lines) for a full cycle of discharging-charging at $T_{\mathrm{HTF,in}} = 45, 50,$ and 55°C. During discharge (melting), the flux is positive and peaks early, when HPs face the cold PCM and the temperature difference, ΔT, is largest; the 55 °C case shows the highest initial peak and the 45 °C has the lowest, consistent with the HTF temperature. As melting progresses and a liquid layer of PCM forms, natural convection spreads heat and the driving ΔT falls, so the flux decreases while the dashed temperature increases. When the cycle switches to charging (solidification), the flux changes sign (negative), reaching a minimum at the start of freezing and becomes smoother as the solid front grows and the thermal resistance increases. The average PCM temperature drops accordingly and crosses the PCM heat flux range once freezing is largely

complete. Overall, greater HTF inlet temperature yields a larger early heat flux peak and a faster melt, while the solidification part shows a gradual return to equilibrium for all three cases as the charging process has been same for all the cases.

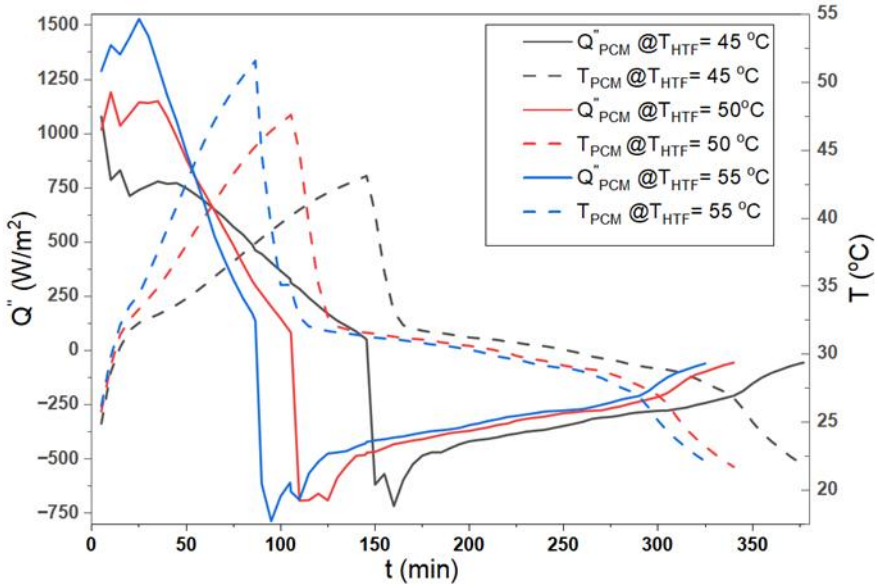

Figure 5-14 Heat flux to/from the PCM and average PCM temperature during discharge and charging cycle for different $T_{\mathrm{HTF,\,in}}$ and $\dot{m}_{HTF}$ = 8.2 g/s.

Figure 5-15 shows the melt fraction and x-velocity vectors on an x–y plane taken near the top of the PCM storage tank at (I) t = 10 min and (II) t = 15min for $T_{\mathrm{HTF,\,in}}$ =50 °C and $\dot{m}_{HTF}$ = 8.2 g/s. At t=10 min, a thin liquid PCM forms around the HP's surfaces, while rest of PCM near the walls remains largely solid. The velocity vectors show lateral recirculation at the corners between adjacent HPs. Warmer liquid next to the HPs moves sideways along the top plane, whereas velocities decay rapidly at the solid–liquid interface. At t =15 min, the liquid regions around neighboring HPs thicken and begin to join, and the lateral motion becomes more organized. This is consistent with convection strengthening as the liquid layer increases. Overall, the top section transitions from conduction dominated melting to convection assisted melting, as natural convection accelerates.

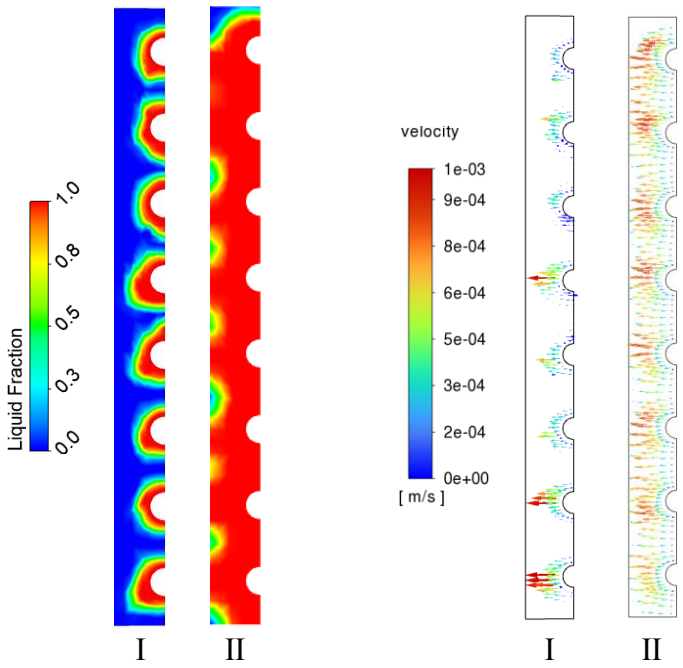

(a) (b)

Figure 5-15 (a) PCM melt fraction, and (b) x-velocity -vectors on x-y plane crossing through the top of the PCM storage at time (I) t = 10 min and (II) t = 15min, with $T_{\mathrm{HTF,\ in}}$ =50 °C and $\dot{m}_{HTF}$ = 8.2 g/s.

Figure 5-16 presents axial vapor velocity inside the HPs (evaporator at the bottom, in contact with the HTF) at different tie slots for $T_{\mathrm{HTF,\ in}}$ =50 °C and $\dot{m}_{HTF}$ = 8.2 kg/s. At the primary times the vapor velocity is highest at early times (t <30 min) and decreases as melting progresses. At the start, the middle part of the HPs are in contact with cold, mostly solid PCM, so the temperature difference ($T_{\mathrm{HP,\ B}} - T_{\mathrm{HP,\ T}}$) is large. This creates a strong saturation pressure gradient along the HP and drives a high vapor mass flux contributing to the large vapor axial velocities. As the PCM melts and the middle part warms, the temperature (and saturation pressure) difference reduces, so the driving force for vapor circulation diminishes. At the same time, more length of HP becomes wet by liquid PCM, so the required heat is in contact with a larger area, the heat flux

per unit area and the vapor flow both reduce. These two effects explain the observed decline in axial vapor velocity despite the constant evaporator temperature.

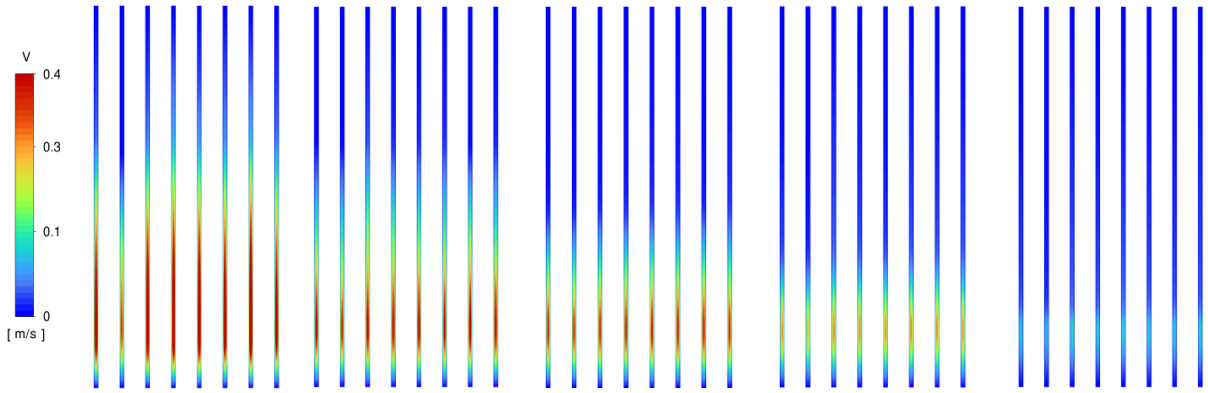

(a) (b) (c) (d) (e)

Figure 5-16 Axial vapor velocity contours within the HPs for $T_{\text{HTF, in}}$ =50 °C and $\dot{m}_{HTF}$ = 8.2 g/s at: (a) t = 10 min; (b) t = 30 min; (c) t = 45 min; (d) t = 60 min; (e) t = 90 min (the bottom end is in contact with the HTF)

Figure 5-17 compares melting (discharge) and solidification (charge) times of numerical simulations for two HTF flow rates (8.2 g/s and 5.0 g/s) at three inlet temperatures (45, 50, 55 ºC). There are two clear patterns. First, melting gets faster as the HTF is hotter and as the flow is higher, the larger ΔT and stronger convection transfer more heat through the HPs and the PCM, so the melt time reduces for both flow rates. Second, for a constant flow rate the solidification times are close and is slightly longer at higher HTF inlet temperatures. That small increase is due to a higher PCM temperature at the end of discharge, the PCM starts the freeze a bit warmer (more sensible heat to reject), and with a constant air side cooling, it takes slightly longer to refreeze. For example, at $T_{\text{HTF, in}}$= 55 ºC the volume-average PCM temperature at the end of melting is about 51.5 ºC, roughly 4.5 ºC higher than in the 50 ºC case, leading to greater time of solidification for T_{HTF} =55 ºC. At the same HTF inlet temperature, the PCM finishes the melt process about 1 ºC warmer in

the 8.2 g/s than in the 5.0 g/s case, showing the faster heat transfer at higher flow and the slightly higher bulk temperature at the end of discharge.

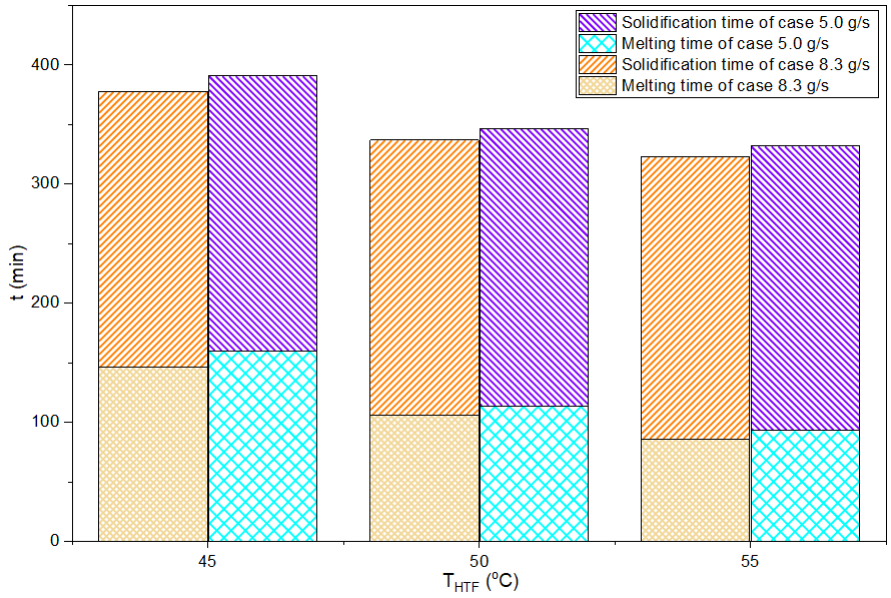

Figure 5-17 Charge/discharge times vs. HTF inlet temperature and mass flow rate.

Table 5-2 presents a comparison of the total melting and solidification durations corresponding to different $T_{\mathrm{HTF,in}}$ temperatures, as obtained from both experimental measurements and numerical simulations. The results demonstrate reasonable agreement, with observed discrepancies primarily attributed to the simplifying assumptions employed in numerical modeling.

Table 5-2 Comparison of predicted and measured melting and solidification times.

$\dot{m}_{HTF}$ (g/s)	$T_{\mathrm{HTF,in}}$ (°C)	Case	Melting (min)	Solidification+ Melting (min)
8.2	45	Experimental	155	383
		Numerical	146	377
	50	Experimental	111	348
		Numerical	106	340
	55	Experimental	86	331
		Numerical	85	326
5	45	Experimental	177	403
		Numerical	160	391

	50	Experimental	124	353
		Numerical	114	347
	55	Experimental	94	334
		Numerical	93	332

5.3 Performance of the System

This section primarily focuses on assessing the thermal performance of the proposed CTES and how well it delivers and stores cold under the two flow rates and three inlet HTF temperatures. The experimental data show reasonable agreement with numerical predictions, validating the accuracy of the simulation model. Table 5-3 summarizes the experimentally calculated heat transfer quantities, heat losses from the system and summarizes the calculated thermal resistance values during the melting process (delivers cooling) for different inlet temperatures and mass flow rates of the HTF. The governing equations, calculation procedures, and definitions were previously outlined in the Experimental Analysis section. Across both flow rates, raising the HTF inlet temperature slightly increases the energy absorbs by the PCM ($Q_{\text{lat}} + Q_{\text{sen}}$ grows from 238 to 253 kJ at 8.2 g/s, and from 237 to 252 kJ at 5.0 g/s). The overall resistance drops with both hotter inlet and higher flow. The numerical results model data R_{num} is close to R_{exp} shows confidence in the numerical calculations of the melt phase.

Table 5-4 indicates the results for stores cooling under the same fan power for all runs, so differences mainly reflect what was stored during the prior melt. As expected, the total heat rejected depends on the PCM temperature at end of melting, and higher prior inlet temperature contributes to higher PCM melt temperature (e.g., at 8.2 g/s, Q_{tot} grows from 420→443 kJ and $Q_{\text{lat}} + Q_{\text{sen}}$ from 233→250 kJ for T_{HTF} = 45→55 °C). The overall resistance in charging is higher than in discharge which is due to dependence of refreezing on the air side adding resistance. The numerical results are in good match with experimental ones for charging phase.

Table 5-3 Calculated heats and system thermal performance during the discharging process at varying HTF inlet temperatures at $\dot{m}_{HTF}$ = 8.2 g/s and $\dot{m}_{HTF}$ = 5 g/s.

$\dot{m}_{HTF}$ (g/s)	$T_{HTF,\,in}$ (°C)	ΔT (°C)	Q_{tot} (kJ)	$Q_{PCM,sen,s}$ (kJ)	$Q_{PCM,sen,l}$ (kJ)	Q_{lat} + Q_{sen} (kJ)	Q_{loss} (kJ)	R_{exp} (k/w)	R_{num} (k/w)
8.2	45	1.8	527.88	27.75	18.17	238.1	201.31	0.47	0.46
	50	2.1	451.35	26.7	25.94	244.72	201.72	0.46	0.46
	55	2.8	473.95	27.75	33.38	253.24	220.9	0.45	0.45
5	45	2.7	542.52	27.75	16.67	236.55	208.65	0.49	0.51
	50	3.1	457.8	27.75	24.61	244.46	211.74	0.48	0.49
	55	4.1	464.68	27.75	31.88	251.74	226.56	0.47	0.48

Table 5-4 Calculated heats and system thermal performance during the charging process at varying HTF inlet temperatures at $\dot{m}_{HTF}$ = 8.2 g/s and $\dot{m}_{HTF}$ = 5 g/s.

$\dot{m}_{HTF}$ (g/s)	$T_{HTF,\,in}$ (°C)	Q_{tot}(kJ)	$Q_{PCM,sen,l}$ (kJ)	$Q_{PCM,sen,s}$ (kJ)	Q_{lat} + Q_{sen} (kJ)	Q_{loss} (kJ)	R_{exp} (k/w)	R_{num} (k/w)
8.2	45	420.21	21.58	21.34	235.03	22.9	0.65	0.64
	50	429.27	29.35	21.34	242.79	26.65	0.64	0.63
	55	443.75	36.80	21.34	250.25	26.92	0.63	0.63
5	45	412.96	20.01	21.34	233.53	20.23	0.66	0.65
	50	416.59	28.03	21.34	241.47	23.71	0.64	0.64
	55	434.7	35.3	21.34	248.75	25.33	0.63	0.63

5.4 Simultaneous Charge and Discharge Operation

Up to this point, the CTES module has been tested in sequential modes; a full discharge (PCM melting) followed by a full charge (PCM solidification). In practice, however, many cooling plants operate under mixed boundary conditions, part of the system is trying to deliver cooling

while another part is already resetting the store. This section introduces and analyzes that more realistic case: simultaneous charging and discharging.

The operating idea is simple. The HPs evaporator in the hot water conduit are set to a fixed condition ($T_{HTF,\,in}$ = 50ºC), contributing to locally PCM melting, while at the same time the air side and its fan work over the condenser section that extracts heat from the PCM and promotes freezing. As a result, the PCM experiences competing thermal drives of one region gains heat through melting, another loses heat through solidifying. This configuration mimics a cooling plant that wants to keep serving heating load while gradually restoring storage, for example during a long, hot afternoon with intermittent generator operation or when recovering from a short power event.

The goals of these tests are two things. First, to monitor the operating mechanism under simultaneous drives, to identify when the net effect is "net discharge" (more melting than freezing), "net charge" (more freezing than melting), or a quasi-steady balance in which the melt fraction and outlet temperatures hold nearly constant. Second, to see the effects of hot-water setpoint and flow on the evaporator side, the air-side capacity (fan setting), and the evolving PCM geometry. In this regime, the useful criteria is the net rate.

$$Q_{net} = Q_{tot,\ discharge} - Q_{total,\ charge} - Q_{loss}$$

Considering both melt fraction and the volume average PCM temperature, when $Q_{net} > 0$, the store is still delivering cooling overall (melting dominates) and when $Q_{net} < 0$, it is recovering capacity (freezing dominates).

Tests in this section begin with a solid PCM state, apply $T_{HTF,\,in}$ = 50 ºC at the hp evaporators while running the air-cooling section at the same fan setting used in prior charging cases and other working conditions. HTF flow is held at the previous values of 8.2 or 5.0 g/s, and

all temperatures ($T_{\mathrm{HTF,in}}$, $T_{\mathrm{HTF,out}}$, PCM thermistors) are logged to compute instantaneous $Q_{tot,discharge}$, $Q_{total,charge}$, Q_{loss}, and the net Q_{net}. Images of the PCM storage show how the melt front and solid front evolve when both processes are active.

This simultaneous operation extends the useful cooling period as the store slowly recharges at the same time. In other words, instead of a switch between use the cold and reset it, operators can blend both to match real loads and ambient conditions.

Figure 6-18 presents the temperature evolution during the simultaneous melting-solidification experiment of the CTES system. In this test the HTF enters the storage tank at $T_{\mathrm{HTF,in}} = 50°\mathrm{C}$, while the incoming air to the air-cooling heat exchanger is at $T_{\mathrm{air,in}} = 19.5°\mathrm{C}$, with mass flow rates of $\dot{m}_{\mathrm{HTF}} = 8.2$ g/s and $\dot{m}_{\mathrm{air}} = 150$ g/s. The upper plot shows the local temperature histories of the thermistors inside the storage tank (T_{R1}–T_{R4} and T_{HP1}–T_{HP4}). All thermistors within the PCM (T_{R1}–T_{R4}) show a rapid increase in temperature during the first tens of minutes, followed by a much more gradual rise as the phase change progresses. The curves flatten as the PCM approaches its melting temperature and a large fraction of the supplied energy is absorbed as latent heat. The lower plot illustrates the corresponding temperatures of the working fluids, tank wall and bottom and up section of HP. The HTF inlet temperature remains close to $50°\mathrm{C}$ throughout the test, whereas the HTF outlet temperature and the temperature of the wall increase slowly, reflecting the continuous removal of heat by the air stream and the ongoing phase change within the tank.

A direct comparison with the sequential melting and solidification experiment (Fig. 5-2) helps to highlight the impact of simultaneous discharge and charge on the thermal response of the CTES unit. In the sequential case, the system is first exposed only to the hot HTF, so the PCM undergoes an alone melting process. As shown in Fig. 5-2(a) and Fig. 5-2(b), the temperatures of

the internal thermistors quickly rise toward the HTF inlet temperature, and complete melting is achieved in roughly 111 min. At the end of this melting period, the average PCM temperature is about 44°C, indicating that the PCM is not only fully melted but also significantly heated above its phase-change temperature. Once the charging phase is finished, the operating conditions are switched and the system is allowed to cool, leading to a clear transition from the high-temperature level to a gradual decay in all temperature signals as the PCM solidifies.

In contrast, when melting and solidification occur simultaneously in a single experiment, the hot HTF and the cold air stream are acting on the storage tank at the same time. Part of the energy supplied by the HTF is continuously extracted by the air loop, which effectively takes heat out of the upper region of the tank while the lower region is still being heated. As a consequence, the melting front progresses more slowly and the temperature profiles inside the tank become less steep. This is evident in Fig. 5-18(a), where none of the thermistors reaches close to the HTF inlet temperature, and curves remain in the vicinity of the melting temperature range for a much longer period. The total melting time increases from about 111 min in the alone melting test to approximately 208 min in the simultaneous melting–solidification case. In other words, concurrent discharge and charge stretch the melting process in time and lead to more moderate, smoother temperature gradients within the storage tank, which is consistent with the effects of heat input from HTF and heat removal by the air stream. Moreover, at the end of melting in the simultaneous test, the average PCM temperature is only about 38°C, noticeably lower than the 44°C observed in the sequential case. This lower final PCM temperature confirms that a significant portion of the supplied heat is continuously removed by the air stream rather than being stored as sensible heat in the PCM, leading to a more moderate temperature range of the storage material even when it is fully melted.

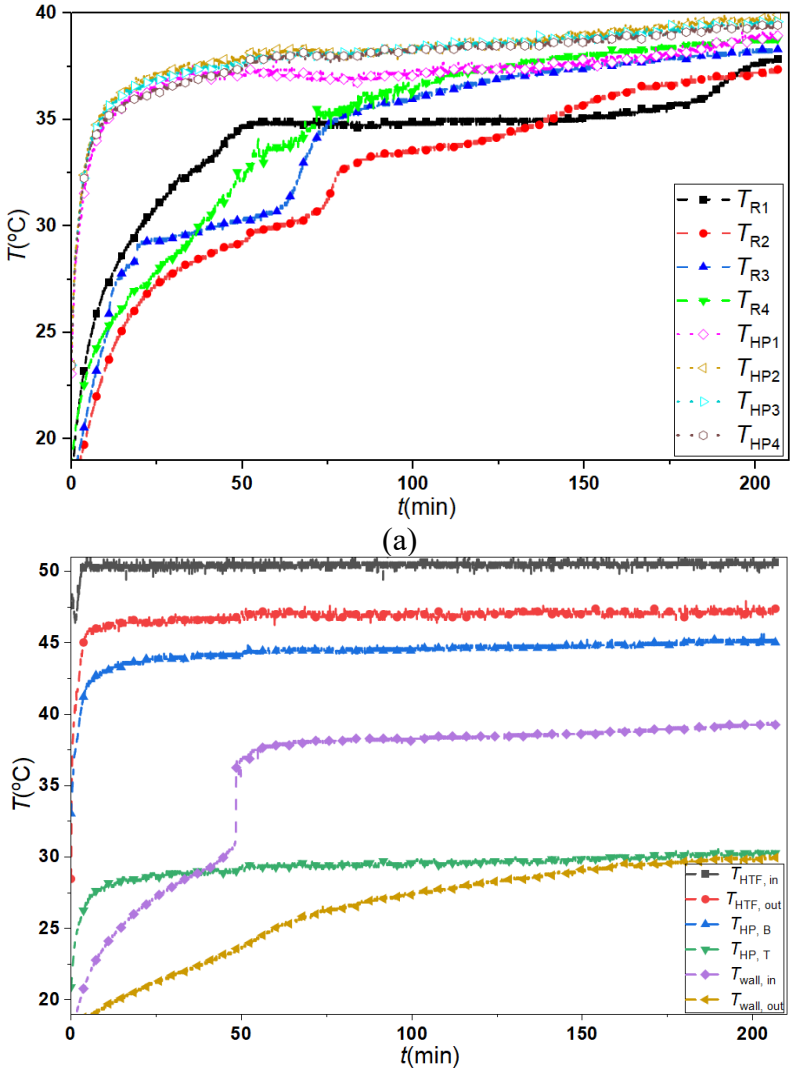

Figure 5-18 Local temperature histories for $T_{HTF, in}$ =50 °C, $T_{air,in}$ = 19°C at $\dot{m}_{HTF}$ = 8.2 g/s and $\dot{m}_{air}$ = 150 g/s for simultaneous discharging and charging of a) within the storage tank thermistors and, (b) outer storage tank thermistors.

In Fig. 5-19 melting and solidification occur simultaneously, the pictures of evolution of the PCM is clearly slower and more irregular than in the alone melting case of Fig. 5-3. In the simultaneous case, the melt front descends gradually and develops a wavy shape, with pockets of solid PCM persisting between the heat pipes even at 140–160 min and complete melting reached at about 208 min. On the other hand, in the melting-only experiment (Fig. 5-3), the front remains comparatively

flat and uniform as it moves downward, and the solid phase disappears much earlier, with full melting achieved around 111 min. The case by case comparison highlights the effect of the concurrent cooling by the air stream, which continuously removes part of the supplied heat and therefore stretches the melting process and enhances spatial non-uniformity of the melt front.

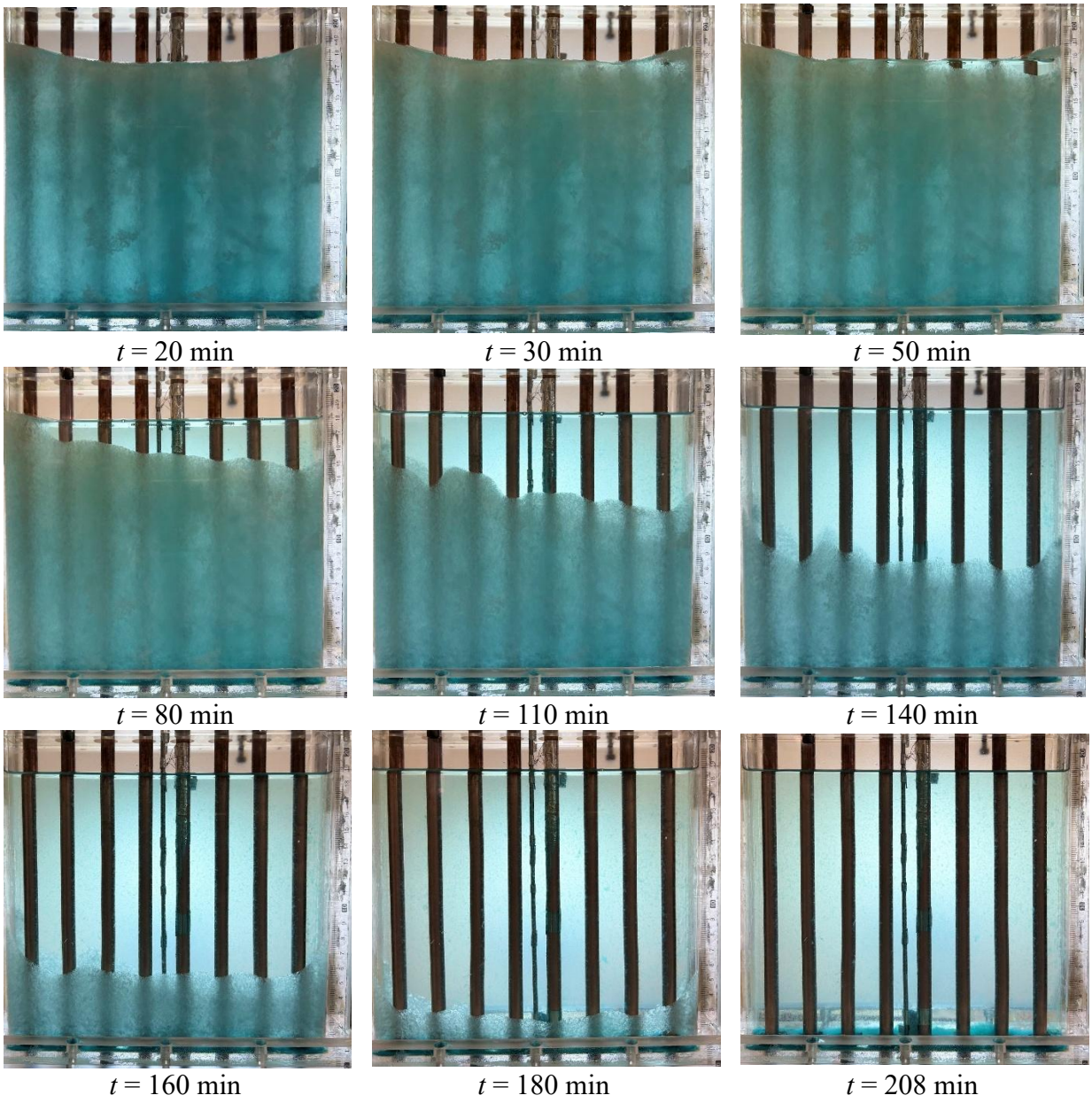

Figure 5-19 Temporal evolution of simultaneous discharging and charging $T_{HTF,\,in}$ =50 °C, $T_{air,\,in}$ = 19.5°C at $\dot{m}_{HTF}$ = 8.2 g/s and $\dot{m}_{air}$ = 150 g/s.

Figure 5-20 shows the temperature histories when the air mass flow rate is reduced by half, to $\dot{m}_{air} = 75$ g/s, while $T_{HTF,in} = 50°C$, $T_{air,in} = 19.5°C$, and $\dot{m}_{HTF} = 8.2$ g/s remain approximately unchanged. The only difference was on the slight change in the ambient temperature that the day of this was a little higher. With the weaker air flow, the heat extracted from the tank is smaller, so the PCM warms up more quickly and the melting front progresses faster than in the previous simultaneous case with $\dot{m}_{air} = 150$ g/s. As a result, the total melting time decrease to about 168 min, which is still longer than the alone melting test but noticeably shorter than the 208 min observed with the higher air flow rate. At the end of melting, the average PCM temperature is approximately 39°C, slightly higher than the previous simultaneous (38°C) case, reflecting the reduced cooling effect of the air loop and the increased fraction of heat stored as sensible energy in the PCM.

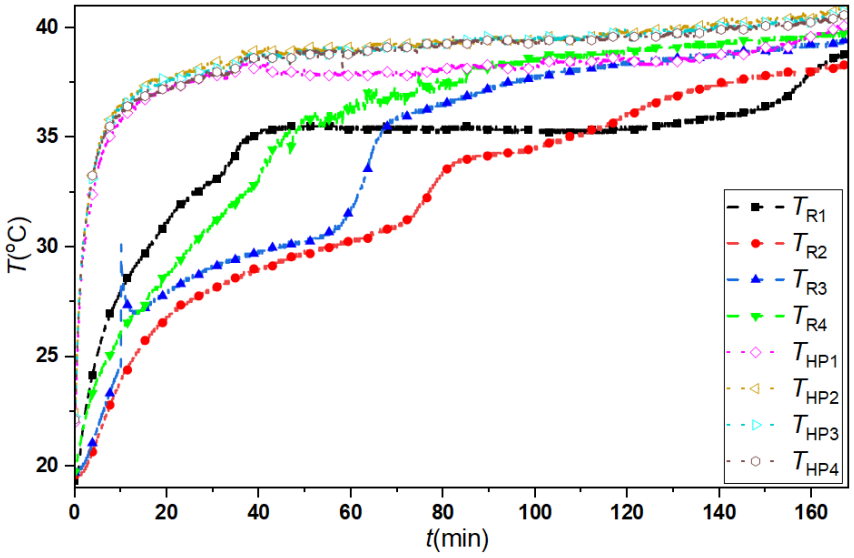

(a)

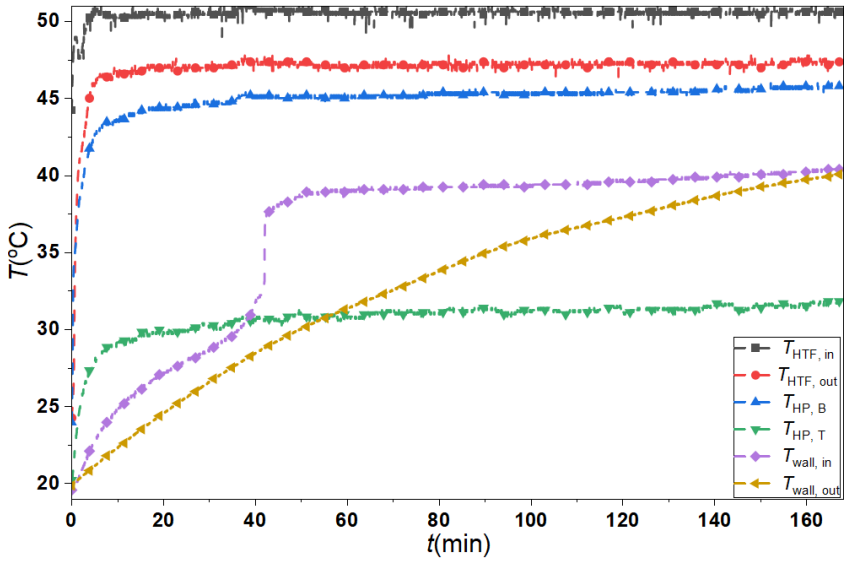

(b)

Figure 5-20 Local temperature histories for $T_{HTF, in}$=50 °C, $T_{air,in}$ = 19.5°C at $\dot{m}_{HTF}$ = 8.2 g/s and $\dot{m}_{air}$ = 75 g/s for simultaneous discharging and charging of a) within the storage tank thermistors and, (b) outer storage tank thermistors.

Table 5-5 summarizes the calculated heats and overall thermal performance of the CTES system for the two simultaneous discharging/charging tests. In both cases the HTF conditions are the same ($\dot{m}_{HTF}$ = 8.2 g/s, $T_{HTF, in}$=50 °C) while the air mass flow rate is either 150 g/s or 75 g/s. When the higher air flow is used, the total heat discharged from the tank is about 1476 kJ, compared with 1189 kJ for the lower air flow, and the corresponding charging heat also almost doubles (about 832 kJ versus 432 kJ). This reflects the stronger convective cooling and heating provided by the larger air flow rate. Also, the useful thermal energy stored in the PCM, represented by $Q_{sens} + Q_{lat}$, remains almost the same in both simultaneous cases, about 234–236 kJ. These values are also close to those obtained for the sequential melting/solidification experiments, indicating that the main storage capacity of the PCM block is essentially independent of whether the system is operated sequentially or at simultaneous charge and discharge conditions. However, in the simultaneous case this similar amount of cooling energy is spread over a longer period of time, so the PCM can

provide useful cooling for a longer duration, which is more beneficial for applications that require extended operating times or load shifting. The heat losses Q_{loss} are likewise of similar magnitude (around 220–230 kJ), showing that changing the air flow rate mostly affects how fast and where heat is transferred between the tank and the air, rather than how much total energy the PCM can store and later give back.

Table 5-5 Calculated heats and system thermal performance during the simultaneous discharging and charging process at varying mass flow rates and temperatures

$\dot{m}_{\text{HTF}}$ (g/s)	$T_{\text{HTF, in}}$ (°C)	$\dot{m}_{air}$ (g/s)	T_{air} (°C)	$Q_{tot,Discharge}$ (kJ)	$Q_{tot,Charge}$ (kJ)	$Q_{sens} + Q_{lat}$ (kJ)	Q_{loss} (kJ)
8.2	50	150	19	1475.5	831.6	233.9	216.8
8.2	50	75	19.5	1189.2	432.2	236	229.5

Chapter 6. Concluding Remarks and Future Work

Experimental and numerical investigations were conducted to design and evaluate a CTES capable of storing thermal energy during nighttime and discharging it during daytime, with a specific focus on applications involving industrial hot waste recovery and residential HVAC cooling. The CTES system integrates PCM, HPs, and extended surfaces (fins) to enhance thermal performance. Three different HTF inlet temperatures of 55 °C, 50°C, and 45°C were analyzed for both the charging and discharging scenarios, each with two different HTF mass flow rates of and $\dot{m}_{HTF}$ = 8.2 g/s and $\dot{m}_{HTF}$ = 5 g/s.

6.1 Concluding Remarks

Concluding Remarks are summarized as follows:

- Melting Time Sensitivity: The total melting time at $T_{\text{HTF, in}}$ = 55°C is approximately 45% shorter than that at $T_{\text{HTF, in}}$ = 45°C, highlighting the significant influence of HTF temperature on the discharge performance.
- PCM Solidification Dynamics: During the charging phase, more than 90% of the PCM solidifies within the initial 75% of the time, with residual solidification occurring near the periphery (edges and corners) in the final phase.
- Heat Transfer Mechanisms: Natural convection significantly enhances the discharging (melting) process once the system transitions from conduction-dominated to convection-dominated heat transfer, unlike the charging phase which remains largely conduction-driven.
- The hotter HTF and higher flow rate shorten the full charge/discharge cycle, making this CTES design a practical, fast turnaround option for industrial cooling.

- Model Validation: The numerical simulations closely match experimental data, showing a discrepancy in overall system performance of 5%.
- Simultaneous discharge-charge keeps the $T_{HTF,\,out}$ lower than sequential case and extends the delivery window. Compared with the sequential case, the melt time increases from 111 min to 208 min when the air flow was 150 g/s, and the PCM finishes the melting at 38 °C vs. 44 °C for sequential case, consistent with continuous heat removal by the air loop during discharge.
- The useful PCM energy ($Q_{sen} + Q_{lat}$) stays nearly the same in simultaneous run and the sequential tests. Simultaneous charge–discharge therefore does not increase capacity. It spread the same "cold" over a longer period while gradually rebuilt storage. This operating mode supports longer, steadier delivery and aligns with applications that need extended coverage or time-shifted cooling

6.2 Future Works

In this dissertation, a CTES setup is fabricated and evaluated under a variety of operational conditions. The experimental study demonstrated promising results, showing the efficacy and feasibility of a novel CTES system. Despite the advantages of the proposed system, several aspects of the current configuration require further modifications or enhancements to optimize performance. Future improvements should focus on refining these areas to fully leverage the potential of this innovative storage approach.

- One modification that could be implemented in the current study involves assessing the influence of mass of the PCM, flowrate of the HTF, configuration of the HPs in the PCM chamber/water conduit on system performance and long-term operational reliability.

- Using hourly ambient temperature data for a city like Norman, simulate a full day schedule for the CTES under sequential and simultaneous charge–discharge modes to identify the best operating windows considering optimize hot water setpoint, HTF mass flow, and fan speed to maximize useful cold delivered, minimize cycle losses, and quantify expected cooling continuity during brief outages.
- As an optimized method, there could be a parametric study on the evaporator and condenser lengths (holding total tube length and charge constant). For example, increase the evaporator immersion in the HTF manifold from 5 cm to 7 cm and reduce the condenser length exposed to the air-cooling section from 10.5 cm to 8.5 cm. Quantify the impact on discharge power, charge/freezing time. This will show how the length split governs system performance at the tested flows and temperatures.
- It is recommended to explore the use of thermosyphons in place of HPs in large-scale industrial systems, particularly in environments where the ambient temperature exceeds the heat source temperature and PCM melting point. This would restore the fully passive operation originally envisioned for the system, eliminating the need for an active fan. While the HPs with a fan system effectively ensure functionality, they introduce mechanical components that compromise the passive nature of the design. The decision to use HPs was driven by the unavailability of suitable thermosyphons in the market at the time of this research. For areas like arid regions or locations with fluctuating temperatures, thermosyphons could provide an efficient, passive heat transfer mechanism, improving system sustainability and reducing maintenance needs without the added complexity of mechanical components.

- However, the thickness of the acrylic material was chosen in a way to minimize the losses through the system a recommendation is to fully insulate the setup including the PCM tank, air-cooling section, pipes, and supports. This will cut stray heat losses, keep temperatures steadier, and make the energy balance much tighter.

Nomenclature

Symbol	Description	Unit / Note
A_{mushy}	Mushy-zone constant	
c_p, C_p	Specific heat	J/kg·K or J/kg·°C
g	Gravitational acceleration	m/s²
h, H	Enthalpy	J/kg
h_{fg}	latent heat of vaporization of the HP working fluid	kJ/kg
h_{sl}	Latent heat of fusion of the PCM	kJ/kg
HP	Heat pipe	
ID	Inner diameter	cm or mm
k	Thermal conductivity	W/m·K
L	Length	cm or mm
$\dot{m}$	Mass flux	kg/m²·s
OD	Outer diameter	m or mm
p	Pressure	Pa
PCM	Phase change material	
Q	Heat transfer	J
Q''	Heat flux	W/m² or kW/m²

R_g	Gas constant	J/kg·K
S_b	Source term	
t	Time	s or min
T	Temperature	K or °C
T_{air}	Air temperature	K or °C
u	Velocity vector	m/s
VF	Volume fraction	
x, y, z	Coordinates	m or mm
Greek		
ΔT	Temperature range	K or °C
α	Liquid fraction	
β	Thermal expansion coefficient	1/K
ε	Small value	
μ	Viscosity	Pa·s
ρ	Density	kg/m³
Subscript		
ab	Adiabatic	
ac	Air cooling section	
exp	experimental	

F	Fin
int	Interface
l	Liquid
Lat	Latent heat
m	melting
num	Numerical
Ref	Reference
s	Solid
sat	Saturation
sen	Sensible heat
st	Storage tank
tot	total
v	Vapor
w	Wall
wc	Water conduit
wi	Wick

References

[1] H. Zhai and E. S. Rubin, "Performance and cost of wet and dry cooling systems for pulverized coal power plants with and without carbon capture and storage," *Energy Policy,* vol. 38, no. 10, pp. 5653-5660, 2010/10/01/ 2010, doi: https://doi.org/10.1016/j.enpol.2010.05.013.

[2] H. Zhai, E. S. Rubin, E. J. Grol, A. C. O'Connell, Z. Wu, and E. G. Lewis, "Dry cooling retrofits at existing fossil fuel-fired power plants in a water-stressed region: Tradeoffs in water savings, cost, and capacity shortfalls," (in English), *Applied Energy,* vol. 306, p. Medium: ED; Size: Article No. 117997, 2021, doi: 10.1016/j.apenergy.2021.117997.

[3] F. Kojok, F. Fardoun, R. Younes, and R. Outbib, "Hybrid cooling systems: A review and an optimized selection scheme," *Renewable and Sustainable Energy Reviews,* vol. 65, pp. 57-80, 2016/11/01/ 2016, doi: https://doi.org/10.1016/j.rser.2016.06.092.

[4] G. Zhu, T. Wen, Q. Wang, and X. Xu, "A review of dew-point evaporative cooling: Recent advances and future development," *Applied Energy,* vol. 312, p. 118785, 2022/04/15/ 2022, doi: https://doi.org/10.1016/j.apenergy.2022.118785.

[5] P. Esfanjani, S. Jahangiri, A. Heidarian, M. S. Valipour, and S. Rashidi, "A review on solar-powered cooling systems coupled with parabolic dish collector and linear Fresnel

reflector," *Environmental Science and Pollution Research,* vol. 29, no. 28, pp. 42616-42646, 2022/06/01 2022, doi: 10.1007/s11356-022-19993-3.

[6] I. Oropeza-Perez and P. A. Østergaard, "Active and passive cooling methods for dwellings: A review," *Renewable and Sustainable Energy Reviews,* vol. 82, pp. 531-544, 2018/02/01/ 2018, doi: https://doi.org/10.1016/j.rser.2017.09.059.

[7] D. Parker, "Theoretical Evaluation of the NightCool Nocturnal Radiation Cooling Concept," 01/01 2005.

[8] G. Li, "Sensible heat thermal storage energy and exergy performance evaluations," *Renewable and Sustainable Energy Reviews,* vol. 53, pp. 897-923, 2016/01/01/ 2016, doi: https://doi.org/10.1016/j.rser.2015.09.006.

[9] A. Gil *et al.*, "State of the art on high temperature thermal energy storage for power generation. Part 1—Concepts, materials and modellization," *Renewable and Sustainable Energy Reviews,* vol. 14, no. 1, pp. 31-55, 2010/01/01/ 2010, doi: https://doi.org/10.1016/j.rser.2009.07.035.

[10] G. Alva, Y. Lin, and G. Fang, "An overview of thermal energy storage systems," *Energy,* vol. 144, pp. 341-378, 2018.

[11] I. Dincer and M. A. Rosen, "Energy storage systems," *Thermal Energy Storage: Systems and Applications,* pp. 51-82, 2010.

[12] B. Zalba, J. M. Marín, L. F. Cabeza, and H. Mehling, "Review on thermal energy storage with phase change: materials, heat transfer analysis and applications," *Applied Thermal Engineering,* vol. 23, no. 3, pp. 251-283, 2003/02/01/ 2003, doi: https://doi.org/10.1016/S1359-4311(02)00192-8.

[13] F. Agyenim, N. Hewitt, P. Eames, and M. Smyth, "A review of materials, heat transfer and phase change problem formulation for latent heat thermal energy storage systems (LHTESS)," *Renewable and Sustainable Energy Reviews,* vol. 14, no. 2, pp. 615-628, 2010/02/01/ 2010, doi: https://doi.org/10.1016/j.rser.2009.10.015.

[14] M. M. Kenisarin, "High-temperature phase change materials for thermal energy storage," *Renewable and Sustainable Energy Reviews,* vol. 14, no. 3, pp. 955-970, 2010/04/01/ 2010, doi: https://doi.org/10.1016/j.rser.2009.11.011.

[15] L. Scapino, H. A. Zondag, J. Van Bael, J. Diriken, and C. C. M. Rindt, "Sorption heat storage for long-term low-temperature applications: A review on the advancements at material and prototype scale," *Applied Energy,* vol. 190, pp. 920-948, 2017/03/15/ 2017, doi: https://doi.org/10.1016/j.apenergy.2016.12.148.

[16] I. Dincer, "On thermal energy storage systems and applications in buildings," *Energy and buildings,* vol. 34, no. 4, pp. 377-388, 2002.

[17] R. Zeinelabdein, S. Omer, and G. Gan, "Critical review of latent heat storage systems for free cooling in buildings," *Renewable and Sustainable Energy Reviews,* vol. 82, pp. 2843-2868, 2018.

[18] E. Oró, A. de Gracia, A. Castell, M. M. Farid, and L. F. Cabeza, "Review on phase change materials (PCMs) for cold thermal energy storage applications," *Applied Energy,* vol. 99, pp. 513-533, 2012/11/01/ 2012, doi: https://doi.org/10.1016/j.apenergy.2012.03.058.

[19] L. F. Cabeza, F. R. Martínez, E. Borri, S. Ushak, and C. Prieto, "Thermal Energy Storage Using Phase Change Materials in High-Temperature Industrial Applications: Multi-Criteria Selection of the Adequate Material," *Materials,* vol. 17, no. 8, p. 1878, 2024. [Online]. Available: https://www.mdpi.com/1996-1944/17/8/1878.

[20] H. Wang, B. Xie, and C. Li, "Review on operation control of cold thermal energy storage in cooling systems," *Energy and Built Environment,* vol. 6, no. 3, pp. 509-523, 2025/06/01/ 2025, doi: https://doi.org/10.1016/j.enbenv.2024.01.007.

[21] K. Nwaigwe, O. Anthony, N. Ogueke, and E. Anyanwu, "Review of nocturnal cooling systems," *International Journal of Energy for a Clean Environment,* vol. 11, pp. 117-143, 01/01 2010, doi: 10.1615/InterJEnerCleanEnv.2011003225.

[22] A. P. Tsoy, A. S. Granovskiy, A. V. Baranenko, and D. A. Tsoy, "Effectiveness of a night radiative cooling system in different geographical latitudes," *AIP Conference Proceedings,* vol. 1876, no. 1, 2017, doi: 10.1063/1.4998880.

[23] K. Yanbing, J. Yi, and Z. Yinping, "Modeling and experimental study on an innovative passive cooling system—NVP system," *Energy and buildings,* vol. 35, no. 4, pp. 417-425, 2003.

[24] A. Waqas and S. Kumar, "Utilization of Latent Heat Storage Unit for Comfort Ventilation of Buildings in Hot and Dry Climates," *International Journal of Green Energy,* vol. 8, no. 1, pp. 1-24, 2011/02/11 2011, doi: 10.1080/15435075.2010.529406.

[25] A. Waqas, M. Ali, and Z. Ud Din, "Performance analysis of phase-change material storage unit for both heating and cooling of buildings," *International Journal of Sustainable Energy,* vol. 36, no. 4, pp. 379-397, 2017/04/21 2017, doi: 10.1080/14786451.2015.1018832.

[26] K. Nagano, S. Takeda, T. Mochida, K. Shimakura, and T. Nakamura, "Study of a floor supply air conditioning system using granular phase change material to augment building

mass thermal storage—heat response in small scale experiments," *Energy and buildings,* vol. 38, no. 5, pp. 436-446, 2006.

[27] K. Nagano, S. Takeda, T. Mochida, and K. Shimakura, "Thermal characteristics of a direct heat exchange system between granules with phase change material and air," *Applied Thermal Engineering,* vol. 24, no. 14-15, pp. 2131-2144, 2004.

[28] A. A. R. Darzi, S. M. Moosania, F. L. Tan, and M. Farhadi, "Numerical investigation of free-cooling system using plate type PCM storage," *International Communications in Heat and Mass Transfer,* vol. 48, pp. 155-163, 2013/11/01/ 2013, doi: https://doi.org/10.1016/j.icheatmasstransfer.2013.08.025.

[29] R. Zeinelabdein, S. Omer, and G. Gan, "Experimental performance of latent thermal energy storage for sustainable cooling of buildings in hot-arid regions," *Energy and Buildings,* vol. 186, pp. 169-185, 2019/03/01/ 2019, doi: https://doi.org/10.1016/j.enbuild.2019.01.013.

[30] Y. Hu, P. K. Heiselberg, C. Drivsholm, A. S. Søvsø, P. J. C. Vogler-Finck, and K. Kronby, "Experimental and numerical study of PCM storage integrated with HVAC system for energy flexibility," *Energy and Buildings,* vol. 255, p. 111651, 2022/01/15/ 2022, doi: https://doi.org/10.1016/j.enbuild.2021.111651.

[31] T. Reboli, M. Ferrando, A. Traverso, and J. N. W. Chiu, "Thermal energy storage based on cold phase change materials: Discharge phase assessment," *Journal of Energy Storage,* vol. 73, p. 108939, 2023/12/10/ 2023, doi: https://doi.org/10.1016/j.est.2023.108939.

[32] F. Wang *et al.*, "Advancing next-generation cold storage: A comprehensive analysis of energy efficiency and life cycle cost assessment using clathrate hydrates," *Energy,* vol. 332, p. 137233, 2025/09/30/ 2025, doi: https://doi.org/10.1016/j.energy.2025.137233.

[33] B. Lamrani, R. T. Alqahtani, A. Ajbar, and M. benaicha, "Dynamic performance analysis of sensible and latent cold thermal energy storage systems for building cooling networks," *Case Studies in Thermal Engineering,* vol. 71, p. 106264, 2025/07/01/ 2025, doi: https://doi.org/10.1016/j.csite.2025.106264.

[34] M. A. Alam, K. Irshad, S. Rehman, F. Masood, and M. E. Zayed, "Recent developments in renewable energy assisted cold thermal energy storage air conditioning systems," *Journal of Energy Storage,* vol. 127, p. 117124, 2025/08/15/ 2025, doi: https://doi.org/10.1016/j.est.2025.117124.

[35] G. Fang, F. Tang, and L. Cao, "Dynamic characteristics of cool thermal energy storage systems—A review," *International Journal of Green Energy,* vol. 13, no. 1, pp. 1-13, 2016.

[36] K. Yang, Z. Chen, and P. Zhang, "State-of-the-art of cold energy storage, release and transport using CO2 double hydrate slurry," *Applied Energy,* vol. 358, p. 122531, 2024/03/15/ 2024, doi: https://doi.org/10.1016/j.apenergy.2023.122531.

[37] J. Wang, Y. Yin, Y. Wang, and J. Huang, "Thermal performance analysis of multi-stage cold storage packed bed with modified phase change material based on Na2SO4·10H2O," *Applied Thermal Engineering,* vol. 219, p. 119666, 2023/01/25/ 2023, doi: https://doi.org/10.1016/j.applthermaleng.2022.119666.

[38] P. Hlanze, A. Elhefny, Z. Jiang, J. Cai, and H. Shabgard, "In-duct phase change material-based energy storage to enhance building demand flexibility," *Applied Energy,* vol. 310, p. 118520, 2022/03/15/ 2022, doi: https://doi.org/10.1016/j.apenergy.2022.118520.

[39] J. H. Ahn, H. Kim, J. H. Kim, and J. Y. Kim, "Evaporative cooling performance characteristics in ice thermal energy storage with direct contact discharging for food cold storage," *Applied Energy,* vol. 330, p. 120334, 2023/01/15/ 2023, doi: https://doi.org/10.1016/j.apenergy.2022.120334.

[40] Z. Ouaouja, A. Ousegui, C. Toublanc, O. Rouaud, and M. Havet, "Phase Change Materials for Cold Thermal Energy Storage applications: A critical review of conventional materials and the potential of bio-based alternatives," *Journal of Energy Storage,* vol. 110, p. 115339, 2025/02/28/ 2025, doi: https://doi.org/10.1016/j.est.2025.115339.

[41] W. Liu, J. Cao, T. Hu, D. Jiao, and G. Pei, "Experimental investigation on the characteristics of a controllable separate heat pipe-based cold storage temperature control system," *Applied Thermal Engineering,* vol. 241, p. 122356, 2024/03/15/ 2024, doi: https://doi.org/10.1016/j.applthermaleng.2024.122356.

[42] M. A. Yedmel, R. Hunlede, S. Lacour, G. Alvarez, A. Delahaye, and D. Leducq, "A novel approach combining thermosiphon and phase change materials (PCM) for cold energy storage in cooling systems: A proof of concept," *International Journal of Refrigeration,* vol. 158, pp. 393-404, 2024/02/01/ 2024, doi: https://doi.org/10.1016/j.ijrefrig.2023.12.015.

[43] M. A. Yedmel, A. Delahaye, and D. Leducq, "Analysis of the performance of a refrigerated display cabinet fitted with a thermosiphon thermal accumulator for demand-side management," *Energy Conversion and Management,* vol. 346, p. 120483, 2025/12/15/ 2025, doi: https://doi.org/10.1016/j.enconman.2025.120483.

[44] M. S. K. Tareen, A. F. Zueter, M. Zolfagharroshan, M. Xu, and A. P. Sasmito, "Seasonal ground cold energy storage potential for data center cooling using thermosyphon: A comparative study of five cities in Canada for carbon footprint reduction," *Journal of Energy Storage,* vol. 84, p. 111486, 2024/04/15/ 2024, doi: https://doi.org/10.1016/j.est.2024.111486.

[45] R. Singh, M. Mochizuki, K. Mashiko, and T. Nguyen, "Heat pipe based cold energy storage systems for datacenter energy conservation," *Energy,* vol. 36, no. 5, pp. 2802-2811, 2011/05/01/ 2011, doi: https://doi.org/10.1016/j.energy.2011.02.021.

[46] B. Huang, Z. Zheng, G. Lu, and X. Zhai, "Design and experimental investigation of a PCM based cooling storage unit for emergency cooling in data center," *Energy and Buildings,* vol. 259, p. 111871, 2022/03/15/ 2022, doi: https://doi.org/10.1016/j.enbuild.2022.111871.

[47] Z. Zheng, B. Huang, G. Lu, and X. Zhai, "Design and optimization of an air-based phase change cold storage unit through cascaded construction for emergency cooling in IDC," *Energy,* vol. 241, p. 122897, 2022/02/15/ 2022, doi: https://doi.org/10.1016/j.energy.2021.122897.

[48] X. Ma, Q. Zhang, and S. Zou, "An experimental and numerical study on the thermal performance of a loop thermosyphon integrated with latent thermal energy storage for emergency cooling in a data center," *Energy,* vol. 253, p. 123946, 2022/08/15/ 2022, doi: https://doi.org/10.1016/j.energy.2022.123946.

[49] L. Liu, Q. Zhang, S. Zou, S. Du, and F. Meng, "Experimental study on dynamic thermal characteristics of novel thermosyphon with latent thermal energy storage condenser," *Energy,* vol. 282, p. 128196, 2023/11/01/ 2023, doi: https://doi.org/10.1016/j.energy.2023.128196.

[50] Z. Liu, Z. Quan, Y. Zhao, W. Zhang, M. Yang, and Z. Chang, "Optimization of a cold thermal energy storage system with micro heat pipe arrays by statistical approach: Taguchi method and response surface method," *Renewable Energy,* vol. 238, p. 121899, 2025/01/01/ 2025, doi: https://doi.org/10.1016/j.renene.2024.121899.

[51] Y. Lu *et al.*, "Heat transfer enhancement of latent heat thermal energy storage with longitudinal stepped fins inside heat transfer fluid," *Journal of Energy Storage,* vol. 87, p. 111546, 2024/05/15/ 2024, doi: https://doi.org/10.1016/j.est.2024.111546.

[52] S. Zhang, L. Pu, S. Mancin, Z. Ma, and L. Xu, "Experimental study on heat transfer characteristics of metal foam/paraffin composite PCMs in large cavities: Effects of material types and heating configurations," *Applied Energy,* vol. 325, p. 119790, 2022/11/01/ 2022, doi: https://doi.org/10.1016/j.apenergy.2022.119790.

[53] B. Buonomo, M. Rita Golia, O. Manca, and S. Nardini, "A review on thermal energy storage with phase change materials enhanced by metal foams," *Thermal Science and Engineering Progress,* vol. 53, p. 102732, 2024/08/01/ 2024, doi: https://doi.org/10.1016/j.tsep.2024.102732.

[54] B. Nie, A. Palacios, B. Zou, J. Liu, T. Zhang, and Y. Li, "Review on phase change materials for cold thermal energy storage applications," *Renewable and Sustainable Energy Reviews,* vol. 134, p. 110340, 2020/12/01/ 2020, doi: https://doi.org/10.1016/j.rser.2020.110340.

[55] D. Zhou, S. Xiao, and Y. Liu, "The Effect of Expanded Graphite Content on the Thermal Properties of Fatty Acid Composite Materials for Thermal Energy Storage," *Molecules*, vol. 29, no. 13, doi: 10.3390/molecules29133146.

[56] A. Nandi and N. Biswas, "Experimental and numerical investigation of shape-altered energy storage unit containing nanoparticle-enhanced phase change material (NePCM)," *Applied Thermal Engineering,* vol. 272, p. 126428, 2025/08/01/ 2025, doi: https://doi.org/10.1016/j.applthermaleng.2025.126428.

[57] S. Ahmed *et al.*, "Melting enhancement of PCM in a finned tube latent heat thermal energy storage," *Scientific Reports,* vol. 12, no. 1, p. 11521, 2022/07/07 2022, doi: 10.1038/s41598-022-15797-0.

[58] H. E. Abdellatif *et al.*, "Enhancing latent heat storage: Impact of geometric modifications, S-shaped enclosure walls, and L-shaped fins," *Materials Today Sustainability,* vol. 30, p. 101114, 2025/06/01/ 2025, doi: https://doi.org/10.1016/j.mtsust.2025.101114.

[59] L. Lv, S. Huang, Y. Zou, X. Wang, and H. Zhou, "Heat transfer and thermal resistance analysis under various heat transfer fluid flow rates based on a medium-temperature pilot-scale latent heat storage system," *International Journal of Heat and Mass Transfer,* vol. 220, p. 124896, 2024/03/01/ 2024, doi: https://doi.org/10.1016/j.ijheatmasstransfer.2023.124896.

[60] Z. A. Qureshi, H. M. Ali, and S. Khushnood, "Recent advances on thermal conductivity enhancement of phase change materials for energy storage system: A review," *International Journal of Heat and Mass Transfer,* vol. 127, pp. 838-856, 2018/12/01/ 2018, doi: https://doi.org/10.1016/j.ijheatmasstransfer.2018.08.049.

[61] Y. Lin, Y. Jia, G. Alva, and G. Fang, "Review on thermal conductivity enhancement, thermal properties and applications of phase change materials in thermal energy storage," *Renewable and Sustainable Energy Reviews,* vol. 82, pp. 2730-2742, 2018/02/01/ 2018, doi: https://doi.org/10.1016/j.rser.2017.10.002.

[62] H. M. Ali, "Applications of combined/hybrid use of heat pipe and phase change materials in energy storage and cooling systems: A recent review," *Journal of Energy Storage,* vol. 26, p. 100986, 2019/12/01/ 2019, doi: https://doi.org/10.1016/j.est.2019.100986.

[63] S. Wu, T. Yan, Z. Kuai, and W. Pan, "Thermal conductivity enhancement on phase change materials for thermal energy storage: A review," *Energy Storage Materials,* vol. 25, pp. 251-295, 2020/03/01/ 2020, doi: https://doi.org/10.1016/j.ensm.2019.10.010.

[64] S. A. Mohamed *et al.*, "A review on current status and challenges of inorganic phase change materials for thermal energy storage systems," *Renewable and Sustainable Energy Reviews,* vol. 70, pp. 1072-1089, 2017/04/01/ 2017, doi: https://doi.org/10.1016/j.rser.2016.12.012.

[65] R. Jiang, G. Qian, Z. Li, X. Yu, and Y. Lu, "Progress and challenges of latent thermal energy storage through external field-dependent heat transfer enhancement methods," *Energy,* vol. 304, p. 132101, 2024/09/30/ 2024, doi: https://doi.org/10.1016/j.energy.2024.132101.

[66] A. Khalifa, L. Tan, A. Date, and A. Akbarzadeh, "Performance of suspended finned heat pipes in high-temperature latent heat thermal energy storage," *Applied Thermal Engineering,* vol. 81, pp. 242-252, 2015/04/25/ 2015, doi: https://doi.org/10.1016/j.applthermaleng.2015.02.030.

[67] X.-H. Yang, S.-C. Tan, Z.-Z. He, and J. Liu, "Finned heat pipe assisted low melting point metal PCM heat sink against extremely high power thermal shock," *Energy Conversion and Management,* vol. 160, pp. 467-476, 2018/03/15/ 2018, doi: https://doi.org/10.1016/j.enconman.2018.01.056.

[68] H. Shabgard, T. L. Bergman, N. Sharifi, and A. Faghri, "High temperature latent heat thermal energy storage using heat pipes," *International Journal of Heat and Mass Transfer,* vol. 53, no. 15, pp. 2979-2988, 2010/07/01/ 2010, doi: https://doi.org/10.1016/j.ijheatmasstransfer.2010.03.035.

[69] S. Tiari, S. Qiu, and M. Mahdavi, "Numerical study of finned heat pipe-assisted thermal energy storage system with high temperature phase change material," *Energy Conversion*

and Management, vol. 89, pp. 833-842, 2015/01/01/ 2015, doi: https://doi.org/10.1016/j.enconman.2014.10.053.

[70] X. Liu, G. Fang, and Z. Chen, "Dynamic charging characteristics modeling of heat storage device with heat pipe," *Applied Thermal Engineering,* vol. 31, no. 14, pp. 2902-2908, 2011/10/01/ 2011, doi: https://doi.org/10.1016/j.applthermaleng.2011.05.018.

[71] C. W. Robak, T. L. Bergman, and A. Faghri, "Enhancement of latent heat energy storage using embedded heat pipes," *International Journal of Heat and Mass Transfer,* vol. 54, no. 15-16, pp. 3476-3484, 2011.

[72] C. Ladekar, S. K. Choudhary, and S. S. Khandare, "Experimental investigation for the optimization of heat pipe performance in latent heat thermal storage," *Journal of Mechanical Science and Technology,* vol. 31, no. 6, pp. 2627-2634, 2017/06/01 2017, doi: 10.1007/s12206-017-0505-6.

[73] H. Behi, "Experimental and Numerical Study on Heat Pipe Assisted PCM Storage System," 2015.

[74] Y.-C. Weng, H.-P. Cho, C.-C. Chang, and S.-L. Chen, "Heat pipe with PCM for electronic cooling," *Applied Energy,* vol. 88, no. 5, pp. 1825-1833, 2011/05/01/ 2011, doi: https://doi.org/10.1016/j.apenergy.2010.12.004.

[75] J. Krishna, P. S. Kishore, and A. B. Solomon, "Heat pipe with nano enhanced-PCM for electronic cooling application," *Experimental Thermal and Fluid Science,* vol. 81, pp. 84-92, 2017/02/01/ 2017, doi: https://doi.org/10.1016/j.expthermflusci.2016.10.014.

[76] W. Q. Li, K. Cao, Q. L. Song, P. F. Zhu, and Y. Ba, "Enhancements of heat transfer and thermoelectric performances using finned heat-pipe array," *Applied Thermal Engineering,* vol. 230, p. 120682, 2023/07/25/ 2023, doi: https://doi.org/10.1016/j.applthermaleng.2023.120682.

[77] Y.-Z. Ling, X.-S. Zhang, F. Wang, and X.-H. She, "Performance study of phase change materials coupled with three-dimensional oscillating heat pipes with different structures for electronic cooling," *Renewable Energy,* vol. 154, pp. 636-649, 2020/07/01/ 2020, doi: https://doi.org/10.1016/j.renene.2020.03.008.

[78] N. Sharifi, S. Wang, T. L. Bergman, and A. Faghri, "Heat pipe-assisted melting of a phase change material," *International Journal of Heat and Mass Transfer,* vol. 55, no. 13, pp. 3458-3469, 2012/06/01/ 2012, doi: https://doi.org/10.1016/j.ijheatmasstransfer.2012.03.023.

[79] K. Liu, C. Wu, H. Gan, C. Liu, and J. Zhao, "Latent heat thermal energy storage: Theory and practice in performance enhancement based on heat pipes," *Journal of Energy Storage,* vol. 97, p. 112844, 2024/09/01/ 2024, doi: https://doi.org/10.1016/j.est.2024.112844.

[80] J. Qu, A. Zuo, H. Liu, J. Zhao, and Z. Rao, "Three-dimensional oscillating heat pipes with novel structure for latent heat thermal energy storage application," *Applied Thermal Engineering,* vol. 187, p. 116574, 2021/03/25/ 2021, doi: https://doi.org/10.1016/j.applthermaleng.2021.116574.

[81] J. M. Maldonado, D. Verez, A. de Gracia, and L. F. Cabeza, "Comparative study between heat pipe and shell-and-tube thermal energy storage," *Applied Thermal Engineering,* vol. 192, p. 116974, 2021/06/25/ 2021, doi: https://doi.org/10.1016/j.applthermaleng.2021.116974.

[82] W. Zhong *et al.*, "Heat transfer performance of a device integrating thermosyphon with form-stable phase change materials," *Journal of Energy Storage,* vol. 54, p. 105315, 2022/10/01/ 2022, doi: https://doi.org/10.1016/j.est.2022.105315.

[83] N. Sharifi, A. Faghri, T. L. Bergman, and C. E. Andraka, "Simulation of heat pipe-assisted latent heat thermal energy storage with simultaneous charging and discharging," *International Journal of Heat and Mass Transfer,* vol. 80, pp. 170-179, 2015/01/01/ 2015, doi: https://doi.org/10.1016/j.ijheatmasstransfer.2014.09.013.

[84] N. Sharifi, H. Shabgard, C. Millard, and U. Etufugh, "Hybrid Heat Pipe-PCM-Assisted Thermal Management for Lithium-Ion Batteries," *Batteries*, vol. 11, no. 2, doi: 10.3390/batteries11020064.

[85] A. Faghri, *Heat Pipe Science and Technology*. Global Digital Print (in English), 2016.

[86] https://www.microteklabs.com/product-data-sheets. (accessed.

[87] N. Sharifi, T. L. Bergman, M. J. Allen, and A. Faghri, "Melting and solidification enhancement using a combined heat pipe, foil approach," *International Journal of Heat and Mass Transfer,* vol. 78, pp. 930-941, 2014/11/01/ 2014, doi: https://doi.org/10.1016/j.ijheatmasstransfer.2014.07.054.

[88] S. W. Churchill and H. H. S. Chu, "Correlating equations for laminar and turbulent free convection from a horizontal cylinder," *International Journal of Heat and Mass Transfer,* vol. 18, no. 9, pp. 1049-1053, 1975/09/01/ 1975, doi: https://doi.org/10.1016/0017-9310(75)90222-7.

[89] F. P. Incropera, D. P. DeWitt, T. L. Bergman, and A. S. Lavine, *Fundamentals of heat and mass transfer*. New York John Wiley & Sons, Inc., 1990.

[90] P. D. Weidman and G. Mehrdadtehranfar, "Instability of natural convection in a tall vertical annulus," *The Physics of Fluids,* vol. 28, no. 3, pp. 776-787, 1985, doi: 10.1063/1.865045.

[91] V. Teplyakov and M. Shalygin, "7 - Integrated systems involving membrane vapor permeation and applications," in *Pervaporation, Vapour Permeation and Membrane*

Distillation, A. Basile, A. Figoli, and M. Khayet Eds. Oxford: Woodhead Publishing, 2015, pp. 177-201.

[92] H. M. Sadeghi, M. Babayan, and A. Chamkha, "Investigation of using multi-layer PCMs in the tubular heat exchanger with periodic heat transfer boundary condition," *International Journal of Heat and Mass Transfer,* vol. 147, p. 118970, 2020/02/01/ 2020, doi: https://doi.org/10.1016/j.ijheatmasstransfer.2019.118970.

[93] A. D. Brent, V. R. Voller, and K. J. Reid, "ENTHALPY-POROSITY TECHNIQUE FOR MODELING CONVECTION-DIFFUSION PHASE CHANGE: APPLICATION TO THE MELTING OF A PURE METAL," *Numerical Heat Transfer,* vol. 13, no. 3, pp. 297-318, 1988/04/01 1988, doi: 10.1080/10407788808913615.